GKSS
FORSCHUNGSZENTRUM
in der HELMHOLTZ-GEMEINSCHAFT

Simulation of the Transport of Suspended Particulate Matter in the Río de la Plata

(Vom Department Geowissenschaften der Universität Hamburg als Dissertation angenommene Arbeit)

Author:

H. Hausstein

ISSN 0344-9629

HELMHOLTZ
| GEMEINSCHAFT

wissen
schafft
nutzen

GKSS 2008/7

GKSS 2008/7

Simulation of the Transport of Suspended Particulate Matter in the Río de la Plata

(Vom Department Geowissenschaften der Universität Hamburg als Dissertation angenommene Arbeit)

Author:
H. Hausstein
(Institute of Coastal Research)

GKSS-Forschungszentrum Geesthacht GmbH · Geesthacht · 2008

Die Berichte der GKSS werden kostenlos abgegeben.
The delivery of the GKSS reports is free of charge.

Anforderungen/Requests:

GKSS-Forschungszentrum Geesthacht GmbH
Bibliothek/Library
Postfach 11 60
21494 Geesthacht
Germany
Fax.: +49 4152 87-17 17

Als Manuskript vervielfältigt.

ISSN 0344-9629

GKSS-Forschungszentrum Geesthacht GmbH · Telefon (04152) 87-0
Max-Planck-Straße 1 · 21502 Geesthacht / Postfach 11 60 · 21494 Geesthacht

GKSS 2008/7

Simulation of the Transport of Suspended Particulate Matter in the Río de la Plata

(Vom Department Geowissenschaften der Universität Hamburg als Dissertation angenommene Arbeit)

Hagen Hausstein

109 pages with 48 figures and 11 tables

Abstract

Numerical simulations of the transport of Suspended Particulate Matter in the Río de la Plata estuary were performed with a three dimensional model for coastal waters driven by wave sand currents. Aturbulence based flocculation approach is implemented to the model. The model is for the first time applied under heavy conditions, since the Río de la Plata has discharges up to 25000 m ^{3}/s and SPM concentrations up to 300–400 mg/l. Such concentrations are also difficult to compute from satellite measurements. SeaWiFs satellite images served for the validation of the model results. The model is able to reproduce the shape and the position of the front as well as the zone of the turbidity maximum. It also identifies the zones of erosion and deposition which is of significant importance because of the dense ship traffic along the navigational channels towards Buenos Aires and the cities upstream the rivers.

Simulation von Schwebstofftransport im Río de la Plata

Zusammenfassung

Für den Río de la Plata wurden zahlreiche numerische Simulationen des Schwebstofftransports im Ästuar durchgeführt. Ein drei-dimensionales Schwebstoffmodell, getrieben durch Strömung und Wellen, hat die Verteilung des Schwebstoffs berechnet. Im Laufe der Arbeit wurde ein turbulenzabhängiger Flokkulationsansatz entwickelt, der die Ergebnisse deutlich verbessert. Das erste Mal wurde das Modell unter schwierigen Bedingungen mit Abflussgrößen bis zu 25.000 m^3/s und Schwebstoffkonzentrationen bis 300–400 mg/l eingesetzt. Unter solchen Bedingungen ist auch die Errechnung der Schwebstoffkonzentrationen aus Satellitenmessungen sehr kompliziert. Satellitenbilder von SeaWiFs wurden für die Auswertung der Simulationsergebnisse herangezogen. Es konnte gezeigt werden, dass das Modell die Schwebstofffahne in der Form und der Position gut wiedergibt. Auch die Trübungszone wurde durch das Modell gut berechnet. Ausserdem wurden Erosions- und Sedimentationsgebiete lokalisiert, was gerade für den dichten Seeverkehr Richtung Buenos Aires und stromaufwärts von großer Bedeutung ist.

Manuscript received / Manuskripteingang in TKP: 11. Juni 2008

Contents

List of Figures

List of Tables

Chapter 1

Introduction

SPM is a synonym in earth sciences for Suspended Particulate Matter. The complex definition of Wilber (1983) gives the reader a clear idea of what SPM is and what the knowledge of SPM can be used for. He states that SPM is "...sediment carried in suspension by the turbulent components of the fluid or Brownian movement". It is the residue in a well-mixed sample of water that will not pass through a standard, glass fiber (0.45 μm) filter. Suspended sediments can also be called suspended solids or suspended particles. A water body's suspended load is a component of the total turbidity. Generally, the suspended loads in flowing water consists of grains less than 0.5 mm in diameter. There are various types of suspended sediment. Eroded soils produce the most important type of suspended solids on a large scale. Samples of eroded soils include sand, silt, and clay that are relocated by rainfall and overland flow and carried into rivers and lakes from rural and agricultural areas, forests, and urban areas. Organic suspended particulates compose a significant part of suspended solids in most natural waters. The organic fraction is often higher in nutrients than the inorganic fraction of the soil. Suspended solids can carry nutrients and pesticides throughout the water system. In addition, suspended solids near the waters surface absorb additional heat from sunlight, raising surface water temperatures (Wilber, 1983).

This doctoral thesis outlines an approach to simulate the transport of SPM in the Río de la Plata (RdP) estuary in Argentina/Uruguay. The reason for numerical simulations of suspended sediments is that a spatial distribution of SPM is essential for describing biological processes in coastal waters, deriving

information on erosion or depositional systems for ship traffic, identifying possible sites for waste dump, estimating water qualities for tourism purposes or trace the dispersion of contaminants which stick on SPM particles. The simulation and the acquisition of SPM data is meaningful for the Río de la Plata (RdP) if one regards the extensive use of this highly populated estuary. The coastal environment is permanently stressed by physical influences like wind, waves and tides but also by human intervention. Human pressure is given by two major cities accessing the tidal river: the capitals of Argentina and Uruguay, Buenos Aires with about 12 million inhabitants and Montevideo with about 1.5 million inhabitants. Both cities have huge ports, thus heavy ship traffic occurs along the coasts. Since Buenos Aires does not have a natural habour, annual dredging is required. This demands an intensive investigation in order to steer and maintain the equilibrium between nature and humans. It is one of the largest and most important estuaries and serves several South American countries having access to the estuary or the catchment area of the river system directly and indirectly. This work is a first attempt to estimate in the RdP the spatial distribution of SPM in three dimensions and also in time. Wind, currents and waves are the main driving forces in this investigation.

The investigation of the RdP started in the middle of the last century. First investigations were done on the geology and the morphology of the RdP itself and the sediment loads of the RdPs contributing rivers (Depetris, 1968; Depetris & Griffin, 1968; Laborde, 1987; Urien, 1967). Depetris (1968) mentioned a total suspended load at the mouth of the RdP of about 65 $tons/km^2$. He also investigated the composition of the SPM split in clay minerals and silt minerals in the RdP and the tributaries. Annual campaigns along the navigational channels on the RdP are operated by the Port Authorities and result in information along a ship track, but do not give information on the spatial distribution. The experience in numerical simulation of the transport of SPM in the RdP is recent and based on two-dimensional computations. Jacovkis (2002) and Menendez (2001) report approaches to estimate sediment dynamics in the estuary. Tracer simulations with hydrodynamic models have been applied to state a current-based distribution of substances (Simionato *et al.*, 2003). Parker *et al.* (1987) presented a conceptual model for sediment transport with focus on the morphogenesis of the bottom of the RdP. However, these approaches do not include any sediment dynamics like

sinking of particles, effect of waves and flocculation. In other words, there is still no approach that presents a roughly true spatial, three-dimensional distribution of SPM in the RdP including the wave dynamics as an important force keeping the material in suspension even after storms. The transport of SPM as well as the spatial and temporal distribution of sediments is presented with this research project, which is an extension of the completed project between the University of Hamburg (Germany) and the University of Buenos Aires (Argentina). This project included the simulation of the currents along the Patagonian Shelf. The GKSS Research Center has developed models for treating the task of the present research.

The RdP is an interesting environment for testing and applying the abundant models under heavy conditions with high sediment concentrations. Also the shallowness is a crucial point, because the wave conditions are more complicated than in deep water environments. It is a very complex system influenced both by dynamic interactions between its fresh and salt water components, and by the geological history of the region. The drainage basin occupies parts of five countries, and is exceeded in South America in size only by that of the Amazon. Natural and anthropogenic changes influence many estuarine characteristics of the Río de la Plata, and consequently have influence on several million people who live within its boundaries (Laborde, 1997). The RdP is situated between 36.5° S and 34.0° S and 59.0° W. It is nearly 250 km long and covers an area of approximately 38,800 km^2. The RdP separates two well defined physiographic units: in the north the Uruguayan-Brazilian Shield, which is predominantly granitic, and in the south the Argentine sedimentary basin, namely the "Pampas", which has a depth of more than 2,000 m of fine sediments. This leads to contrasting coastal characteristics: sandy beaches with bars, ridges and dunes as well as single cliff areas in the north, and a low and flat marsh land with lagoons, schorres, ancient beach ridges and active dune fields in the south (Laborde, 1997). The drainage basin of about 3,170,000 km^2 includes the mayor contributors: the Uruguay river and the Paraná river. Together these contributors discharge in average 22,000 m^3/s to the RdP. The Paraná river is supposed to be the largest contributor of SPM with approximately 75% and the Uruguay river is with approximately 25% the second largest (Depetris & Griffin, 1968). Considering the area and the geological formations which each of the rivers runs through, the amount of sediment

load is correspondingly high. Figure 1.1 gives an impression of the sediment load passing the RdP. It shows the plume of the RdP. The brownish areas are zones of high SPM concentrations. The front of the plume is clearly visible. There is a transition to waters with evidently much lower SPM concentration.

The thesis is organized as follows: The Chapter 2 explains the area of interest and points out the sedimentological and morphological units of the RdP which lead to current patterns and SPM distributions. Chapter 3 gives a brief overview on the methodology where the model system and its application in the present research is explained. An insight on the data situation is given in Chapter 4, and Chapter 5 describes each of the models and its physics. In Chapter 6 a description of the setup of the models is given and Chapter 7 presents the results of the simulations. The conclusion of this work and the outlook are presented in Chapter 8.

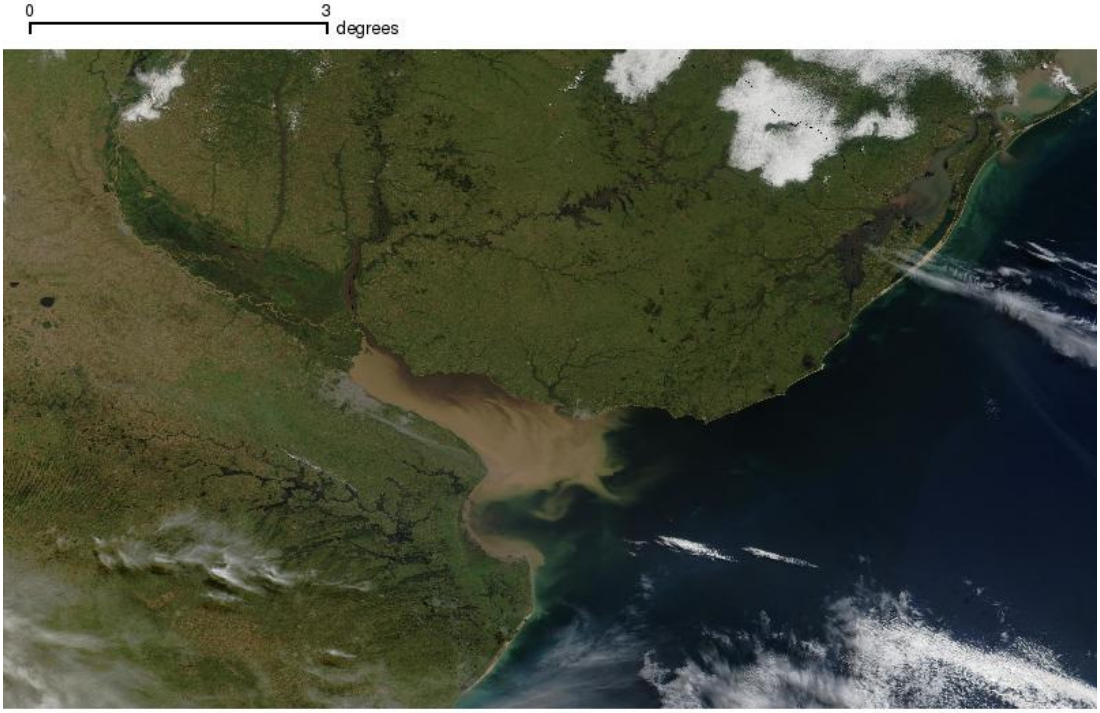

Figure 1.1: Satellite image of the Río de la Plata, 2002-05-09, Terra/MODIS.

Chapter 2

Description of the morphology and hydro-climatic setting

2.1 Morphology

The sedimentological and geological characteristics of the Río de la Plata were extensively studied by Carvallotto (1987) and Parker & Laborde (1990). The authors identified morphological units which were adopted in the present work and are represented in Figure 2.1.

2.1.1 Morphological units

- Playa Honda. This area is the subaqueous extension of the Paraná river delta limited by the 6 m isobath, occuring as a wide spread shallow area crossed by channels. The bottom sediments have their origin from the fluvial load which deposites as the flow velocity decreases. Those sediments form bars across the outlets so that the discharge is forced to find new outlets. The prograding plain develops as the bars become joined and islands are formed. This differential lineal growth is understood as the relation of the southern discharge of the Uruguay river which causes a redistribution of the sediments transported by the Paraná river delta tributaries.

- Sistema Fluvial Norte. This system includes all the channels that extend from the RdP watersheds to Colonia. It is characterized by a number of trenches of about 6 m depth due to the erosive action of the Uruguay

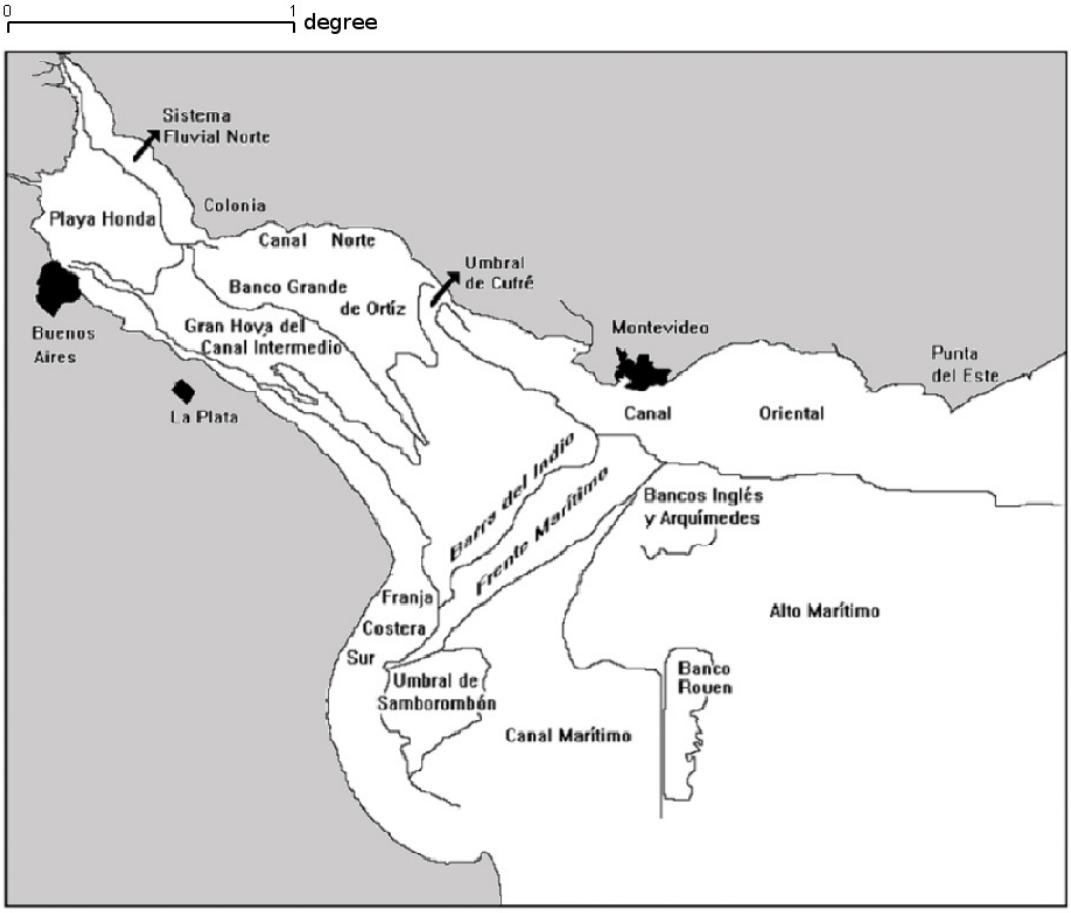

Figure 2.1: Morphology of the Río de la Plata according to Carvallotto (1987) and Parker & Laborde (1990).

river. Its morphology is unstable as consequence of the dynamic balance between the subaqueous delta advance to the north and the discharge of the Urugugay river. Discontinuous and short-term morphological changes are shown by movements along the channel axis and sedimentation processes allowing the fluvial forms and islands to grow.

- Banco Grande de Ortíz. This is a large area of the RdP between Canal Norte, near the Uruguayan coast, and Gran Hoya del Canal Intermedio. It appears as a broad plateau east of Colonia and has a steep southern slope (limited by the 6 m isobath) and is flattened to the north and south east. The shape corresponds to the local current patterns determined by

the discharge action of the river.

- Gran Hoya del Canal Intermedio. This is a wide spread depression to the south of Banco Grande de Ortíz. It has a longitudinal extension and its design corresponds to flood and ebb conditions, that is why it is a good example of the morphogenetic capacity of tidal currents.

- Canal Norte. This extends between the Uruguayan coast and Banco Grande de Ortíz, with a depth around 5.0 m. It forms a gentle depression related to the Sistema Fluvial Norte channels and it is the obligatory passage for discharge currents along the coast.

- Canal Oriental. This long and extended depression of about 15 to 20 m water depth near the Uruguayan coast is directed EW and follows the coastline to the NE near Punta del Este, where it deepens abruptly to 40 m. This NE area of the Canal Oriental is also called Pozos de Fango (mud wells).

- Barra del Indio - This is a wide and gentle plain across the RdP between Montevideo and Punta Piedras. It has an almost horizontal surface formed from recent clay aggradations overlapping Holocene sands (Urien, 1967). Water depth here ranges from 6.5 to 7.0 m.

- Franja Costera Sur - This unit is found along the Argentine coast from Buenos Aires to Cabo San Antonio. It is a inclined plane extending from the coast up to the 6.0-9.0 m isobaths. It appears as a favoured area for sediment deposition because it is located windward of the dominant winds and it experiences low wave energy, and because of its relationships with the major river channels.

- Alto Marítimo. This is the outer Río de la Plata region with about 25 to 30 m water depth containing the Inglés, Arquimedes and Rouen banks. The first two represent stable areas which act as water dividing systems.

- Umbral de Samborombón. This is a triangular region resulting from a change in surface slope, situated between the center of Bahía de Samborombón and the Canal Marítimo. The area has water depth from 8 to 12 m.

- Canal Marítimo. This is an extensive, gently sloping depression of 15 to 25 m, with an asymmetrical profile, developed between Barra del Indio, Franja Costera Sur, Umbral de Samborombón and Alto Marítimo.

2.1.2 Surficial sediments

The surficial sediment distribution according to Laborde (1987) has been taken as basis for the present investigation and is represented in Figure 2.2. It is the most detailed and latest distribution available for this region. The description of Figure 2.2 takes into account the morphological units given in Figure 2.1.

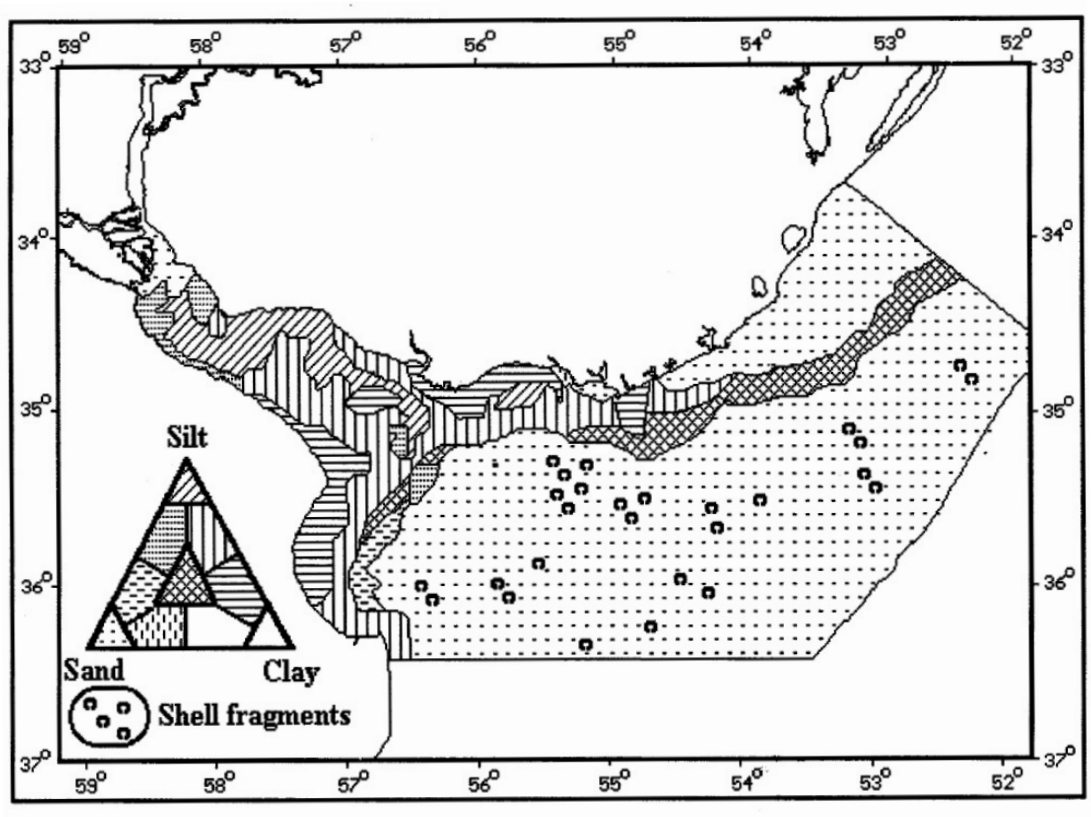

Figure 2.2: Surficial sediment distribution of the Río de la Plata according to Laborde (1987).

Surficial bottom sediments show a graded distribution from coarse sediments (sand) to fine sediments (clay) (Urien, 1967). Sand predominates where the rivers discharge to the RdP, silts are dominant in the middle region and clayey silt occur

towards the mouth of the RdP. In the upper and middle river two particular observations can be made. Along the Uruguayan coast occur mainly sands and silty sand near Playa Honda, grading to silty sands and silts in Banco Grande de Ortíz, while in the outer river clayey silts are found and even silty clays are abundant. On the other hand, along the Argentine coast finer textures with high organic carbon content are observed even near Buenos Aires. Sediments spread over the coast, forming a homogenic matter of sandy silts and silts grading to silty clays.

These two main transport pathways remain separated by Playa Honda, Gran Hoya del Canal Intermedio to Barra del Indio where plains of clay content higher than 25% and mean grain diameter lower than 25 microns. These deposits correspond to the salt intrusion limit and the location of the turbidity maximum. The outer limit is located where recent sands overlap the Holocene sands (Parker *et al.*, 1985).

The banks e.g. Playa Honda and Barra del Indio act direct to the river discharge, and at the same time accumulate sediments and scatter fine sediments due to wave action. Erosive basins e.g. Gran Hoya del Canal Intermedio alternatively act either as temporary sources or sinks of sediment in response to tidal action. Channels act directly to the river discharge.

2.2 Hydro-climatic setting

Nagy *et al.* (1997) separated the RdP in 6 zones which are based on analysis on salinity, turbidity and morpholgical variation. The result is illustrated in Figure 2.3: The upper (freshwater tidal river) region is formed by:

- the Paraná delta zone, developed by a great amount of sand and fine sediments supplied by the Paraná river. Immediately seaward, the presence of sand banks is related to this fluvial sand supply;
- the tidal river zone;
- the middle RdP (intermediate or estuarine region) is placed between the salt intrusion limit and a prograding fluvio-tidal delta (Barra del Indio), where

the cross-section increases. The extent of this region is strongly dependent on river flow and wind variation.

The 6 to 8 m isobaths penetrate along the northern middle and upper coast region, largely explaining the mean position of the salt intrusion and the vertical structure of the system. The outer region is formed by three zones:

- Canal Oriental;
- Bahía de Samborombón;
- Alto Marítimo (central outer).

All three areas have characteristic hydrodynamics and sedimentary processes. The first is a natural (undredged) ancient river valley, the second is a shallow, slightly stratified bay (< 10 m), and the latter (central outer) is located over the marine sands arch. This one is a semi- enclosed shallow shelf stratified sea where the sandy bottom and the outer banks are relict (Holocenic), and not influenced by the daily hydrodynamics of the system.

Nagy *et al.* (1997) states that due to the shape, extent and microtidal regime of the middle RdP the atmospheric processes, especially the wind regime, play a major role in the dynamics of water and mobile sediment in the river system. Circulation and stratification patterns, sea level height, wave climate, sediments and particle behaviour are, to a great extent, controlled by the fetch, the steadiness and the amount of the wind even under non-stormy conditions. In the RdP winds from north and northeast prevail through the year but in winter, the northward displacement of the subtropical high pressure belt provokes an increase in frequency of west winds while in summer, wind comes from east to southeast. In the investigation of Nagy *et al.* (1997) they point out that the wind situation mainly affects both the coastal salinity and the overall system salinity. Summer axial ESE-E predominant winds favour the upper layer saline water entrance, in addition to the decreased influence of the river flow. In spring and summer, SE and E stormy events favour the saline entrance. In winter, the pattern is more complicated. NNW, E, N and NE directions predominate, but the intensity of winds from the SSW is very important therefore, the residual stress is very weak. NNW winds favour the fresh/brackish water evacuation. The river flow and the discharge very much depends on the seasonal cycle. During winter season the

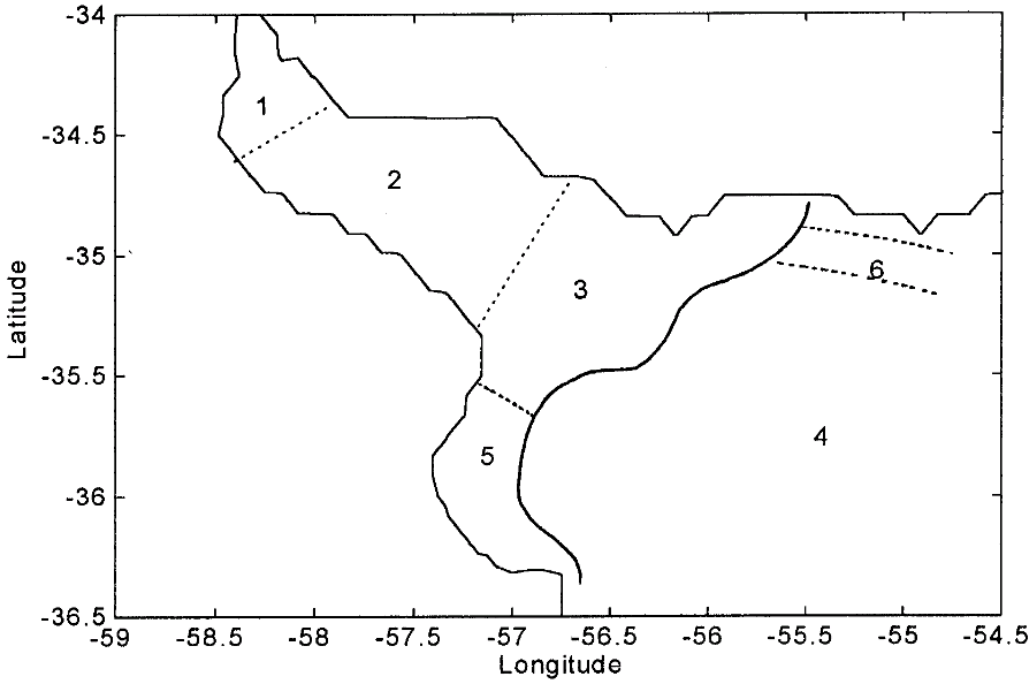

Figure 2.3: Schematics of the morpho-hydrological zonation of the Río de la Plata system (Nagy *et al.*, 1997)). 1= Paraná River Delta watersheads. 2= Tidal River. 3= Estuarine transition. 4= Outer or Marine region (relict sands). 5= Samborombón Bay. 6= Outer Canal Oriental.

continental rainfall is high and the rivers Paraná and Uruguay can discharge up to 25000 m^3/s. Discharge minima occur during summer season with values of about 18000 m^3/s. Extreme monthly mean salinities occur in January (maximum up to 35 psu (part per thousand, salinity unit)), and in May-June and August (minimum down to 2 psu). However, absolute minimum salinities may occur all through the year, especially in February, May, June, August, October and December, but not in January and seldom in July. Some seasons or months are especially affected by river floods eg. early autumn (Paraná river), late autumn and August (combined flows) and October (Uruguay river). The water temperatures vary according to the salinities. The maximum is observed in summer with temperatures up to 25 $°C$. Temperature minima of about 12 $°C$ occur during the winter season from June to August..

The tidal regime has been very intensively studied over the last decades. The tidal regime is semidiurnal with diurnal inequalities. The lunar M_2 component is

the most energetic, but other components like S_2, N_2, K_1 and 0_1 have effects on the tidal regime. The ocean tidal wave is modified in the river by winds, Coriolis force, depth and cross-section decrease. In his tidal analysis O'Connor (1991) found that tidal amplitudes are higher in the southern coast (with a maximum of about 1 m), than in the northern coast, where the maximum amplitude is only about 40 cm. Wind stress can modify this tidal behaviour, creating a continuously increasing or decreasing trend of 2 or 3 m during 2-3 days (Nagy *et al.*, 1997). The sea level is less influenced by tides than by wind forcing and/or wind waves and swell. Extreme values greater than 3.5 m have been measured during the passage of storm surges on the coast. Wave heights greater than 2.2 m are reached every year (Nagy *et al.*, 1997).

Chapter 3

Methodology

3.1 Model system

The flowchart in Figure 3.1 illustrates the methodology used in this work. It represents the data flow in the model system. The boundary and driving input data are represented in blue color. The resulting SPM data set is colored yellow and the arrows indicate which data go into a computation. Pleskachevsky *et al.* (2003) developed a 3D SPM at the GKSS Research Center. This model is driven by currents and waves and interacts permanently with the bathymetry. The bathymetry is an essential parameter for any of the steps in the methodology. Current and wave data could not be acquired as spatial data sets. Therefore, there was a need to setup adequate models to compute such data.

Simionato *et al.* (2001) have set up the HamburgShelfOceanModel (HamSOM) (Backhaus, 1983) to simulate successfully hydro-dynamics in the RdP. For this reason the HamSOM has been chosen as an appropriate tool to compute reliable hydro-dynamic input for the SPM model. The HamSOM requires the available bathymetry and is driven by wind, discharge and tides. The computation of waves also requires the bathymetry data mentioned before. For the present work two different wave models were applied. The WAM (Günther *et al.*, 1992) which is adequate in deep water and the K-Model (Schneggenburger, 1998) which is appropriate for shallow water wave computations. Any of the mentioned wave models require currents, waterlevel variations and winds as well as the bathymetry. Therefore, currents need to be simulated first, followed by waves. As consequence, the order of computing the demanded SPM drivers, currents and

waves, is fixed. With currents, waves as well as with the bathymetry and SPM data on the bottom and on the river outlet, the SPM model can be set up to compute spatial SPM concentrations in three dimensions and in time. Each of the mentioned models run independently. At the time when the present work started there was no interactive coupling of the models implemented.

3.2 Grids and nesting

The current and wave models were performed in nested mode. A nesting was necessary in both models in order to aproach a true state in small scales inside the RdP. Grids were generated based on the available bathymetries which will be explained in Chapter 4. Figure 3.2 shows nested grids. Grid F is the finest grid and covers the area of interest. A nesting has been applied previously by Simionato *et al.* (2001) for hydro-dynamic simulations. This approach was adopted for the hydro-dynamic simulations using the grids C_{cur}, M and F. The nesting method for the simulation of waves was changed slightly because long swells were expected from any direction in the South Atlantic Ocean. Instead of the coarse grid C_{cur} a new coarse grid C_{wav} was introduced. The coarse grid C_{wav} covers the region near Antarctica as well as South Africa and up to the Equator. Table 3.1 explains the grid dimensions and resolutions.

Table 3.1: Grid dimensions and resolutions.

	Lat	Lon	Resolution
C_wav	$-10.0°$ to $-72.0°$	$-69.5°$ to $25.0°$	30 NM
C_cur	$-23.5°$ to $-56.5°$	$-69.5°$ to $-45.5°$	20 NM zonal, 15 NM meridional
M	$-31.5°$ to $-42.0°$	$-61.5°$ to $-51.5°$	6 NM
F	$-34.0°$ to $-36.5°$	$-59.0°$ to $-54.5°$	1.5 NM

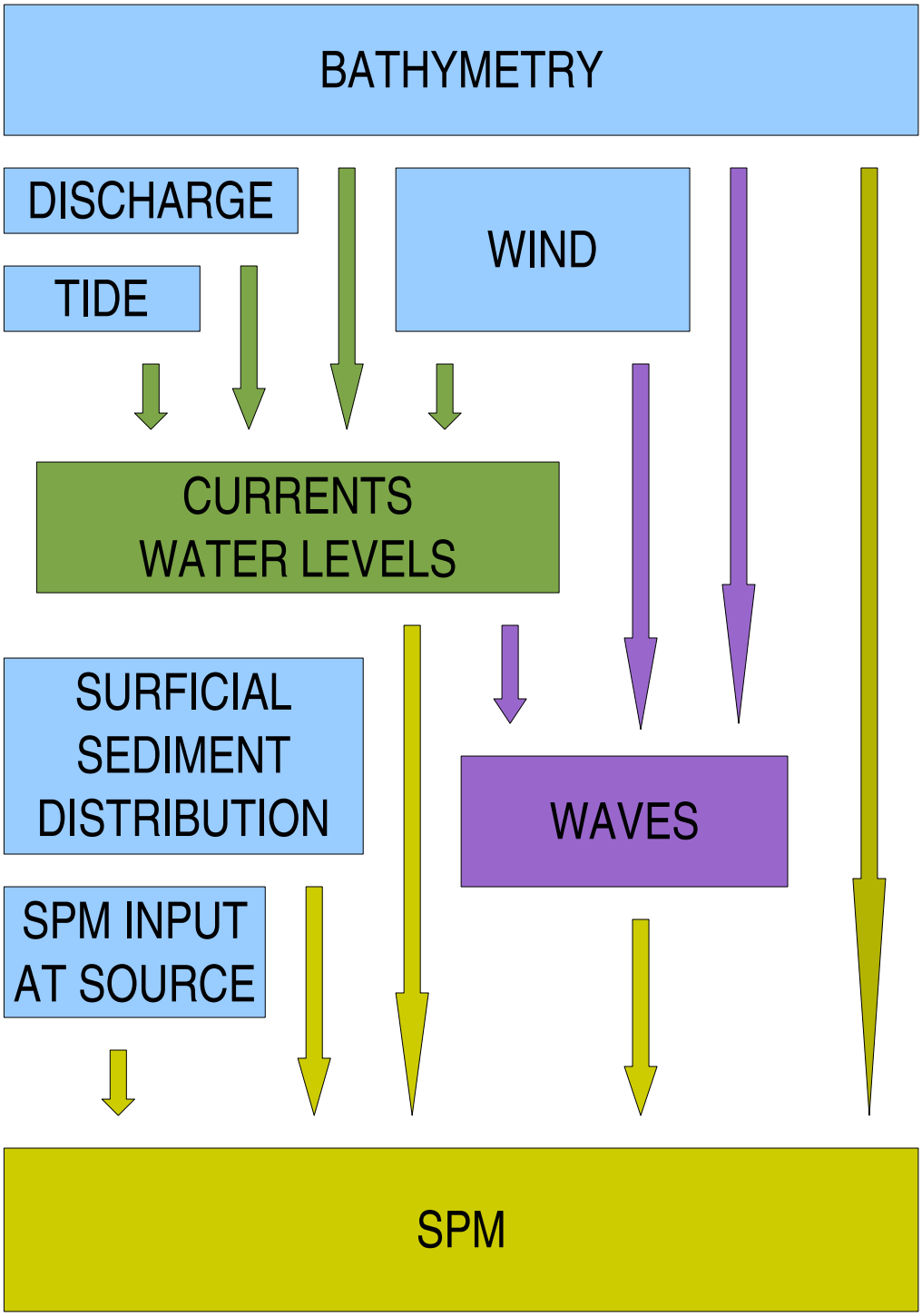

Figure 3.1: Model structure.

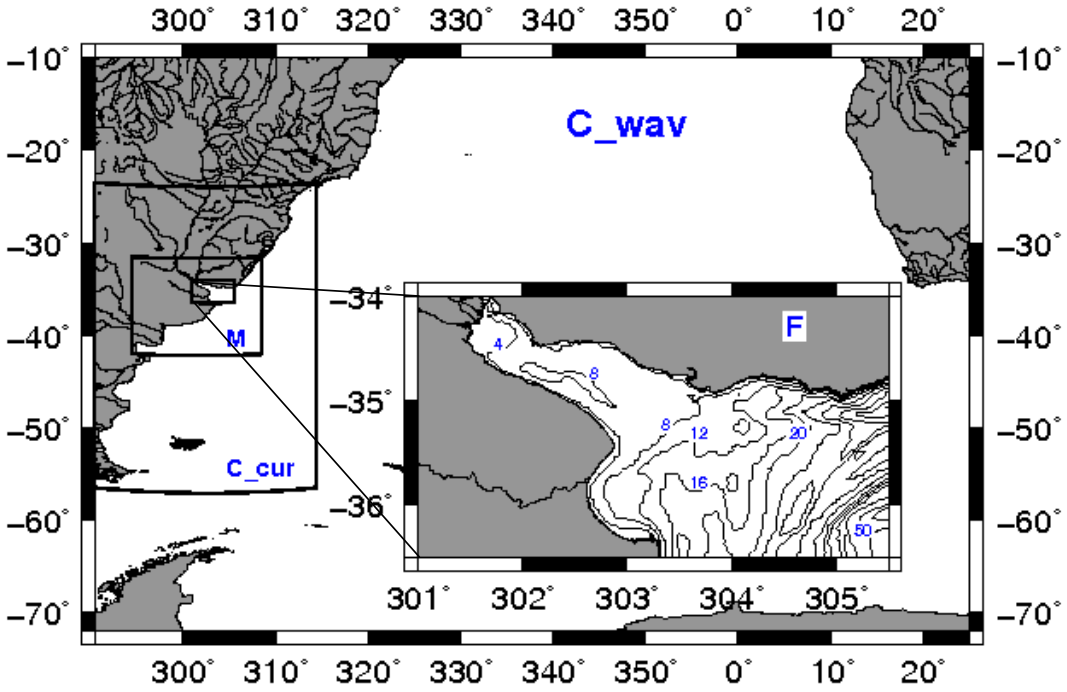

Figure 3.2: Grid setup - inserted fine grid bathymetry (depth in meters).

Chapter 4

Description of utilized data

Following the flow-chart in Figure 3.1 of Chapter 3 a number of data such as model drivers and boundary data (in blue color) were acquired. Besides those, hydro-dynamic, wave and SPM data were also obtained in order to validate the computed model results. The present chapter explains the data and the chosen time frame for the data acquisition.

4.1 Simulation times and data availability

The acquisition of data was a mayor trigger for selecting the time frame of the simulations. The year 1999 was the only year in which data was available for driving and validating the models. Data of currents, waterlevels and discharges were available only for the period of February 1999. Wave data were available for the second half of 1999. Also for the second half of 1999 satellite images were acquired to retrieve SPM data. Between October 20th and November 10th 1999 a storm event occured. The present research will mainly focus on this time interval because the meteorological situation induced interesting conditions for SPM transport. Winds from the east induced a current inside the RdP and intensified tidal currents. Due to strong wave action and long swell the SPM was kept in the water column even after the storm abated.

4.2 Bathymetry

The bathymetries origin from the ETOPO5 (Mansbridge, 2005) data set, but have been improved for depths lower than 200 m with data provided by the Servicio de Hidrografia Naval de Argentina (SHN, 1986). They have been updated and refined using nautical charts (SHN, 1992, 1993, 1999a, 199b). The corresponding bathymetries are presented in Figures 4.1, 4.2 and 4.3. The bathymetry of the grid C_{cur} is not placed here because it is already covered by the grid C_{wav}. In Chapter 3, the grids on which the bathymetries are based were introduced. On grid C_{wav}, the depth ranges from 0 to 6000 m. Even the area of grid M has a depth up to 5500 m. The area of interest (grid F) has depth values from 0 to 55 m. The scale bars indicate the depth in each of the Figures. Bathymetries on grid C and grid M show clearly the shelf edge, where the depth increases rapidly from 200 to several 1000 m. Such sharp gradients are not recognizable in the bathymetry on grid F.

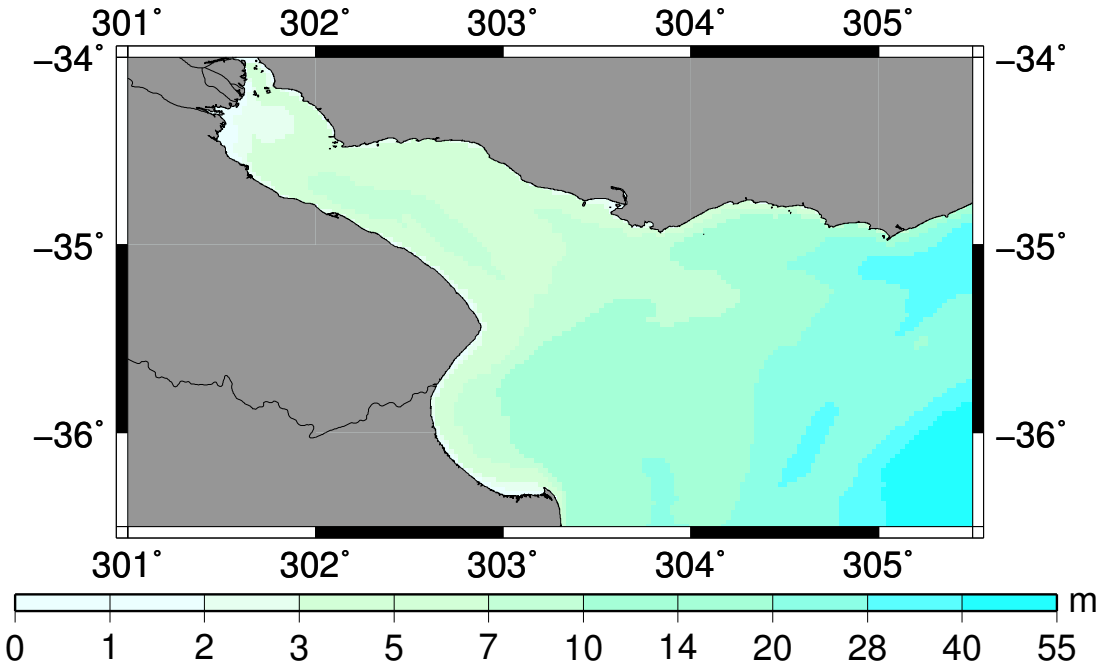

Figure 4.1: Bathymetry of the Río de la Plata - based on the fine grid F.

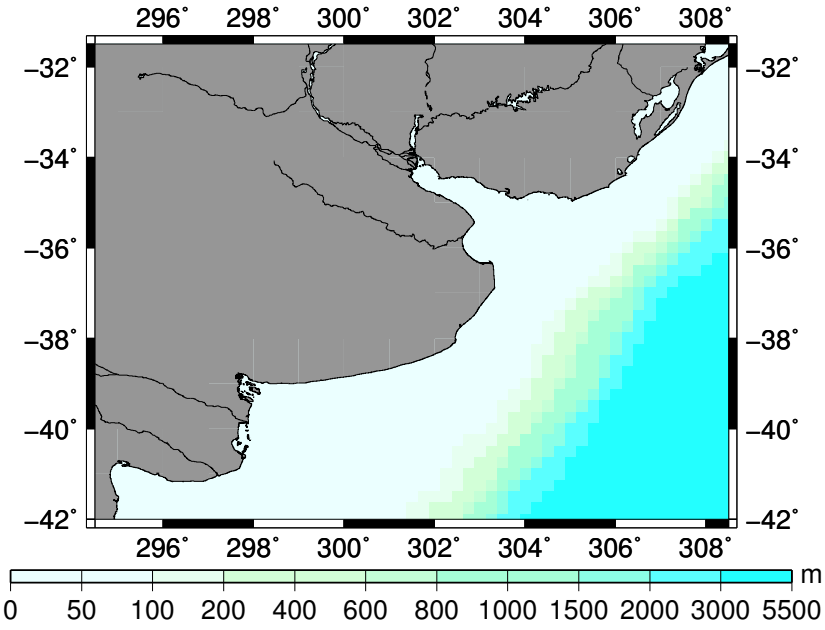

Figure 4.2: Bathymetry of area near the Río de la Plata - based on grid M.

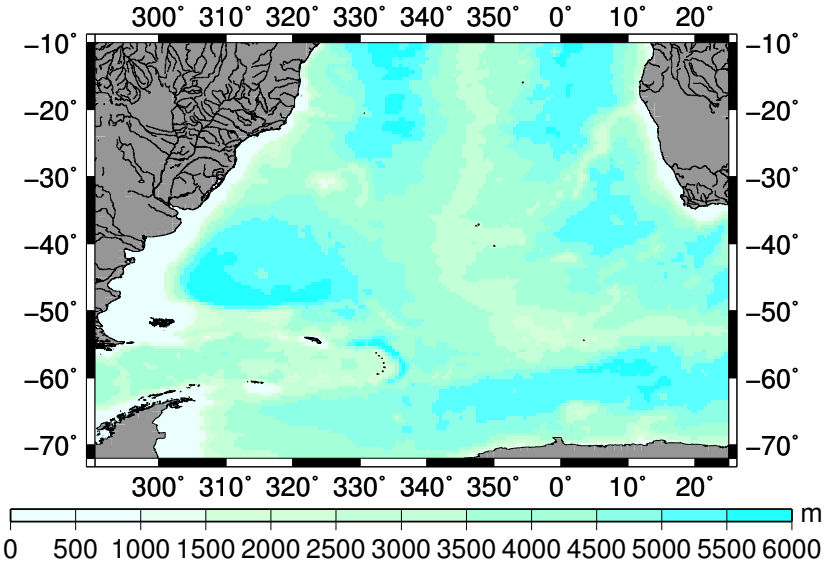

Figure 4.3: Bathymetry of the South Atlantic Ocean - based on grid C_{wav}.

4.3 Wind

Wind data have been acquired from the web-server of NCEP reanalysis NOAA-CIRES (Tolman, 1998). It provides 6 hourly U_{10} wind fields (wind speed at 10 m height) separated in zonal and meridional compontents. Figure 4.4 describes the wind situation during the year 1999. The mean wind speed is between 5 and 10 m/s. A few events come with winds up to 15 m/s and more. These events are dispersed over the year and are not concentrated in any season. During winter time there are long periods with winds from the west, while during summer time winds prevail from an easterly direction. This is typical for this region (Simionato *et al.*, 2001) (Nagy *et al.*, 1997).

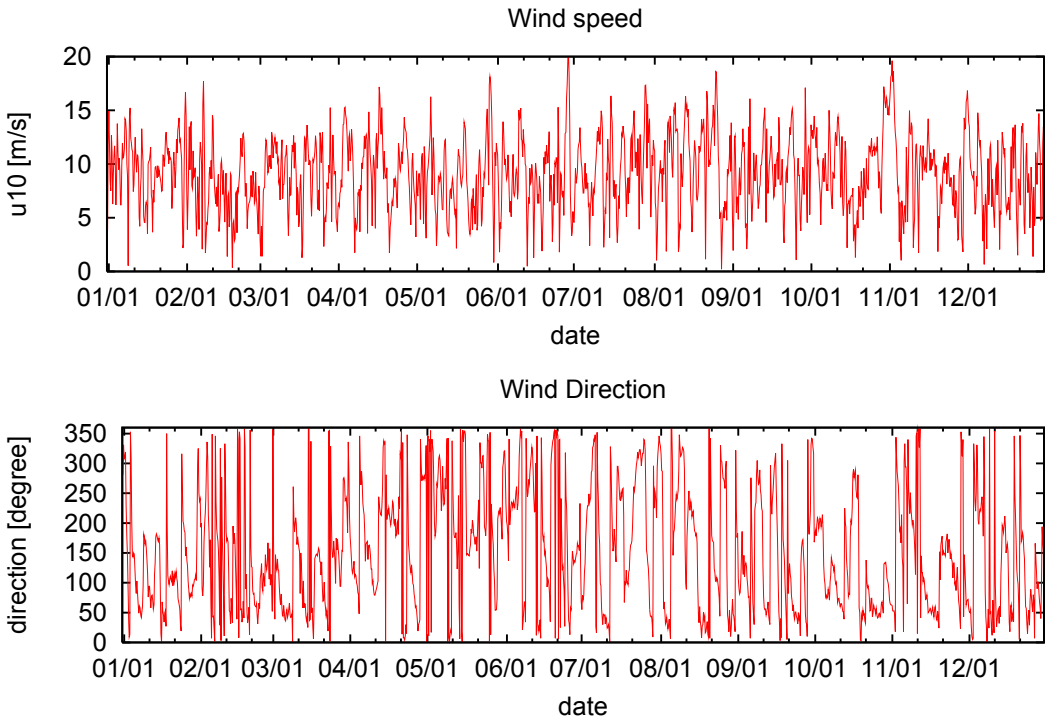

Figure 4.4: Wind conditions in Río de la Plata entrance for the entire year 1999 - directions follow the meteorological convention.

Figure 4.5 focuses on a typical wind condition during spring/summer with mainly constant easterly winds in moderate speed scales (Simionato *et al.*, 2001). Surface winds between October 20th and November 1st remained constant from

E - NE. From October 29th until November 2nd a storm event occured. Wind speed increased up to 20 m/s and abated later to low and moderate winds.

Figure 4.6 demonstrates the wind situation on October 30th of 1999 on the South Atlantic Ocean. A cyclone south of the RdP induces strong winds which point to the area of interest. Such an event creates a long swell entering the RdP and can lead to a waterlevel increase in the RdP.

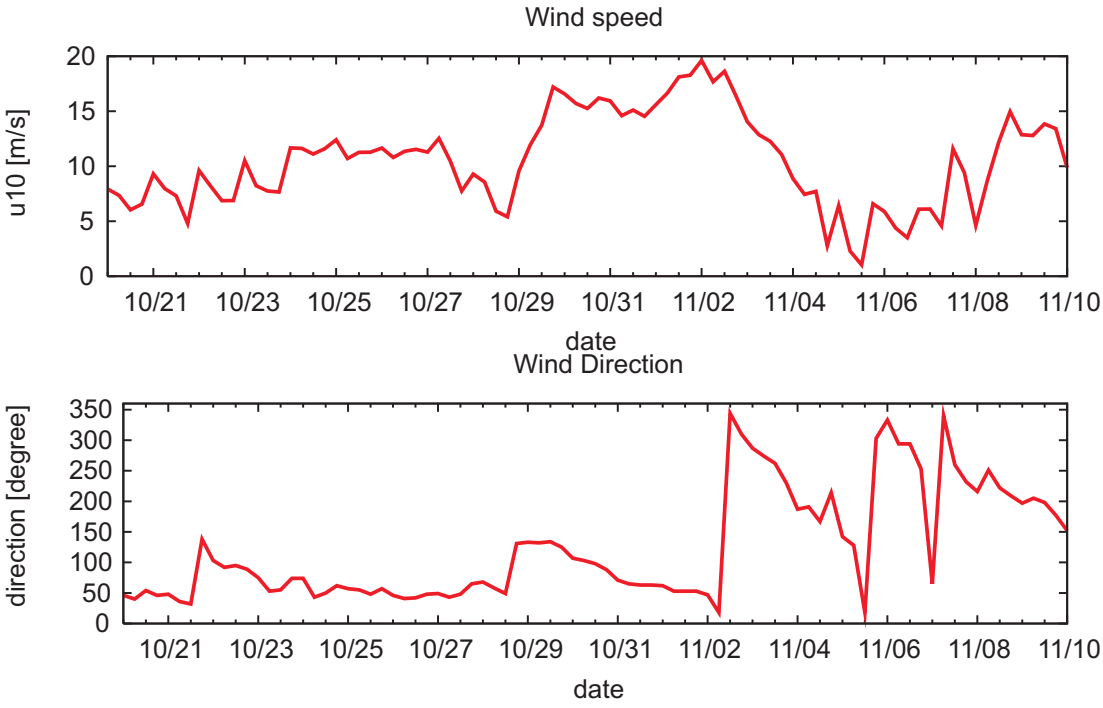

Figure 4.5: Wind conditions in Río de la Plata entrance from October 20th to November 10th of 1999 - directions follow the meteorological convention.

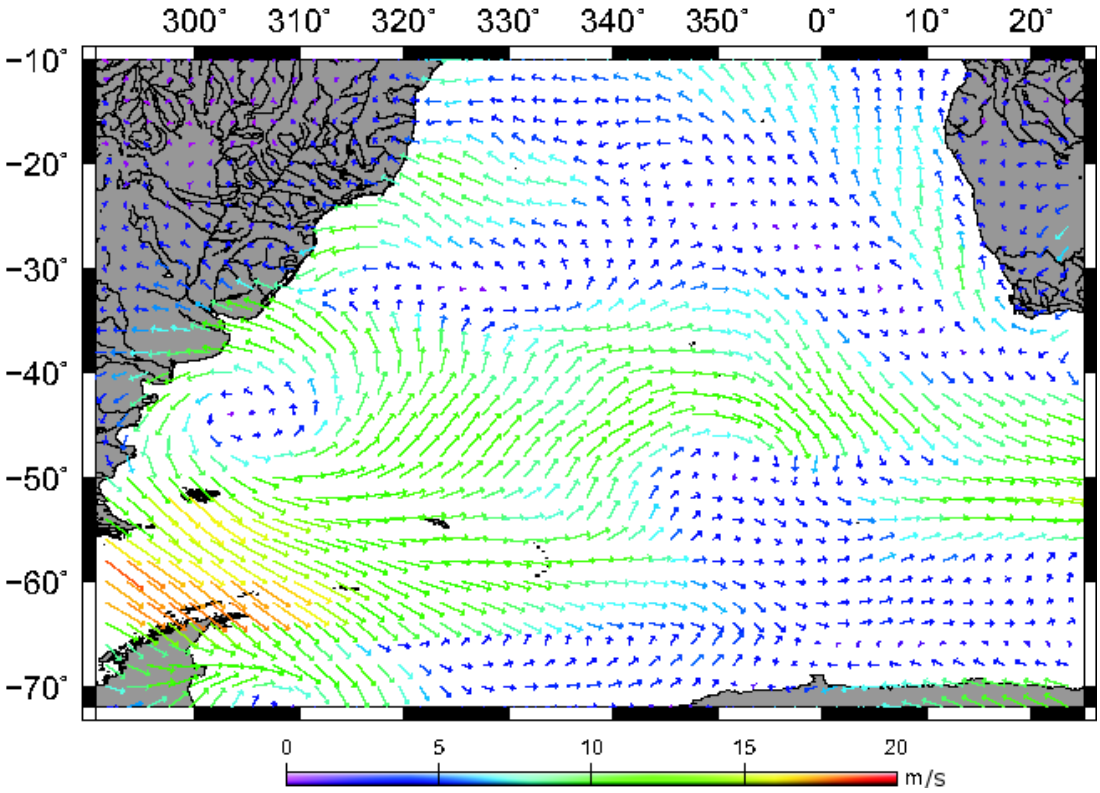

Figure 4.6: Wind situation on October 30th, 1999 with prevailing wind heading to the RdP.

4.4 Discharge data

The discharge data have been received through cooperation with the University of Buenos Aires. They are based on daily measurements and include the discharges of the two major rivers: the Uruguay river and the Paraná river. The received data set contains the entire discharge of the region bundled to a single outlet point where the river Uruguay and large parts of the river Paraná meet. The portion of each of the rivers cannot be distinguished. Figure 4.7 shows the variation of the discharge to the RdP over the year. The freshwater discharge during the winter season is higher than in summer time. In the humid winter period the discharge exceeds 25000 m^3/s while in summer only 15000 m^3/s run off. The figure shows that 1999 was a relatively dry year compared to the decade 1985 - 1994 (Nagy *et al.*, 1997). The monthly mean discharge for the decade of 1985 - 1994 is higher in summer and winter season.

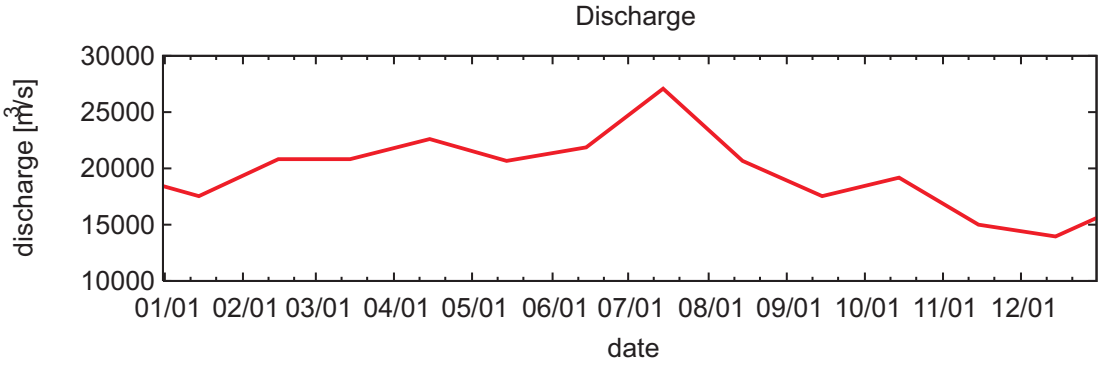

Figure 4.7: Sum of the discharge of the Paraná river and the Uruguay river in the year 1999.

4.5 Tidal constituents

The tidal constituents M_2 and S_2 are boundary parameters for hydro-dynamic simulations with the HamSOM. The M_2 is the tidal constituent which has largest impact on the tidal variability in the RdP. At the RdP entrance it amounts to about 65 cm of amplitude in the south and only a few centimeters in the north. The impact of the S_2 component is only 1/6 of the impact of the M_2. All tidal

constiutents are listed in Table 4.1. The tidal boundary information is adopted from the simulations performed and explained by Simionato *et al.* (2001).

Table 4.1: Major and minor tidal constituents in the Rio de la Plata.

Major tidal constituents	Minor tidal constituents
M_2, S_2	K_2, N_2, O_1, P_1, K_1, Q_1

4.6 Currents and waterlevels

Waterlevel variations and current velocities from three gauge stations are available (see the locations in Figure 4.8). These data have been kindly provided by the partners at the University of Buenos Aires. The water level variations in Figure 4.9 and 4.10 were acquired from floaters named 'Oyarvide' (OYA) and 'San Clemente' (SCL). The components of the current velocity are measured at a buoy named 'Oceanor' (see Figure 4.8). Hourly measurements were available for February 1999.

Waterlevel variations at 8 m waterdepth at Oyarvide are shown in Figure 4.9. An oscilation in the graph indicates a tidal cycle. The maximal ebb amplitude is 1.2 m and the maximal flood amplitude is about 1.6 m. The flood amplitude of 1.6 m on February 8th corresponds to the wind event with speeds of more than 15 m/s. After February 15th when winds are moderate also the tidal amplitudes are lower with values between 0.5 and 1 m.

Figure 4.10 represents the waterlevel variations at the gauge station San Clemente at a water depth of about 20 m. The wind event on the February 8th has a similar impact on the waterlevel variation but not as strong as at the station Oyarvide inside the RdP.

The zonal component of the current velocity measured at the buoy Oceanor is illustrated in Figure 4.11. The zonal component is almost directed along the axis of the tidal river. Depending on the tidal cycle the u component of the current velocity increases up to 40 cm/s. The graph of meridonal component of the current velocities in Figure 4.12 shows a less regular progression. A strong peak to the positive is mostly followed by less strong peaks to the negative and vice versa.

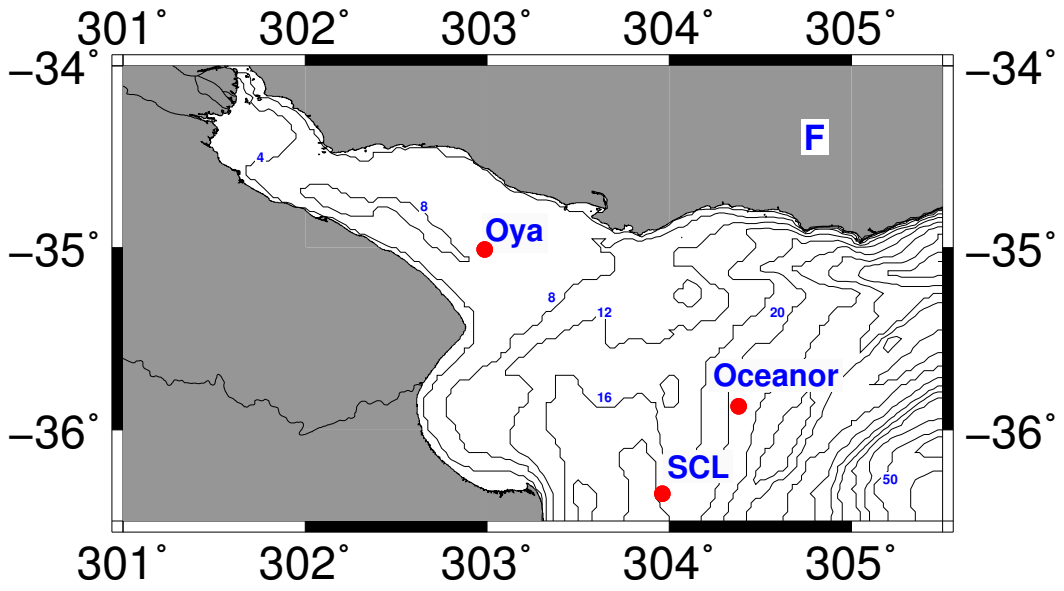

Figure 4.8: Hydrodynamic gauge stations - named Oyarvide (OYA), San Clemente (SCL), and Oceanor (numbers are depths in meters).

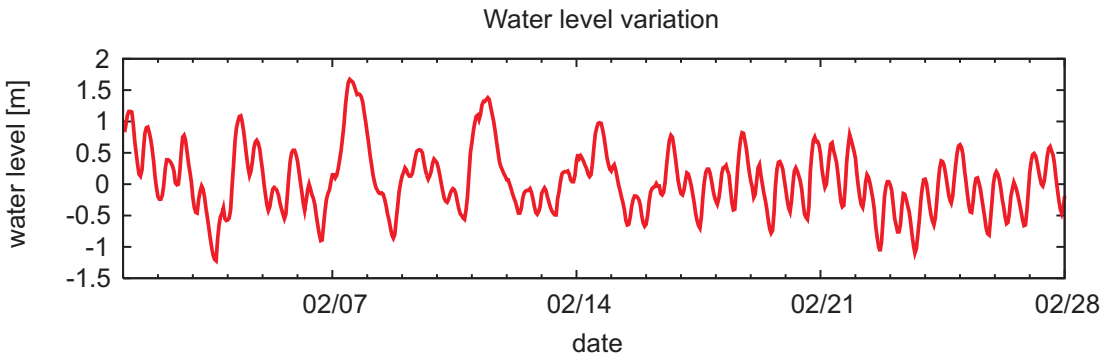

Figure 4.9: Waterlevel variations at gauge station Oyarvide in February 1999.

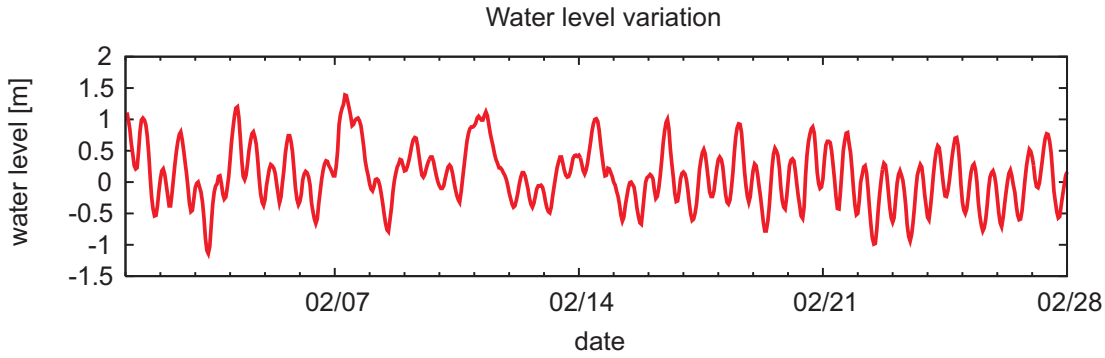

Figure 4.10: Waterlevel variations at gauge station San Clemente in February 1999.

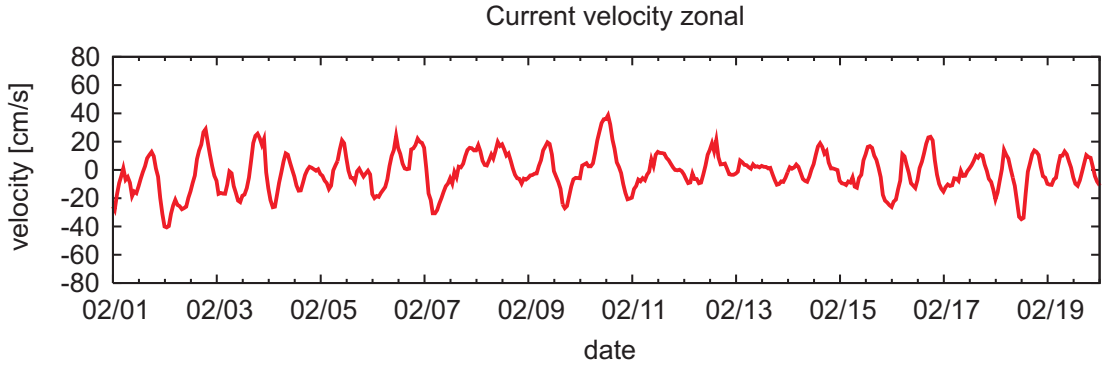

Figure 4.11: Zonal current velocities at buoy Oceanor in February 1999.

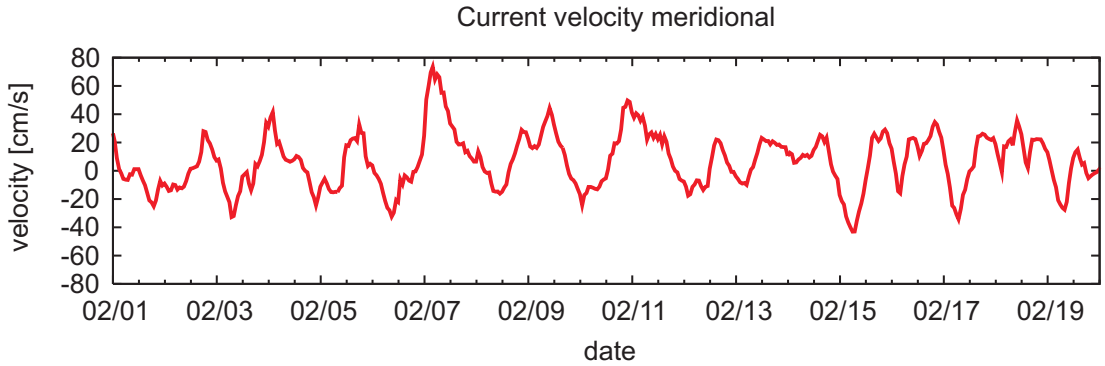

Figure 4.12: Meridional current velocities at buoy Oceanor in February 1999.

4.7 Wave data

Buoy measurements and altimeter data are available for the validation of the wave models.

4.7.1 Buoy

A directional wave rider buoy is placed in the entrance of the RdP (see Figure 4.14). The water depth at this position is about 15 m. The available data, kindly provided by the Servicio Hidrografico Naval in Buenos Aires, contains the wave parameters: significant wave height (H_s), $TM1$ period and wave direction in from 1996 to 2001. All data have passed a quality control, eliminating outliers H_s higher than 30 m as well as outlier $TM1$ periods larger than 20 seconds. The data set includes various gaps of irregular length. The time steps are irregular as well with an average of about 2-3 minutes. A statistical analysis in Table 7.4 gives an overview about wave conditions at the entrance of the RdP in the period from 1996 to 1999. The occurances of each quadrant were counted and assigned to the directions N, NE, E, SE, S, SW, W, NW. Mean values were calculated and maximum values identified. It can be stated that nearly 80% of the waves come from E-SE direction. From this directional range the highest waves enter with up to 4.55 m and also the long waves with $TM1$ periods up to 11 seconds.

Table 4.2: Statistical parameters of buoy measurements from 1996 to 2001.

		N	NE	E	SE	S	SW	W	NW	ALL
n		278	236	3161	4635	1603	537	418	407	11276
mean	H_s	1.07	1.10	1.17	1.06	1.37	1.69	1.44	1.13	1.41
	$TM1$	4.37	4.39	5.11	5.69	5.32	5.03	4.73	4.37	5.30
MAX	H_s	2.41	2.23	4.55	4.39	4.55	3.80	2.71	2.51	4.55
	$TM1$	7.94	5.34	9.83	11.23	9.75	7.63	6.48	7.03	11.23

4.7.2 Altimeter

Altimeter data obtained at the GeoForschungsZentrum (GFZ) in Potsdam/Germany are used for cross-checking the buoy measurements and for validating the results of the deep water wave model simulations. The obtained data were acquired with

the TOPEX/Poseidon (Menard *et al.*, 1995). This is a sensor placed on a satellite which sends and receives pulses to the earth. It has a return period of 10 days. The significant wave height is determined from the shape of the return pulse; a calm sea with low waves returns a condensed pulse, while rough seas with high waves return a long pulse.

A cross-check of buoy to altimeter has been performed. The reference data set contains 750 records from 1996 to 1999 of the buoy and corresponding records of the altimeter. Only data from tracks that passed the buoy with in 30 NM (tracks pass irregularly within a distance of 30 NM from the buoy) and 30 min with respect to the buoy observations have been included. The resulting scatter plot between buoy and altimeter wave heights is shown in Figure 4.13. Buoy and altimeter correlate with a coefficient of 0.89.

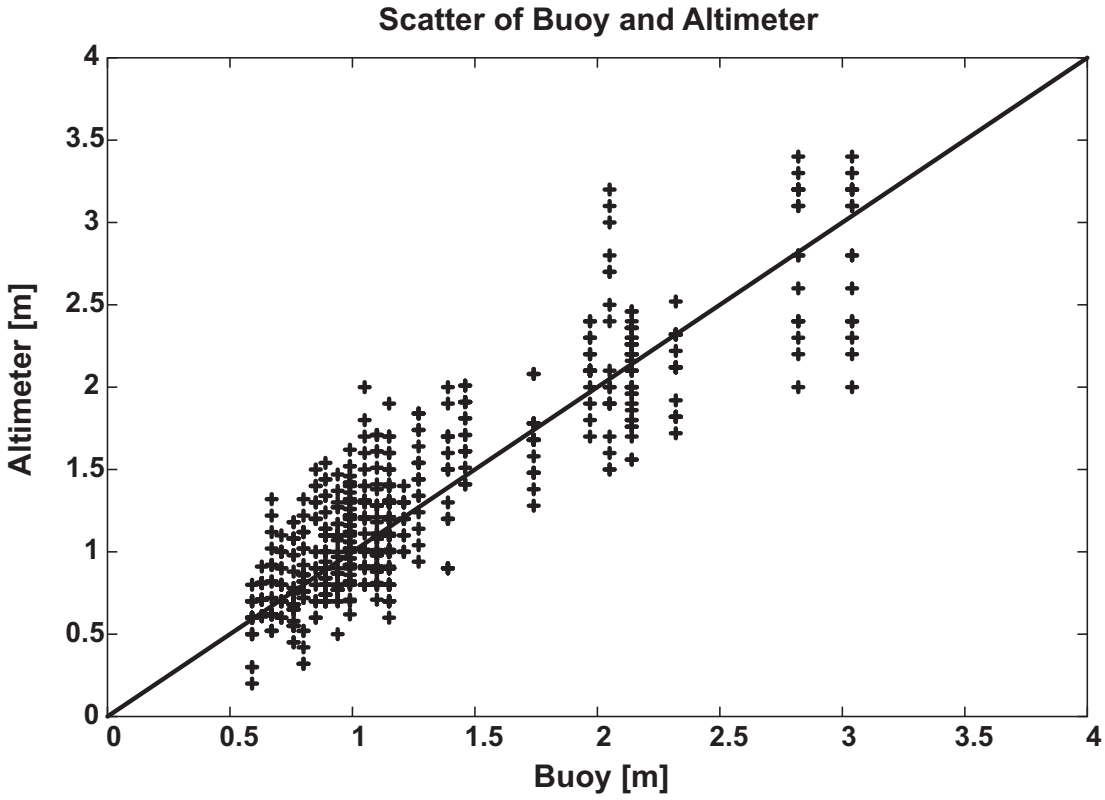

Figure 4.13: Significant wave height from buoy and topex altimeter for 750 coincidences.

In the time between October 20th and November 10th 1999, seven tracks of TOPEX/Poseidon served for the validation of deep water wave simulations (see

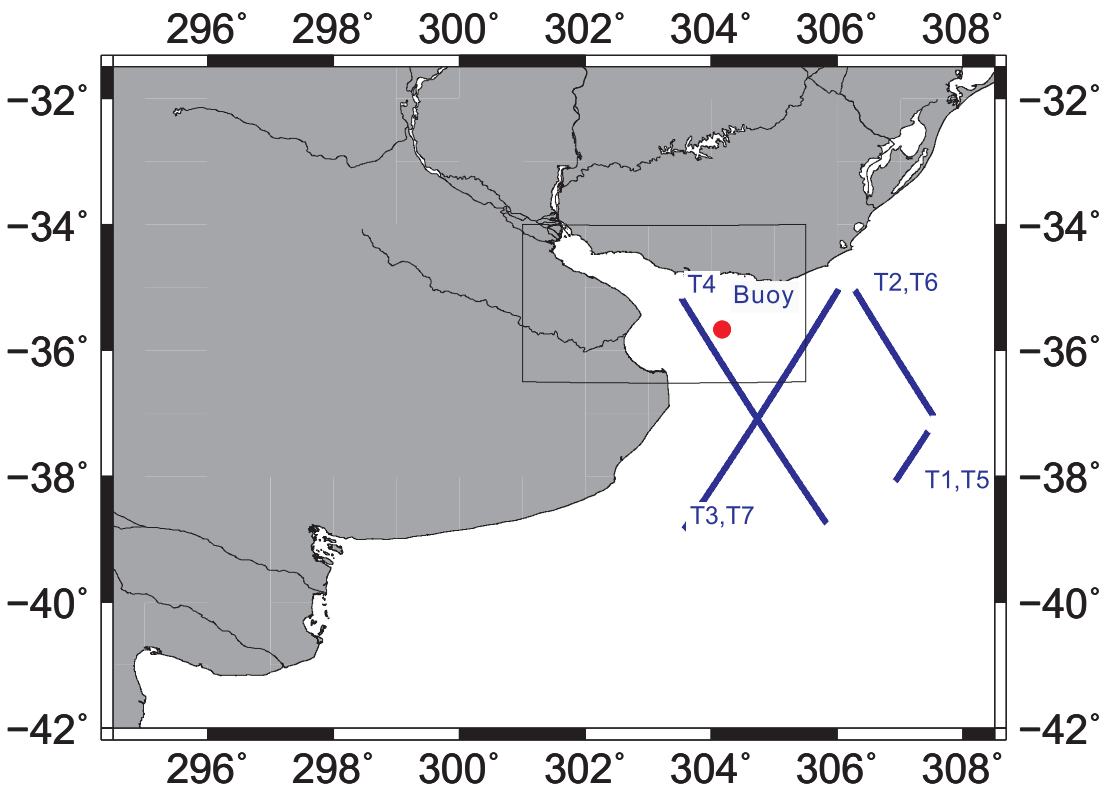

Figure 4.14: Position of the buoy and tracks of Altimeter for wave model validation - with fine grid boundary, T1-7 indicate the track numbers and the beginning of each track.

Figure 4.14). The tracks were chosen in fair distance to the coast in order to avoid land effects on pulse signal. The tracks are located in the entrance of the RdP but covered by the grid M. The wave simulations with the WAM wave model have been compared with these tracks. Track 1 - 7 have a chronological order. Due to a 10 day return period track 5 is on the same position as track 1, the same is valid for track 2 and track 6, as well as for track 3 and track 7. The beginning of each track is marked by the label placement in Figure 4.14.

4.8 Initial sediment distribution

In order to start the simulation with a realistic bottom coverage of sediments, the surficial sediment distribution map by Laborde (1987, 1997) and Parker *et al.* (1987) (see Figure 2.2) was digitized and a basic bottom coverage of SPM was

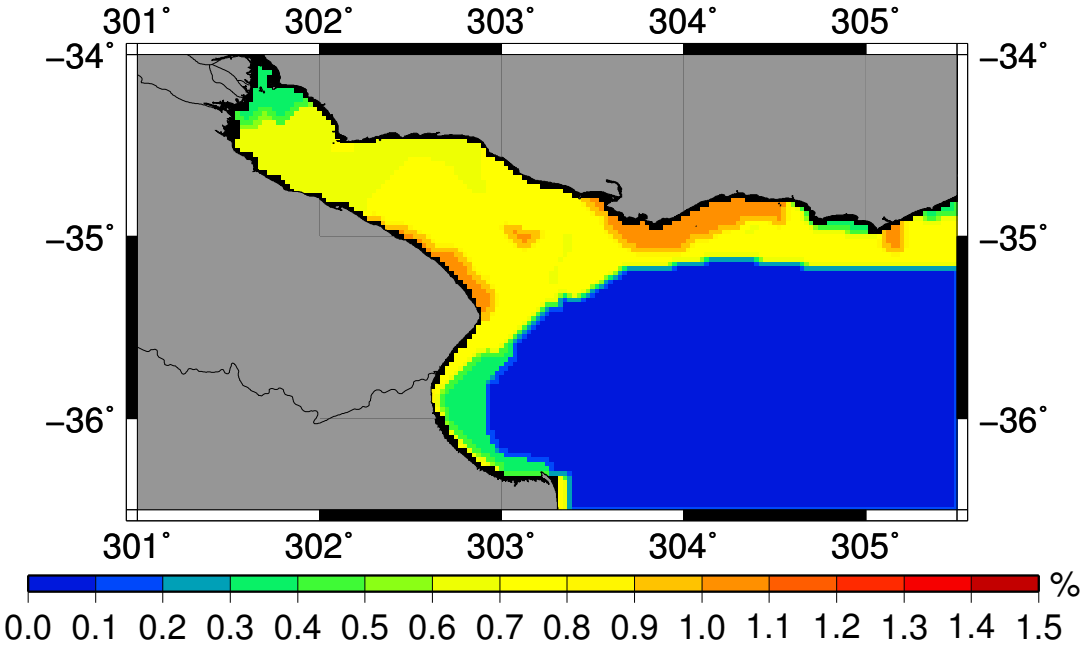

Figure 4.15: Initial bottom sediment distribution for the simulation.

generated from that. Figure 4.15 illustrates the fine sediment bottom coverage derived from the sediment distribution on the ground. The values given in this map are the percentage of SPM per unit sediment. The mass of a unit sediment on the bottom is unknown, it is assumed that the percentage of SPM in the bottom sediment is higher where the prevailing sediments are finer. Reference values for the assumptions come from the bottom coverage on the North Sea (Pleskachevsky *et al.*, 2003). The grain size used for the simulation is between 20 μm and 60μm.

4.9 SPM data

SeaWiFS (Sea-viewing Wide Field-of-view Sensor) (Hooker *et al.*, 1992) satellite data were found to be the only suitable data source for validating the SPM model. SeaWiFS was launched in August 1997. The instrument consists of an optical scanner and an electronics module. The nominal radiometric parameters for SeaWiFS are given in the Table 4.3.

SeaWiFS offers a local-area coverage (LAC) of 1 km resolution and a swath width of 2801 km. SeaWIFS provides Level 2 (L2) data which contain the geo-

physical parameters derived from the raw data. The software package SeaDAS (SeaWiFS GSFC, 2005) was applied to analyse and convert the L2 data into useful data for the present work. SeaDAS includes an algorithm to retreive Total Suspended Matter (TSM). TSM includes besides SPM organic fractions in suspension.

Table 4.3: SeaWIFS bands.

Band No.	Band Center (nm)	Potential applications
1	412	Dissolved organic matter
2	443	Chlorophyll absorption
3	490	Pigment absorption
4	510	Chlorophyll absorption
5	555	Pigments, optical properties, sediments
6	670	Atmospheric correction (CZCS heritage)
7	765	Atmospheric correction, aerosol radiance
8	865	Atmospheric correction, aerosol radiance

The Río de la Plata from the multispectral point of view: From the multispectral point of view the RdP is a typical Case 2 water. Case 2 waters go along with a number of problems in interpretation. Case 2 waters are mainly coastal waters or upwelling areas, where relatively high primary production and turbidity occurs. This can mislead the algorithms that are used to calculate optical properties and suspended sediment concentrations. Case 2 waters usually reflect more light than Case 1 waters which are open blue waters. Then the increased radiance can exceed the limits where the algorithms are most accurate. Although Case 2 waters and the conditions that cause them are known, the algorithms may return erroneous overestimates of the TSM concentration in these regions. This problem becomes obvious, where the blanked areas are, because the reflection of light from the sediments is so bright that they are interpreted

as clouds. The TSM concentration in such areas cannot be analyzed. Another problem is that because Case 2 waters are generally brighter (more reflective) than Case 1 waters, the atmospheric correction algorithms that rely on the fact that most ocean water is optically dark at certain wavelengths become less reliable. Furthermore, as already mentioned Case 2 waters are frequently found in coastal areas, the overlying atmosphere is also more muddled by terrestrial input, including smoke, the haze of pollution and dust. This makes atmospheric correction more difficult as well.

The atmospheric correction problem: The SeaWiFS atmospheric algorithm was developed by Wang & Gordon (1994). The atmospheric correction is the removal of atmospheric effects from the sensor-measured radiance and requires the information of atmospheric optical properties which are not always available. Therefore, the correction normally relies on the satellite-derived data alone. The algorithm uses band 870 nm and 765 nm (red and near-infrared). In Case 1, the ocean can be taken as black surface (Wang, 1999). From those two bands the aerosol reflectance is extrapolated to shorter wavelengths. This approach has proven to be useful for relatively clear water. In Case 2 water this approach is not successful (Ruddick *et al.*, 2000). Due to the fact that no data of discharge after 1999 were available no more advanced sensors and algorithms could be applied. The standard algorithm of the SeaDas software package (SeaWiFS GSFC, 2005) has been used to interprete the L2 data and has not yet implemented an improved atmospheric correction for Case 2 waters.

Reference images: For the selected simulation period, 15 images were available. Only the best image for each month from August to December 1999 was selected for the comparison. The reference images are shown in true-color in Figure 4.16 on the left. The right side shows the computed Total Suspended Matter (TSM) concentrations in the RdP computed with the SEADAS Software package. This software offers algorithms for the computation of Total Suspended Matter in units of mg/l (TSM). The computation of TSM concentrations includes the atmospheric correction. The labels of the images are the dates with the format: YearDayoftheyearHourMinuteSecond. Table 4.4 explains the meteorological and hydrographical situation at the time the pictures were taken.

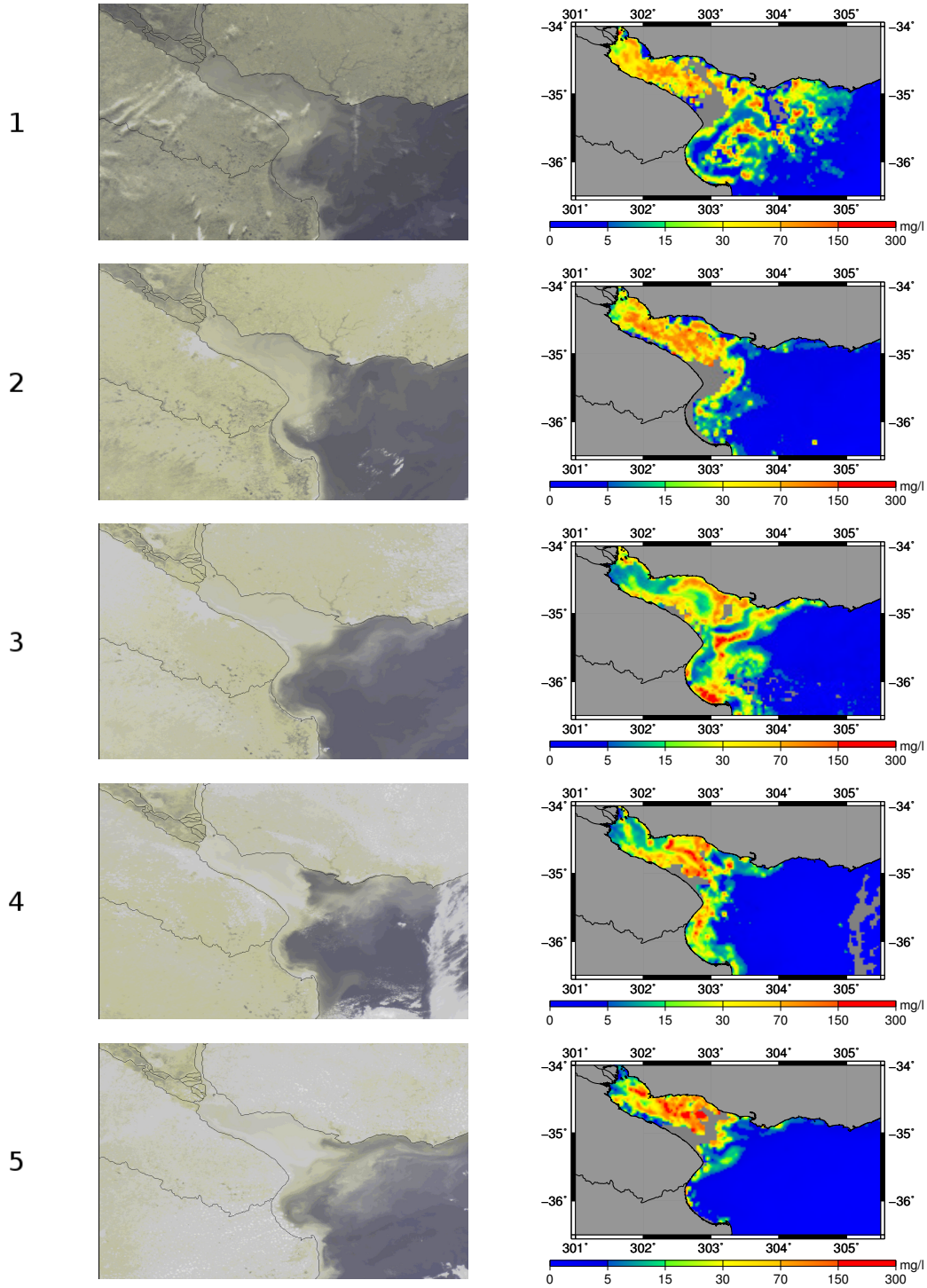

Figure 4.16: Reference images: Quasi True-color (left) and SeaWIFS TSM in mg/l (right).

Table 4.4: Meteorological and hydrological situation at date the images were taken.

Image	Label	Date	Wind	Discharge
1	S1999214152231	August 2nd 1999	5 m/s from W	23000 m^3/s
2	S1999265151314	September 22nd 1999	14 m/s from NE	18500 m^3/s
3	S1999290153339	October 17th 1999	5 m/s turning	18000 m^3/s
4	S1999325150315	November 21th 1999	10 m/s from SE	14500 m^3/s
5	S1999341151756	December 7th 1999	5 m/s from E	14000 m^3/s

Difficulties in data acquisition: The acquisition of in-situ SPM data in the RdP was very difficult. Generally, it must be mentioned that there are data available, however, they are rare and very difficult to obtain. Having established contact to both major universities, the University of Buenos Aires (Argentina) and the University of Montevideo (Uruguay), none of them could provide SPM in-situ data or connect to other institutions who possess adequate data. Therefore, the only SPM data available were satellite images from SeaWiFs. Due to this fact, the time frame for the simulations could only be set to the year 1999 and no other, more sophisticated sensors could be used.

Chapter 5

Model System

5.1 Hydrodynamic model

Current and tide simulations are realized with the Hamburg Shelf Ocean Model (HamSOM, Version CIMA), developed by Backhaus (1983, 1985) of the Institute of Oceanography at the University of Hamburg in Germany. This model was applied in a number of sites around the world and demonstrated to be suitable to simulate the hydrodynamics associated to continental shelfs (Backhaus & Hainbucher, 1987; Rodriguez *et al.*, 1991; Stronach *et al.*, 1993; Simionato *et al.*, 2001). This model is already described in a number of publications by Backhaus (1983, 1985); Backhaus & Hainbucher (1987); Rodriguez *et al.* (1991); Stronach *et al.* (1993). A brief review of the model is given here. The HamSOM is a three-dimensional, baroclinic model based on the Reynolds equations:

$$\begin{aligned}
\frac{\partial u}{\partial t} + u\frac{\partial u}{\partial x} + v\frac{\partial u}{\partial y} + w\frac{\partial u}{\partial z} + \frac{1}{\rho}\frac{\partial \rho}{\partial x} &= fv + A_h\left[\frac{\partial^2 u}{\partial x^2} + \frac{\partial^2 u}{\partial y^2}\right] + \frac{\partial \tau_x}{\partial z} \\
\frac{\partial v}{\partial t} + u\frac{\partial v}{\partial x} + v\frac{\partial v}{\partial y} + w\frac{\partial v}{\partial z} + \frac{1}{\rho}\frac{\partial \rho}{\partial x} &= -fu + A_h\left[\frac{\partial^2 v}{\partial x^2} + \frac{\partial^2 v}{\partial y^2}\right] + \frac{\partial \tau_y}{\partial z}
\end{aligned} \tag{5.1}$$

u and v are the components of the velocity vectors, t is the time, ρ is the water density, f is the Coriolis frequency, τ_x and τ_y are the components of the wind stress vector and A_h is the horizontal turbulent viscosity. The governing equations are completed by adding the equation of continuity and the hydrostatic formula:

$$\frac{\partial u}{\partial x} + \frac{\partial v}{\partial y} + \frac{\partial w}{\partial z} = 0 \tag{5.2}$$

$$\frac{\partial \rho}{\partial z} = -\rho g \tag{5.3}$$

with g the acceleration of gravity. Further details to the model physics can be taken from Backhaus (1985).

5.2 Wave model

WAM Cycle 4.5 and K-Model were applied to simulate waves. WAM points out its strength in deep water and shallow water up to 15 m water depth. The K-Model can be used for very shallow waters. Both, WAM and K-Model are discrete spectral wave models solving the action balance equation. The K-Model solves the action balance equation in wave-number and direction coordinates (k, θ) as independent variables. WAM applies an equivalent notation in frequency-direction space (σ, θ) (Günther *et al.*, 1992). The action balance equation in k-space is:

$$\partial_t N + \partial_x(\dot{x}N) + \partial_k(\dot{k}N) + \partial_\theta(\dot{\theta}N) = S(N) \tag{5.4}$$

where $S(N)$ is the source function describing the energy inputs and dissipation sources of the wave action density N defined as:

$$N = E/\sigma \tag{5.5}$$

with the wave energy density E and the intrinsic frequency σ determined by the dispersion relation:

$$\sigma^2 = gktanh(kh) \tag{5.6}$$

with h the water depth.

N, E and σ are functions of the wave vector coordinates (k, θ) for the K-Model and (f, θ) for the WAM as well as the location x and the time t.
The spectrum of waves can be either represented as a wave-number-direction spectrum $F(k, \theta)$ (K-Model) or a frequency-direction spectrum $E(f, \theta)$ (WAM). WAM and K-Model apply different approaches for the source function. While WAM includes exponential growth due to wind input (S_{in}), dissipation due to white capping (S_{dis}) and nonlinear transfer (S_{nl}) and dissipation by bottom fric-

tion (S_{bo}) in the source function:

$$S(N) = S_{in} + S_{dis} + S_{nl} + S_{bo} \tag{5.7}$$

the K-Model uses the source function as:

$$S(N) = S_{ph} + S_{in} + S_{dis} + S_{bo} \tag{5.8}$$

with S_{ph} Phillips linear growth of waves due to wind, S_{in} Snyder exponential growth, S_{dis} dissipation by turbulent diffusion and white capping, and S_{bo} dissipation by bottom friction. The main difference between the K-Model to the WAM is the application of a nonlinear dissipation source term introduced by Rosenthal (1995) based on the concept of turbulent diffusion. The bathymetric inhomogeneity and currents in coastal environments justifies to use a nonlinear dissipation function as key mechanism and to neglect internal nonlinear interactions of waves according to the theory of Hasselmann (1962). Integrated wave parameters used through the present work are significant wave height H_s, $TM1$ period and the wave direction θ. All values are related to the computed wave spectrum $E(f, \theta)$;

$$H_s = 4\sqrt{m_0} \tag{5.9}$$

and

$$TM1 = \frac{m_0}{m_1} \tag{5.10}$$

with m_0 the zeroth and m_1 the first momentum of a wave spectrum derived from:

$$m_i = \int E(f, \theta)\, f^i \, df \, d\theta \tag{5.11}$$

with f^i the frequency in the momentum i (Demirbilek & Vincent, 2003).

5.3 SPM model

Annotation: In this work the expression 'SPM on or in the bottom' is used. This might be confusing since particles on the bottom are not in suspension but deposited. However, since this deposited sediment will be available for resuspension, the expression will not be changed in order to not cause confusion although

it can be considered incorrect.

SPM model basics: The SPM model is a transport model for suspended sediments in three dimensions (Pleskachevsky *et al.*, 2001, 2002, 2003). It applies the transport modules of the Eulerian dispersion model of the BSH (German Hydrographic Service) (Kleine, 1993). In extension, modules to compute the vertical exchange processes of SPM in the water column induced by currents and waves have been introduced. The sedimentological processes erosion, sedimentation, resuspension, diffusion and bioturbation are considered within that module (Gayer *et al.*, 2004).

The computations are performed for three fractions of SPM which differ in the parameters of settling velocity and initial spatial distribution. With the initial distribution of SPM on the bottom, mentioned in Chapter 4, an initialization program generates an initial state of SPM content of the fractions in two bottom layers of 10 cm thickness $z3$ and $z4$ described in the Figure 5.1. Fraction 1 and fraction 2 have a mass ratio of 9:1. The settling velocities of fraction 1 u_{sink1} (0.0001 m/s) and of fraction 2 (mainly fluvial sediments) u_{sink2} (0.00002 m/s) are based on measurements by Puls *et al.* (1995). The heaviest fraction is fraction 3 with a settling velocity u_{sink3} of 0.001 m/s. It follows a sineformed distribution according to the sum of fraction 1 and 2. The mass of SPM M_k^B (kg/m^2) in $z3$ and $z4$ is:

$$M_3^B = \rho_{sed}\,\mu\,z_3\,,\; M_4^B = \rho_{sed}\,\mu\,z_4 \tag{5.12}$$

with the bottom layer k, the percentage of SPM in the sediment μ and the sediment density $\rho_{sed}\,(1200\,kg/m^3)$. The initialization also generates a depth-dependent SPM distribution in the water column.

5.3.1 Sedimentation, resuspension and erosion

The model physics are based on the physical processes of sediment transport as described by Soulsby (1997). The critical shear velocity is introduced for the determination erosion, sedimentation and resuspension. Figure 5.2 shows the occuring processes depending on the shear velocity u^*. The values for u^* of sedimentation, resuspension and erosion are based on numerous experiments and

N	Layer	Material		Process	
1	upper most water layer	SPM concentration C_1	H_1	sinking ↓	transport ←→ vertical exchange ↑↓
k		C_k	H_k		
kb	lower most water layer	C_{kb}	H_{kb}	sedimentation ↓	
z1	upper most 20 cm of the bottom	SPM mass M_1^B	∼0-1 mm	resuspension ↑	bioturbation ↓ diffusion ↑↓
z2		SPM M_2^B sand	h_{ero} (0-10 cm)	erosion ↑	
z3		SPM M_3^B sand	10 cm - h_{ero}		
z4		SPM M_4^B sand	10 cm		

Figure 5.1: SPM scheme - exchange processes and bottom and water layers.

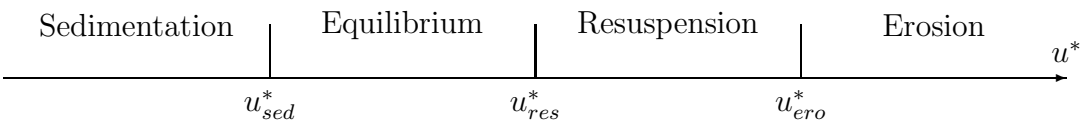

Figure 5.2: Processes depending on the shear velocity u^*.

can be seen in the following chapter 6 .

Erosion: Depending on currents and wave energy, the shear velocity u^* in the lower most waterlayer is computed which induces an erosion, if it goes beyond the critical shear velocity u^*_{ero}. This leads to disengagement of suspended material out of bottom layer $z3$ to an erosion depth h_{ero}. After the erosion process the bottom layer $z2$ is empty. In the course of the simulation bottom layer $z2$ is filled with SPM by diffusion and bioturbation processes.

Sedimentation: Sedimentation takes place when u^* decreases below the critical value for sedimentation u^*_{sed}. Suspended material in the lowermost water layer is deposited in bottom layer $z1$. The mass of deposited material is computed from the concentration of SPM in the lowermost water layer depending on the shear velocity and the settling velocity of the sediment. Bioturbation processes change the content of fine sediments in the present and its underlying layers instantaneously and gradually (in the order of a few days), respectively.

Resuspension: An increase of u^* leads to resuspension of the material deposited in bottom layer $z1$. The critical shear velocities of sedimentation u^*_{sed} and resuspension u^*_{res} differ slightly. Between those an equilibrium exists, implying that there is no exchange between the bottom and the water column. Exceeding u^*_{res} means that the material in $z1$ is resuspended.

The active shear velocity u^* is computed from the maximal shear stress τ:

$$u^* = \sqrt{\tau/\rho} \quad (m/s), \tag{5.13}$$

where ρ is the mean density of water ($1000\,kg/m^3$). The shear stress τ is the sum

of the components arising from waves and currents:

$$\tau = \sqrt{(\tau_m + \tau_{wave}\, cos\phi)^2 \,+\, (\tau_{wave} sin\phi)^2} \quad (kg/s^2/m). \tag{5.14}$$

ϕ is the angle between current direction and wave direction and τ_m the mean shear stress:

$$\tau_m = \tau_{cur} \left[1 + 1.2 \left(\frac{\tau_{wave}}{\tau_{cur} + \tau_{wave}} \right)^{3.2} \right] \quad (kg/s^2/m). \tag{5.15}$$

The current component of the shear stress τ_{cur} is defined by:

$$\tau_{cur} = \rho\, C_D\, \bar{U}^2 \quad (kg/s^2/m) \tag{5.16}$$

with the mean current velocity in the lowermost water layer $\bar{U}$ and the friction coefficient C_D defined by:

$$C_D = 0.16 \left(1 + ln \left(\frac{Z_0}{\Delta H_{kb}} \right) \right)^{-2} , \tag{5.17}$$

where ΔH_{kb} is the thickness of the lowermost water layer in meters, $Z_0 = d_{50}/12$ is the roughness length in meters and d_{50} the grain size. The wave component of the shear stress is determined as:

$$\tau_{wave} = 0.5\, \rho\, f_w\, U_w^2 \quad (kg/s^2/m) \tag{5.18}$$

with the orbital velocity above the bottom U_w:

$$U_w = \frac{\pi H_S}{T sin(kh)} \quad (m/s) \tag{5.19}$$

with the significant wave height H_S, the peak period T, the wave number k and the water depth h. The determination of the roughness coefficient f_w is done by $max(f_{wr}, f_{ws})$, with f_{wr} = coefficient for rough bed friction and f_{ws} = coefficient for smooth bed friction:

$$f_{wr} = 0.237 \left(\frac{A}{k_s} \right)^{-0.52} , \; f_{ws} = B\, R_w^{-N} \tag{5.20}$$

with $k_s = 2.5\, d_{50}$ is the Nikuradse grain roughness. $A = U_w T/2\pi$ is the semi-axis

length of the orbital movement in meters. In case of smooth bed roughness the parameter of the roughness coefficient f_{ws} differs between laminar and turbulent flows:
$B = 2\,,\ \ N = 0.5\ \ for R_w \leq 5 \cdot 10^5$ (laminar),
$B = 0.0521\,,\ \ N = 0.187\ \ for R_w \gg 5 \cdot 10^5$ (turbulent).
For differentiation the Reynolds number R_w is computed:

$$R_w = \frac{U_w A}{\nu} \tag{5.21}$$

where ν is the kinematic viscosity ($0.0000012\ m^2/s$).

Once the shear stress τ and the corresponding shear velocity is u^* are computed, they are compared with the critical shear velocities for erosion, deposition and resuspension. Depending on the occuring process the change of mass is computed in the corresponding bottom and water layers. In the case of erosion, the erosion depth is computed depending on the shear velocity. In the case that the actual erosion depth is larger than the old one, new material from layer $z3$ can be eroded. In case of a smaller erosion depth, only layers $z1$ and $z2$ are resuspended and eroded, respectively. The erosion depth to where SPM is fully removed is computed as:

$$h_{ero} = K_{ero} \frac{u^{*2} - {u^*_{ero}}^2}{{u^*_{ero}}^2} \quad (m). \tag{5.22}$$

K_{ero} is a constant of the order of 0.001 m. It was determined by test computations by Pleskachevsky *et al.* (2001) in the North Sea by analysis of satellite data. In case of sedimentation, the mass of sediment per square meter ΔM^{SED} from the lowermost water layer which makes up bottom layer $z1$ is computed as:

$$M^{SED} = C_{kb}\, u_{sink} \left[1 - \left(\frac{u^*}{u^*_{sed}}\right)^2\right] \quad (kg/m^2/s). \tag{5.23}$$

C_{kb} is the SPM concentration in kg/m^3 in the lowermost water layer kb and u_{sink} is the settling velocity of the sediment.

5.3.2 Bottom processes

SPM covers the bottom, forms the uppermost bottom layer $z1$ and is transported by benthic organisms downwards. Due to bioturbation all deposited SPM would

be distributed - excluding other processes - during the time Z_A (in the model 7.23 days) to the bottom layers $z2$ and $z3$. The diminishion of SPM in the uppermost bottom layer in the time Δt is computed with:

$$\Delta M_1^B = \frac{\Delta t}{Z_A} M_1^B \quad (kg/m^2) \tag{5.24}$$

This SPM is distributed to the bottom layers $z2$ (thickness = $h_{empty} = h_{ero}$ of $t-1$) and $z3$ (thickness = $z3_0$ ($z3$ at $t=0$) - h_{empty}) and is corrected with the portions due to diffusion because of concentration differences ΔM^D as follows:

$$\Delta M_2^B = \Delta M_1^B \frac{h_{empty}}{z_0^3} + \Delta M_{3\to 2}^B \quad (kg/m^2) \tag{5.25}$$

$$\Delta M_3^B = \Delta M_1^B \frac{z3_0 - h_{empty}}{z_0^3} - \Delta M_{3\to 2}^D \begin{pmatrix} +\Delta M_{4\to 3}^D \\ -\Delta M_{3\to 4}^D \end{pmatrix} \quad (kg/m^2). \tag{5.26}$$

The quantity resulting from diffusion between bottom layer k and $k-1$ is calculated with the diffusion equation:

$$\Delta M_k^D = \frac{A_{DIF}(C_k^B - C_{k-1}^B)z_k}{(0.5(z_k + z_{k-1}))^2}\Delta t \quad (kg/m^2) \tag{5.27}$$

where A_{DIF} is the diffusion coefficient and Δz the appropiate distances between the centers of the bottom layers. The value of A_{DIF} results from model tuning in the North Sea region and is listed in the parameter table in the model setup in the following chapter.

5.3.3 Vertical exchange in the water column

The variation of mass of SPM in a water layer with the thickness Δh by vertical exchange over the length Δz is computed as:

$$\Delta M = \frac{A_v \Delta C \Delta h}{(\Delta z)^2} \tag{5.28}$$

with ΔC = the concentration gradient between two neighbouring layers. The distance between the center points of the layers is defined by the length Δz. The

exchange A_v is the sum of a current and a wave component:

$$A_v = A_v^{cur} + A_v^{wave} \quad (m^2/s) \tag{5.29}$$

The wave component A_v^{wave} is computed as:

$$A_v^{wave} = Ak_{wave}\, U_{z_k}^{ORB^2}\, T \quad (m^2/s) \tag{5.30}$$

where T is the wave period and z_k the thickness of layer k. The orbital velocity is determined depth-dependent:

$$U_k^{ORB} = \frac{\pi\, H_s}{T} \frac{cosh(k(h - z_k))}{sinh(kh)} \quad (m/s) \tag{5.31}$$

and the wave-dependent exchange coefficient is computed as:

$$Ak_{wave} = (kH_s)^2 \quad (m^2/s) \tag{5.32}$$

with T the wave period, H_s the significant wave height, k the wave number and z_k depth to the center of layer k.

The current component A_v^{cur} is proportional to the shear current:

$$A_v^{cur} = Ak_{cur}^2 \frac{dU}{dz} = \left(\frac{U_k^2}{g}\right)^2 \frac{|U_{k-1} - U_{k+1}|}{h_k + 0.5\,(h_{k-1} + h_{k+1})} \quad (m^2/s) \tag{5.33}$$

with $h_k = k^{th}$ water layer thickness and Ak_{cur} Prandls mixing length. Ak_{cur} is defined as the way that a water particle needs for diffusion from one layer to another where the particle adopts the new kinematic features. In the lowermost water layer $k = k_b$ the current velocity U_{k+1} is set to zero. The maximum exchange is reached when during a storm all water layers are mixed.

5.3.4 Sinking of SPM

In all water layers except the lowermost where sinking is described as sedimentation (see equation 5.23) sinking in the water layer as mass exchange between the water layers during the time Δt is:

$$\Delta M_k^W = C_k^W\, w_{sink}\, \Delta t \quad (kg/m^2) \tag{5.34}$$

with the settling velocities of the three SPM fractions w_{sink}. The new concentrations of SPM in the water layers of thickness h_k therefore are determined as:

$$\begin{cases} C_k^W = (C_k^W)_{alt} - \frac{\Delta M_k^W}{h_k} & (kg/m^3) \\ C_{k+1}^W = (C_{k+1}^W)_{alt} - \frac{\Delta M_k^W}{h_{k+1}} & (kg/m^3) \end{cases} \tag{5.35}$$

The vertical exchange processes are performed with these procedures. The horizontal exchange is performed with the flow module of the BSH model but extended in order to transport three SPM fractions independently.

5.3.5 Computation of the horizontal distribution of SPM

The horizontal distribution of the three fractions in the water column is computed with the current components (Kleine, 1993). In the computation of horizontal transport also the river discharge is considered.

5.3.6 Flocculation

After collision, fine grained minerals aggregate to flocs. Flocs are usually a mixture of inorganic and also organic matter (Eisma & Cadee, 1991). Turbulence is seen as mayor influencing factor on floc growth and floc breakup (Winterwerp, 1999). Flocculation induced by turbulence is included into the applied SPM model for the first time. Three new fraction have been introduced. At low turbulence, the first three fractions n (1, 2, 3) convert to the new fractions $n+3$ (4, 5, 6). The amount of the concentration which converts from fraction n to fraction $n+3$ is defined by:

$$\Delta C_n = \Delta t \frac{1}{A_f} C_n \tag{5.36}$$

in which Δt is the time step of the model and A_f is a floc growth constant defined by:

$$A_f = 24 * 60 * 60 \ (s) \tag{5.37}$$

The value of the constant results from tests. At high turbulence, the fractions $n+3$ break up instantanously and convert to fraction n. Flocculation and floc breakup is defined over the floc parameter P_F:

$$P_F = \frac{1 + aG}{1 + bG^2} \tag{5.38}$$

which indicates flocculation if $P_F > 1$ and floc breakup if $P_F < 1$ (Dittschke *et al.*, 2005). The empircal derived constants a and b are defined by van Leussen (1994) with $a = 0.3$ and $b = 0.09$ for the Ems estuary. G is the root mean square velocity gradient:

$$G = \sqrt{\frac{\varepsilon}{\nu}} \qquad (1/s) \tag{5.39}$$

defined as the square root of energy dissipation at a point divided by the kinematic viscosity ν. The energy dissipation ε is defined by:

$$\varepsilon = \frac{4}{3\pi}\frac{g}{hC_C^2}u^3 \qquad (J/s/kg) \tag{5.40}$$

Here, g is the acceleration of gravity, h is the water depth and C_C is the Chezy coefficient:

$$C_C = \sqrt{\frac{g\rho u^2}{\tau_B}} \qquad (m^{\frac{1}{2}}/s) \tag{5.41}$$

in which τ_B is the shear stress on the bottom and u the mean flow velocity. The settling velocities for the fractions $n + 3$ (4, 5, and 6) are constant. As soon as the material of the fractions $n + 3$ (4, 5, and 6) reaches the bottom it breaks up and is converted to the fractions n (1, 2, 3). The knowledge of Winterwerp (1999) and van Leussen (1994) that settling velocities have a temporal variablity and should not be constant, is present but not yet implemented in the this work.

Chapter 6

Model setup

6.1 Setup of the hydrodynamic model

Due to insufficient measurements along the boundaries of the area of interest, the HamSOM works with a unidirectional nesting. Three grids C_{cur} (coarse), M (medium) and F (fine) are introduced. The grid extensions and resolutions can be reviewed in Table 3.1 in Chapter 3.2. In the vertical, the model is resolved with 10 layers. 10m, 20m, 40m, 60m, 100m, 200m, 500m, 1000m, 3000m and 6000m are marked as the lower limits of each layer. The minimal layer depth for C_{cur} is 5 m, due to the fact that this version of the model does not recognize dry points. For depth less than 5 m grid points could fall dry and the model aborts. Vertical discretization was selected to obtain a good resolution of the upper water masses and resolve the circulation driven by the wind force. The model based on grid C_{cur} simulates the conditions over the sea shelf outside the domain of grid M. Grid M is resolved vertically by 13 layers (at 7m, 10m, 15m, 20m, 25m, 50m, 100m, 250m, 1000m, 2000m, 3000m and 5500m depth). The minimal layer depth for M is 4 m. Although the depth of the upper layer is too large to resolve adequately the shallow water areas of the domain it is selected to resolve the southeasterly part of the domain, where the amplitudes of the tides are high. Finally, the grid M determines the conditions along the borders of grid F. 12 layers are defined for F with bottoms marked at 3m, 4m, 6m 8m, 10m, 14m, 18m, 24m, 30m, 40m, 50m, 55m. The discretization permits a good vertical resolution in the estuary. The minimal depth of layer thickness is set to 2m. The model in C_{cur} was driven only by tidal input. The eight most important

constituents M_2, S_2, K_2, N_2, O_1, P_1, K_1 and Q_1 were introduced. Subroutines which incorporate the computation of the constituents have been introduced to the model by Simionato *et al.* (2001) in order to realize a correction in the phase and the aplitude of the tide per date. Wind and discharge have been included as model drivers in grids M and F. The HamSOM saved output data every 30 minutes to be used in the wave models and in the SPM model.

6.2 Setup of the wave model

Wave action in the RdP depends very much on the generation of swell on the South Atlantic Ocean. Figure 4.6 in Chapter 4.3 shows a wind situation with prevailing easterly winds over a high fetch to the area of interest. The decision to run the wave models in three nested domains arose due to the fact that storms and continuous windfields on the open South Atlantic Ocean produce high waves that can travel large distances. A second, medium grid is set up in order to combine deep sea and a better resolved shallow water area west of the shelf. The finest grid contains the high resolution of the area of interest. Thus the WAM model runs in deep water mode on grid C_{wav} in Figure 3.2. Wave spectra output of the C_{wav} grid will be available as open boundary conditions to the grid M. There the WAM is set up in shallow water mode with depth refraction included. In grid C_{wav} the wind is the only driver of the system. In grid M, the drivers are wind and boundary spectra generated on grid C_{wav}. Boundary spectra generated by grid M, wind, currents and water level variations drive the K-Model, which is applied in shallow water mode using depth and current refraction.

- The models are set up on three grids. The WAM is setup on grid C_wav, M and F. The K-Model is setup on grid F.
- Due to Schneggenburger (1998) the consideration of variable water depth and currents give a significant improvement of wave model results in shallow water areas where tidal currents have strong influence on the sea state. Variable water depth and current fields are saved every 30 minutes to be used in the F grid of WAM and K-Model.
- The spectral resolution of the K-Model is 24 direction bins ranging from 0 to 360 and 28 wavenumber bins starting from 0.01 rad/m logarithmic scaled

with a factor of 1.24. The WAM has also been adapted to 24 direction bins and corresponding 28 frequency bins, starting from 0.04 Hz scaled with a factor 1.1.

- Propagation time steps in grid C_wav were 10 minutes, and in grid M, 2 minutes. In order to not violate the stability criteria, in grid F the propagation time step was set to 1 minute.

- Wave spectra from a previous coarse grid run indicate the boundary conditions on the domain limits of grid M and grid F, respectively. Grid M receives on 49 grid points spectra from the previous C_wav grid run and provides spectra on 39 grid points to grid F.

6.3 Setup of the SPM model

6.3.1 Initial distribution

The SPM-Model requires an initial distribution for SPM in the water column and on the bottom. The generated SPM bottom coverage (see Chapter 4.8, Figure 2.2) was the base to initialize the model and set up the initial spatial distribution of SPM in the bottom layers and in the water column.

6.3.2 Parameter setup

The parameter setup mentioned in the model description is the setup resulting from North Sea experiments. The same setup with the parameters presented in Table 6.1 is also used in the experiments in the present work due to the fact that no more reliable values were present.

6.3.3 Tests and case studies

The SPM model offers multiple options to change parameters and to tune the model. In the present work only a limited number of options could be considered and calculated. The simulations of SPM are still based on many assumptions where data are not available or insufficient. The following paragraphs present some attempts to improve the simulation results.

Table 6.1: Important parameters for SPM simulation - North Sea setup.

Parameter	Value	Unit	Description
d_{50}	0.00025	m	median grain diameter
z_0	$d_{50}/12$	m	bottom roughness
ν	0.0000012	m^2/s	kinematic viscosity
u^*_{res}	0.01	m/s	criticial shear velocity for resuspension
u^*_{ero}	0.028	m/s	criticial shear velocity for erosion
u^*_{sed}	0.0099	m/s	criticial shear velocity for deposition
u_{sink1}	0.0001	m/s	settling velocity fraction 1
u_{sink2}	0.00002	m/s	settling velocity fraction 2
u_{sink3}	0.001	m/s	settling velocity fraction 3
za	0.0000016	$1/s$	bioturbation constant
A_{DIF}	0.0000000003215	m^2/s	vertical exchange coefficient of the diffusion in bottom layers 2, 3 and 4

Disregard of waves The disregard of waves is an option to show the reader the dimension of the wave effect in SPM simulations. In this context also the effect of the waves on erosion can be identified.

SPM input concentrations No data of SPM input concentration was available.
Depetris & Paolini (1991) mentioned that for the Rio Paraná at a mean discharge of 15,000 m^3/s a concentration of suspended solids is 170 mg/l. This relation was adopted as basis for the present investigation. The SPM concentration is computed from the available discharge data based on this ratio and changes in time depending on the discharge. For testing purposes the ratio was decreased to 15,000 m^3/s and 70 mg/l, then increased to 15,000 m^3/s and 270 mg/l.

SPM sources Originally, a single fluvial SPM source is set. On that point the entire mass of sediment load of the two rivers Uruguay and Paraná enters the RdP in each time step. The Paraná is a delta and consists of many various delta braces. For testing purposes a second river source is implemented at the outlet of another large brace of the Paraná river. The intention is to test for the development of different distribution patterns and for the influence on the form

of the turbidity front. In case of one outlet, 100% of the discharge goes through point S1. For simulations with two outlets, 75% is discharged at S1 and 25% at S2. The available data base on point S1 are simply split into 75% and 25%, respectively. The points S1 and S2 are visualized in Figure 6.1. The percentages of 75 and 25 are not based on detailed information. They are arbitrary values since no other data are available.

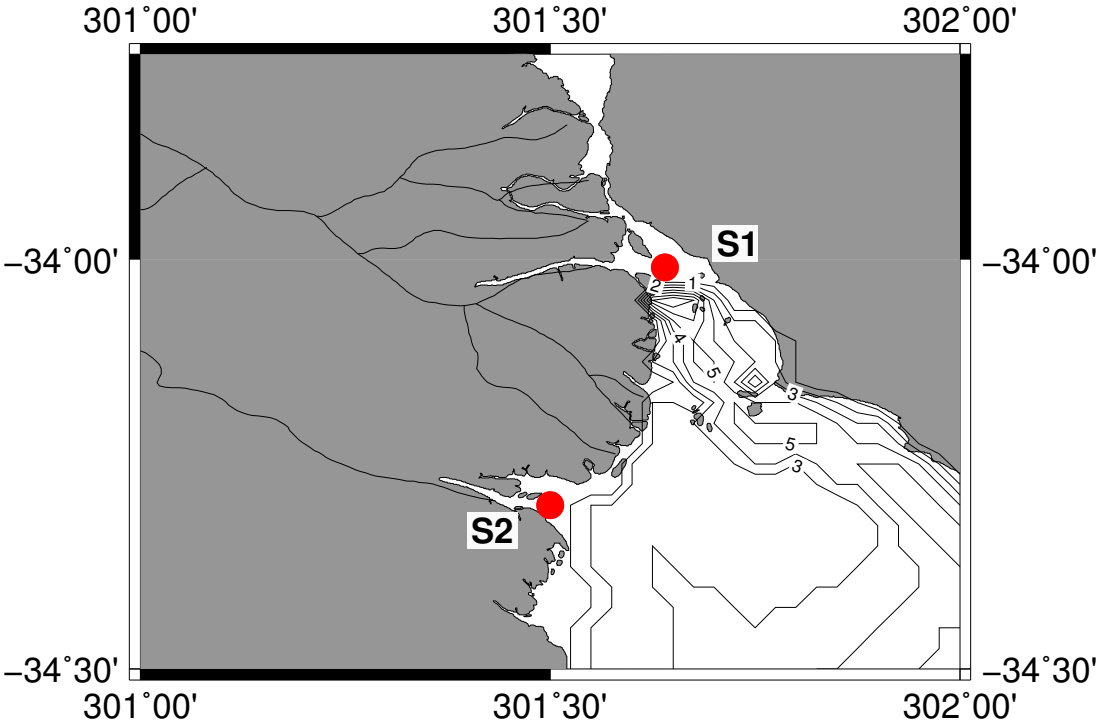

Figure 6.1: Two implemented outlets S1 (75%) and S2 (25%).

Flocculation The flocculation approch described in Chapter 5.3.6 includes only the computation of the floc parameter which indicates a floc growth or floc breakup. The computation of the settling velocities based on the SPM concentration is not implemented. The settling velocities are set constant with:
$u_{sink4} = 0.0002$ (m/s)
$u_{sink5} = 0.00004$ (m/s)
$u_{sink6} = 0.002$ (m/s).
These values double the settling velocities of the fraction of which they are converted.

Río de la Plata parameters The parameters of Table 6.1 are based on investigations in the North Sea. For the RdP no proven data could be acquired. Rough estimations of critical shear velocities and settling velocities by Menendez (2001) were found. These parameters are used to change the setup and listed in Table 6.2. The results of this simulation are presented the following chapter.

Table 6.2: Changed parameters for SPM simulation in the Río de la Plata setup.

Parameter	Value	Unit	Description
d_{50}	0.00015	m	median grain diameter
ν	0.0000012	m^2/s	kinematic viscosity
u^*_{res}	0.01	m/s	criticial shear velocity for resuspension
u^*_{ero}	0.028	m/s	criticial shear velocity for erosion
u^*_{sed}	0.008	m/s	criticial shear velocity for deposition
u_{sink1}	0.0001	m/s	settling velocity fraction 1
u_{sink2}	0.00002	m/s	settling velocity fraction 2
u_{sink3}	0.001	m/s	settling velocity fraction 3
u_{sink4}	0.0004	m/s	settling velocity fraction 4
u_{sink5}	0.00004	m/s	settling velocity fraction 5
u_{sink6}	0.004	m/s	settling velocity fraction 6
A_f	20*24*60*60		constant for flocculation

Chapter 7

Model results

This chapter presents the results of the SPM simulations and the evidence that the hydro-dynamic and wave simulations were successfull and delivered trustful input data to the SPM model. The case studies mentioned in Chapter 6 illustrate the attempts to improve the results of the SPM simulations. Statistical analysis has been performed. The statistical expressions for the analysis are explained in Appendix 8.

7.1 Hydrodynamic model results of the hindcast of February 1999

The results of numerical simulations with the HamSOM are presented. Figures 7.1 and 7.2 show the results of the simulations in comparison with the measurements followed by a statistical evaluation.

The measured water level variations at 'Oyarvide' and 'San Clemente' have been compared with the water level variations computed by the model. Also the current velocities measured at the buoy 'Oceanor' have been compared with the current velocities derived from the model. The table 7.1 shows the statistical analysis between the buoy and the model.

The analysis shows that the water level variation gauged at Oyarvide is overestimated by the model, whereas the model underestimates at station San Clemente. However, both have very low biases (less than 10 cm). The RMS error is slightly higher at Oyarvide with 29 cm compared to 24 cm at San Clemente.

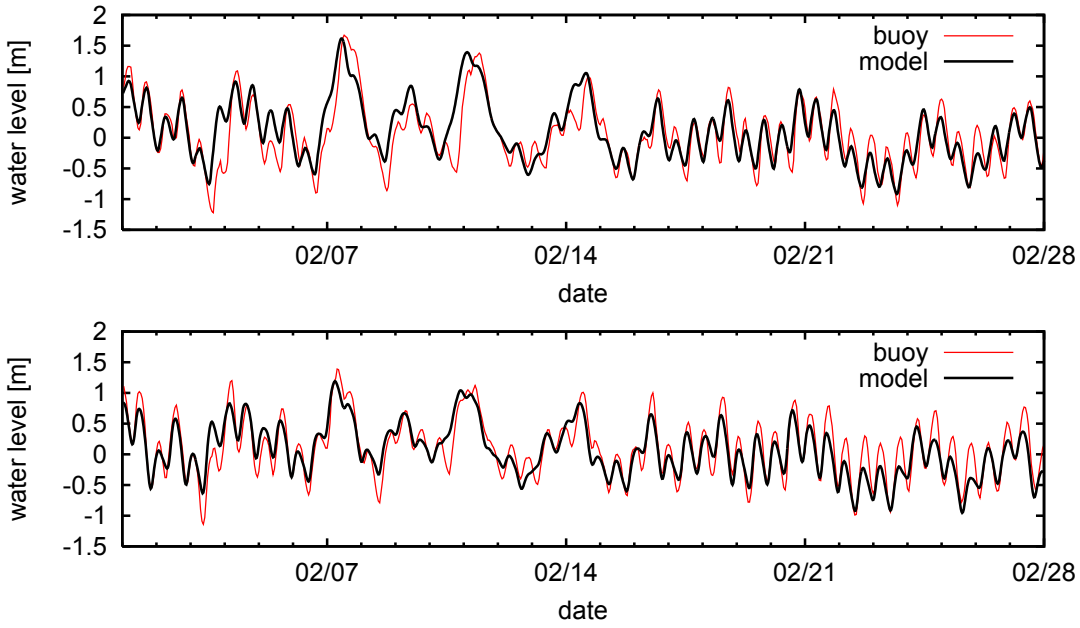

Figure 7.1: Comparison of the water level variation at Oyarvide (upper panel) and San Clemente (lower panel).

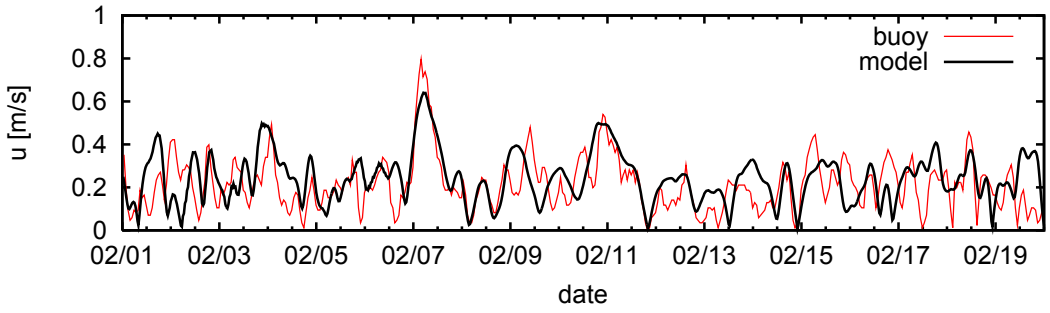

Figure 7.2: Comparison of current velocity at buoy Oceanor.

The model overestimates the current velocities measured at the buoy 'Oceanor' by 0.04 m/s. The RMS error of the current velocities is only 0.13 m/s. The differences in standard deviation of the buoy and the model is for all cases very low. The standard deviations at the gauge Oyarvide are even equal.

In the context of the entire estuary the currents are oscillating in a direction along the axis of the estuary, mainly from NW to SE. Figure 7.3 shows two situations of a semidiurnal tidal condition 6 hours apart. The semidiurnal lunar constituent (M_2) is the one that explains most of tidal variability in the RdP

Table 7.1: Comparison of buoys (x) to model (y) - Statistical parameters of waterlevels for Oyarvide and San Clemente as well as current velocities for Oceanor.

	n	mean x	σ_x	mean y	σ_y	Bias	RMS	Unit
OYARVIDE	671	0.06	0.51	0.09	0.51	0.04	0.29	m
SAN CLEMENTE	671	0.10	0.46	0.03	0.48	-0.07	0.24	m
OCEANOR	467	0.21	0.12	0.25	0.13	0.04	0.13	m/s

which is in agreement with Simionato *et al.* (2001) and O'Connor (1991).

7.1.1 Discussion

Based on the results of the HamSOM, it can be stated that the hydrodynamic part of this work was performed successfully. Water level variations computed with the model fit in amplitude and in phase. In Figure 7.1 each peak is clearly detected by the model. The current velocities in Figure 7.2 do not always agree well with the model. However, current velocities are mostly in phase and have very low rms errors and bias. The simulated hydrodynamic parameters are reliable and with sufficient accuracy to be utilized in the SPM model.

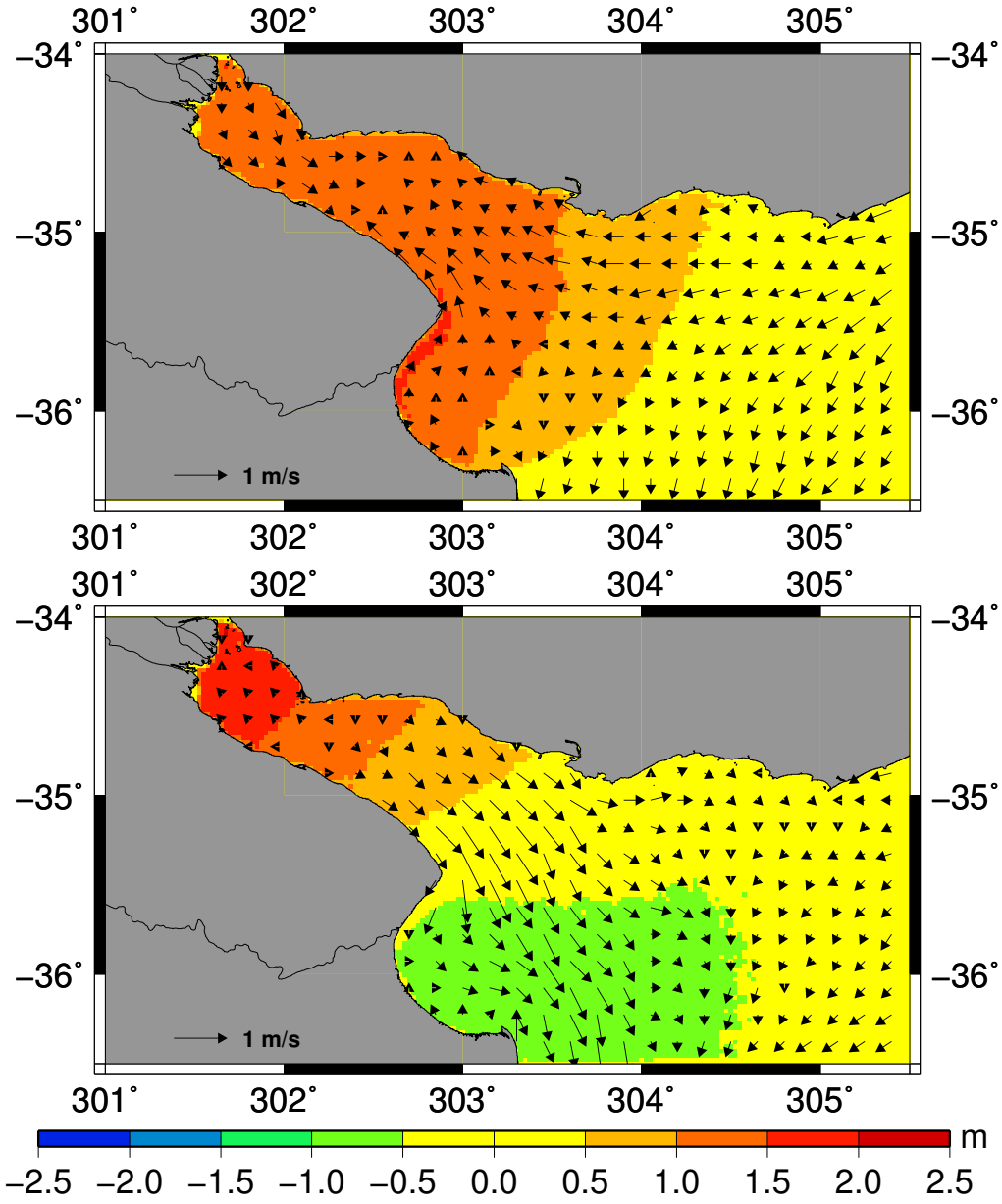

Figure 7.3: Current fields and water levels in one tidal cycle 6 hours apart.

7.2 Wave model results of the hindcast of October and November 1999

In the following section, first the significant wave height computed on grid M of the WAM is compared with the significant wave height of the altimeter tracks near the shelf close to the RdP (see Figure 4.14 in Chapter 4.7). Second, the integrated parameters H_S and $TM1$ period of the F grid run of K-Model and WAM are compared with the corresponding wave parameters measured by the wave rider buoy (see Figure 4.14 in Chapter 4.7).

7.2.1 Comparison of WAM vs. altimeter

The statistical validation of model results against remote sensing data allows a qualitative assessment of the model. To analyze the quality of boundary spectra for the F grid run, wave heights near grid F boundaries generated by WAM in grid M have been compared with satellite data of TOPEX/Poseidon. Along the tracks, the closest grid points of the model were identified. For each of the identified grid points, only the nearest track point was selected and included to compare the data set. The comparison is based on 35 to 60 values depending on the track length. In track 1, 3, 5 and 7 the model underestimates the significant wave height (see Figure 7.4). These are the tracks that head from SW to NE. In track 2 and 4, there is good agreement between the model and the altimeter over large parts of the track. In track 6 the model overestimates the significant wave height. Table 7.3 lists the results of the statistical analysis. The overall bias is -0.12 m. In track 4 on October 29th and track 6 on November 1st (the storm period), the WAM overestimates the altimeter up to 0.38 m. Tracks 5, 6 and 7 show the highest RMS errors of about 0.45 m. Scatter indices are found to be around 20% except on track 7 where this value reaches 32%. The internal variabilities, σ_x of the altimeter and σ_y of the model, differ in ranges from 0.05 to 0.1 m.

Discussion

The comparison of the model results with the altimeter measurements proves a satisfying quality of simulation. The tracks 2, 3 and 4 are best performed by the

Table 7.2: Situation at track dates.

Track	Date	Wind
1	1999/10/21 13:00	4 m/s E
2	1999/10/22 04:00	4 m/s SE
3	1999/10/28 12:00	5 m/s SE
4	1999/10/29 02:30	10 m/s SSE
5	1999/10/31 11:00	10 m/s E
6	1999/11/01 02:00	14 m/s E
7	1999/11/07 10:00	7 m/s NW

Table 7.3: Comparison of Altimeter (x) and WAM (y) - Statistical parameters of significant wave height.

Track	n	mean x (m)	σ_x (m)	mean y (m)	σ_y (m)	Bias(m)	RMS (m)	SI
1	35	1.61	0.10	1.26	0.05	-0.35	0.36	23
2	47	1.26	0.13	1.15	0.05	-0.10	0.18	14
3	63	1.84	0.21	1.70	0.06	-0.14	0.24	13
4	65	1.96	0.66	2.08	0.53	0.12	0.25	13
5	35	2.27	0.11	1.83	0.08	-0.44	0.46	21
6	48	2.16	0.18	2.54	0.27	0.38	0.45	21
7	63	1.44	0.11	1.00	0.01	-0.44	0.45	32
All	356	1.78	0.45	1.66	0.57	-0.12	0.35	20

model. These tracks are at a time when wind conditions are very constant (see Table 7.2). Winds are easterly in moderate scales. The tracks 5 and 6 occured during a time of upcoming wind and slightly turning wind directions. Track 7 is after the storm with turning wind directions and unsteady wind speeds. On track 1, 5 and 7 the model is underestimating the significant wave height. These tracks are orthogonal to the axis of the estuary. On tracks axial with the estuary model and altimeter generally match better.

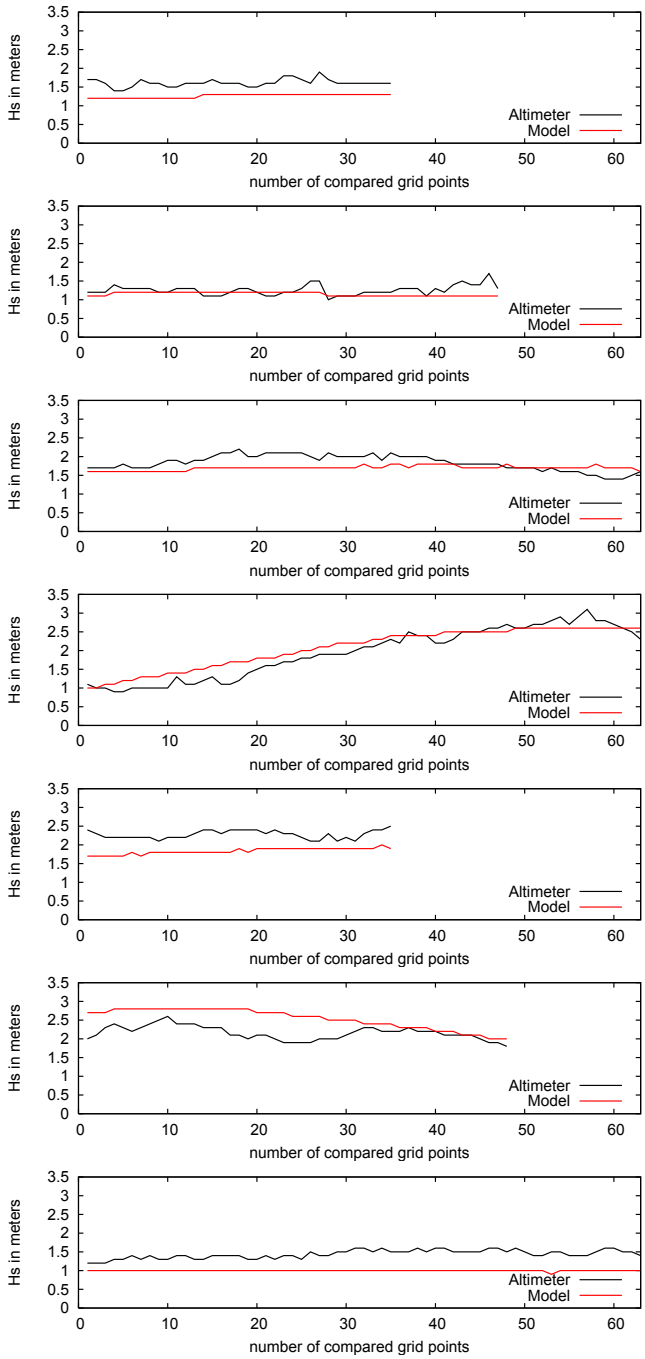

Figure 7.4: Significant Wave Height of altimeter and model in grid M.

7.2.2 Comparison of wave models vs. buoy

A detailed validation study of waves in small enclosed areas has been done by Schneggenburger *et al.* (2000). This study presents the validation of the K-Model in a larger scale. Figure 7.5 presents the time series of both K-Model and WAM in the F grid as well as buoy measurements. H_s and Tm_{01} period are the compared parameters.

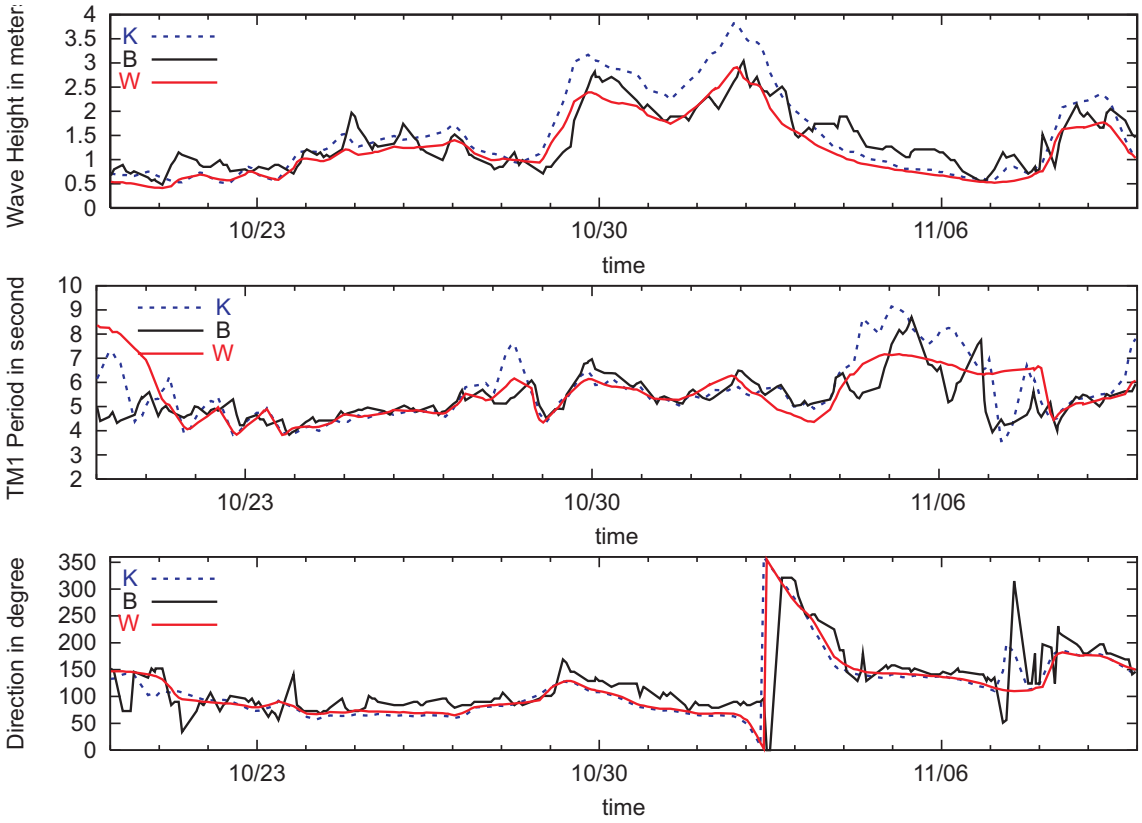

Figure 7.5: H_s, $TM1$ Period and Wave Direction at Buoy - solid black = Buoy, dotted blue = K-Model, solid red = WAM.

Geophysical interpretation The time series of the significant wave height H_s and wave direction go according to the time series of the wind speed and wind direction in Figure 4.5. Both models, WAM and K-Model represent very good the wave conditions in the entrance of the RdP when compared with the buoy measurements. During the first period with steady wind speed and direction

H_s, $TM1$ period and wave direction coincide well in wave height, period and direction. Both models tend to present smoother time series than detected by the buoy. With upcoming winds to speeds of 15 to 20 m/s wave height increases to 3 m of the WAM while the K-Model detects waves up to 4 m. During that period of upcoming winds the $TM1$ period does not increase as the wave height. Only after the storm, when wind speed and wave heights have decreased, the $TM1$ period starts to increase up to 9 seconds when the swell enters the area of interest. Swell are long waves generated during the storm on the South Atlantic Ocean which needed about 3 days to reach the RdP entrance. The wave direction from November 4ht to 7th is SSE although winds are calm and turning.

Significant Wave Height The K-Model's standard deviation of 0.78 m is 0.15 m higher than the WAMs internal variablity of 0.63 m (see section 7.4). A significant difference is obvious for the bias. The K-Model is overestimating the buoy by 0.12 m while the WAM is underestimating the measurement by 0.17 m. The RMS error is slightly higher for the K-Model. The same is true for the scatter indices (SI).

TM1 period Both models show an RMS error in the order of nearly 1 second. Scatter indices are almost identical. The difference of the bias is not as big as it was found for the significant wave height. Both models overestimate the $TM1$ periods when compared to measurements, WAM by 0.17 seconds and K-Model by 0.28 seconds.

Table 7.4: Comparison buoy (x) and model (y) - Statistical parameters of significant wave height and $TM1$ period.

		n	mean x	σ_x	mean y	σ_y	Bias(m)	RMS (m)	SI
HS	K-Model	204	1.41	0.61	1.53	0.78	0.12	0.45	31
HS	WAM	204	1.41	0.61	1.24	0.63	-0.17	0.33	20
		n	mean x	σ_x	mean y	σ_y	Bias(s)	RMS (s)	SI
TM1	K-Model	204	5.35	0.87	5.63	1.25	0.28	0.96	17
TM1	WAM	204	5.35	0.87	5.52	1.02	0.17	0.98	18

Discussion

The results of the validation statistics are of an acceptable quality and do not differ significantly from other shallow water applications with the K-Model (Schneggenburger, 1998) or SWAN (Ris *et al.*, 1999). Generally it can be said that the WAM obtained slightly better results. This counts mainly for the strong wind period between October 29th and November 3rd. Here the K-Model overestimates and the WAM underestimates the peaks. Nevertheless, the validation with the available measurements can be regarded as successful for WAM and K-Model. Although $TM1$ periods simulated with the WAM show a higher RMS error, it is underestimating less the measurements than the K-Model. Especially long swell periods are depicted by the WAM. In such cases the K-Model overestimates the measurements. Due to the fact that the buoy is situated at 18 m water depth, WAM is still in depth ranges according to its strength. In shallower waters the quality of WAMs results is uncertain. In conclusion it can be stated that both models simulate the wave conditions with acceptable accuracy and the K-Model is applicable for generating waves to drive the SPM model.

7.3 SPM model results of the hindcast July - December 1999

This section first explains how the model is working corresponding to the hydrodynamics and waves. Secondly, the case studies described in Chapter 6 are applied and the results are discussed. In order to limit the number of pictures only the image of November 21st is selected for demonstration.

7.3.1 Model results with North Sea setup

The RdP is a wave dominated estuary and consequently, waves have enormous impact on sedimentation processes in the middle and the outer RdP. A rather simple method to determine the occuring bottom processes is to average the shear velocities on the bottom. The shear velocity counts for both waves and currents. The mean of the bottom shear velocity based on six month calculations is visualized in Figure 7.6. The four colors correspond to the occuring processes explained in the description of the model physics in section 5.2. The red color represents zones where mainly deposition occurs. The yellow color represents equilibrium, the green zones areas of resuspension and the blue zones areas of erosion. A disregard of waves in the lower panel of Figure 7.6 would leave large parts of the estuary under depositional conditions, while the introduction of waves brings a mean equilibrium state on large portions of the area. Without considering waves, the shear velocity would be much less, sedimentation would take place and a sediment filling of the estuary would happen shortly without transporting the sediment further offshore. With the current-dependent shear velocity alone, the material would not be transported so far offshore. Consequently, waves play an important role, because they increase the shear velocity which leads to wave induced erosion and it keeps the sediment in suspension even after strong wind events due to swell which is generated on the South Atlantic Ocean and enters the estuary. Therefore it is strongly recommended to consider waves for SPM transport and all of the following results include waves action.

A different manner to show the effect of waves is by comparing the time series of the shear velocities on the bottom. Figure 7.6 shows two sites marked as a black stars: No. 1 and No. 2 at which the shear velocities are computed and vi-

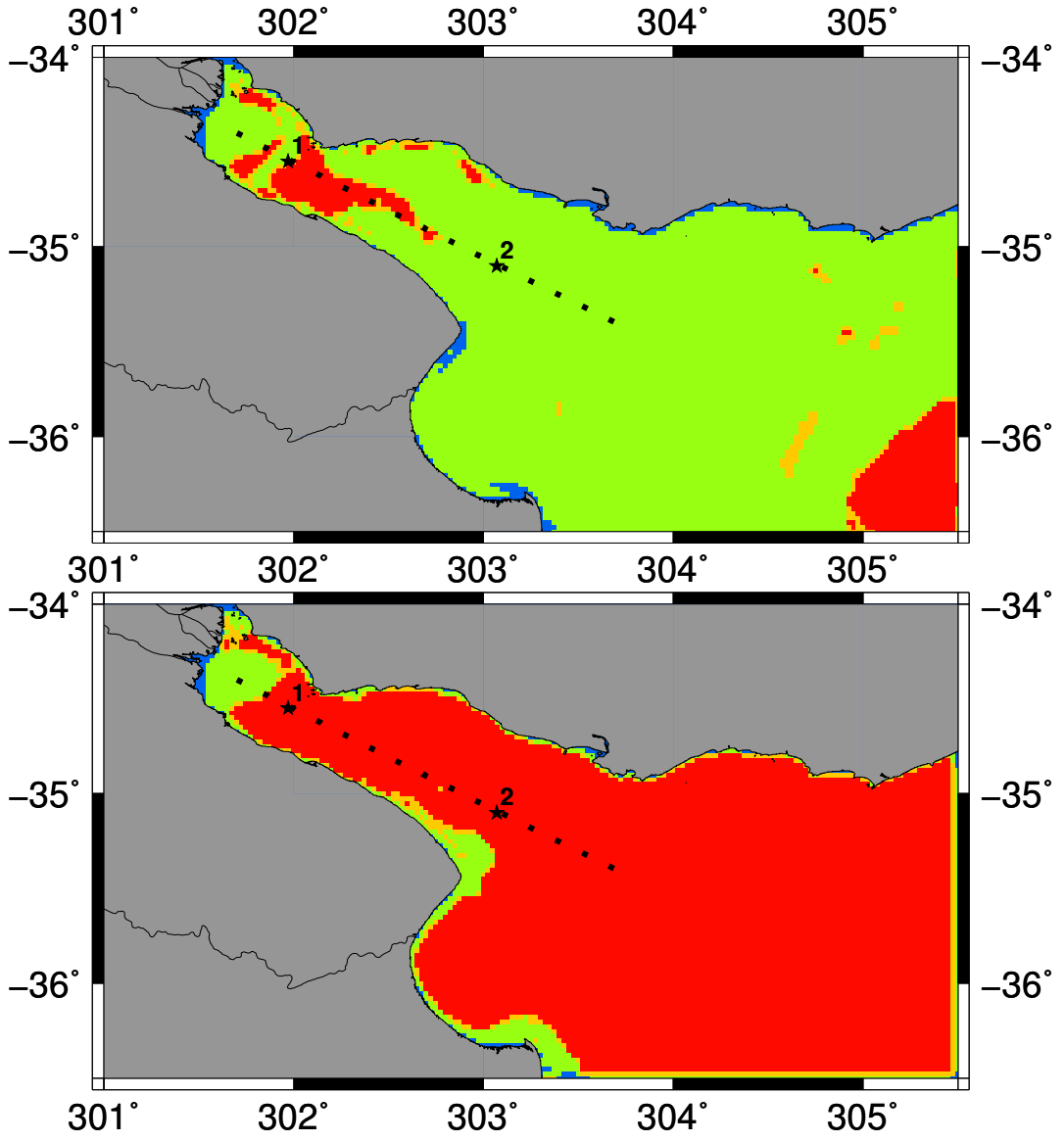

Figure 7.6: Zones of erosion (blue), deposition (red), resuspension (green) and equilibrium (yellow), the upper panel includes the effect of waves and lower panel disregards the effect of waves.

sualized in Figure 7.7. Figure 7.7 is focused on the period between October 20th to November 21th. Two horizontal lines indicate the thresholds for erosion and deposition. With the consideration of waves at two dates during the simulation period erosion occured. These peaks are marked by the area above the line for erosion (green). The shear velocities at the outer point are higher than at the

inner point due to the wave action which is partly dissipated before it reaches the inner site No. 1. The area below the line for deposition (red) describes the occurance of deposition, whereas between the two lines the area marks the occurance of resuspension. There is a fairly balanced ratio of resuspension to deposition over time. In comparison, without waves the shear velocity never reaches the critical value for erosion and hardly exceeds the critical value for resuspension. It is mostly in ranges where deposition occurs.

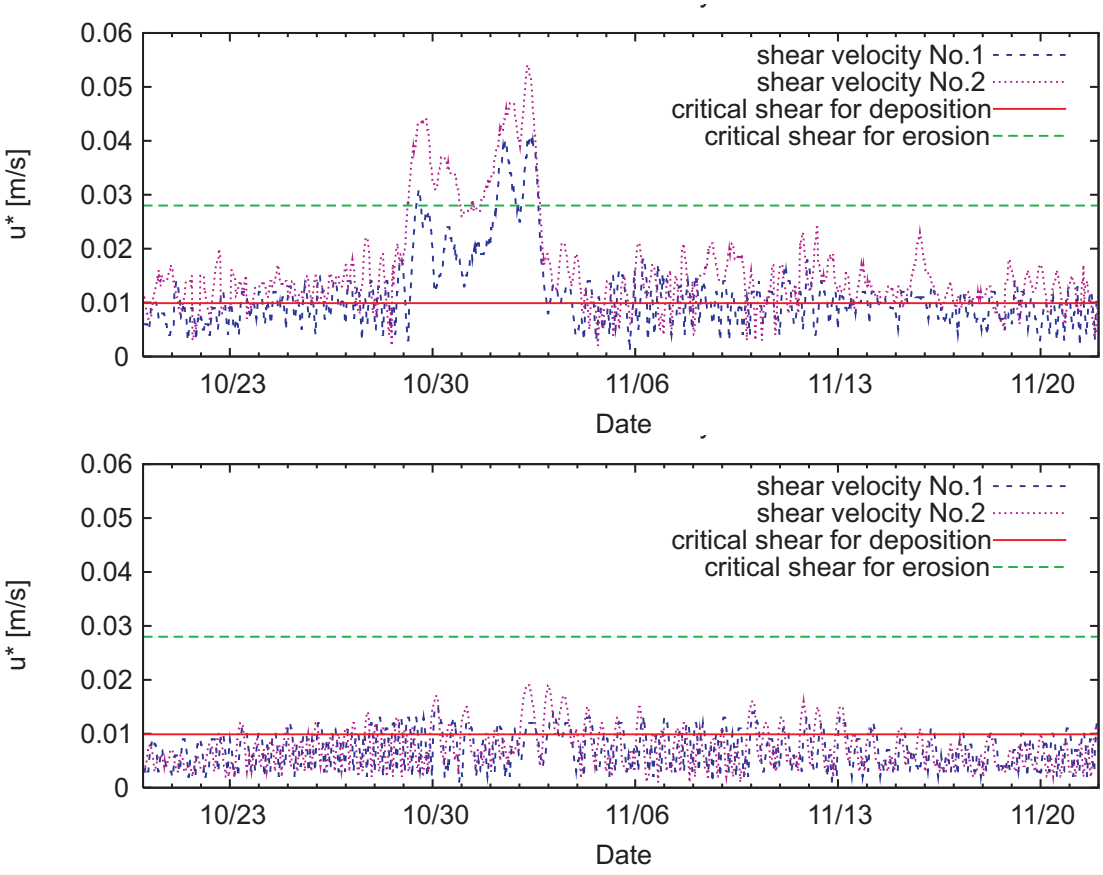

Figure 7.7: Time series of the shear velocities on the bottom at site No. 1 (blue) and No. 2 (pink) - upper panel with waves, lower panel without waves.

To explain the occuring processess in the water column the time series of Figure 7.8 shows the sum of the SPM concentration of the three fractions for three different water layers. The upper panel represents the time series at site No. 1 and the lower panel at site No. 2. As could be expected, the SPM concentration is highest in the lowermost water layer and decreases towards the surface. A fully mixed water column occurs at site No. 1 only during the storm. At site No. 2, which is disposed to wave action at any time, the mixing occurs more often. At the time when the storm abates around November 4th, strong and quick capsizes in the currents occur due to tides at site No. 1, so that SPM in the lower water layer settles and is resuspended immediately. This period from November 4th to November 8th corresponds to the period of the incoming swell which is identified in the wave periods in Figure 7.5. At site No. 2 on November 4th, a rapid decrease of concentrations down to less than 20 mg/l in all layers is observed. This effect is due to the moving front over site 2 towards NW. Wind, current and swell in the same direction intensify this behavior.

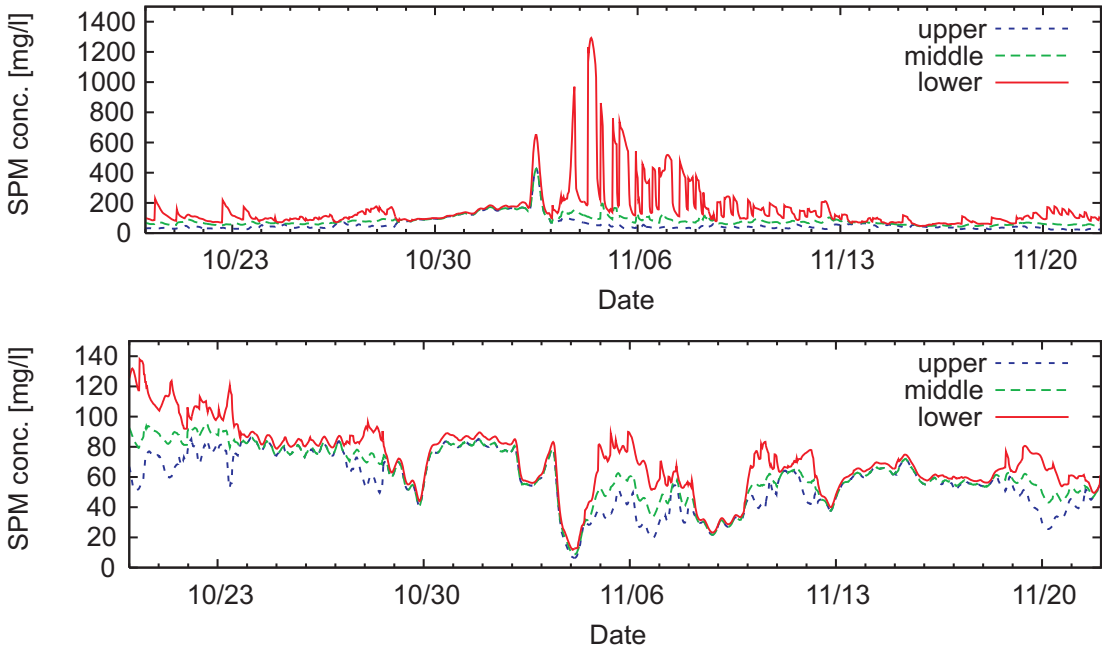

Figure 7.8: Time series of SPM concentration in three water layers at site No.1 (upper panel) and No.2 (lower panel).

Time series demonstrate the changes of the SPM mass on the bottom in Figure 7.9. Only bottom layer $z1$ and $z2$ are chosen, because there the changes are more significant. It is visible that at the beginning of the storm the SPM in the uppermost $z1$ and the underlaying layer $z2$ is removed. After the event, SPM is deposited and resuspended again in the uppermost layer depending on the tidal cycle. The peaks right after the storm are significantly high because the tidal signal is intensified by the swell which is running into the estuary. The peaks get less high as soon as the stable condition in the RdP is reached again. The SPM mass in the second layer increases constantly with passing time.

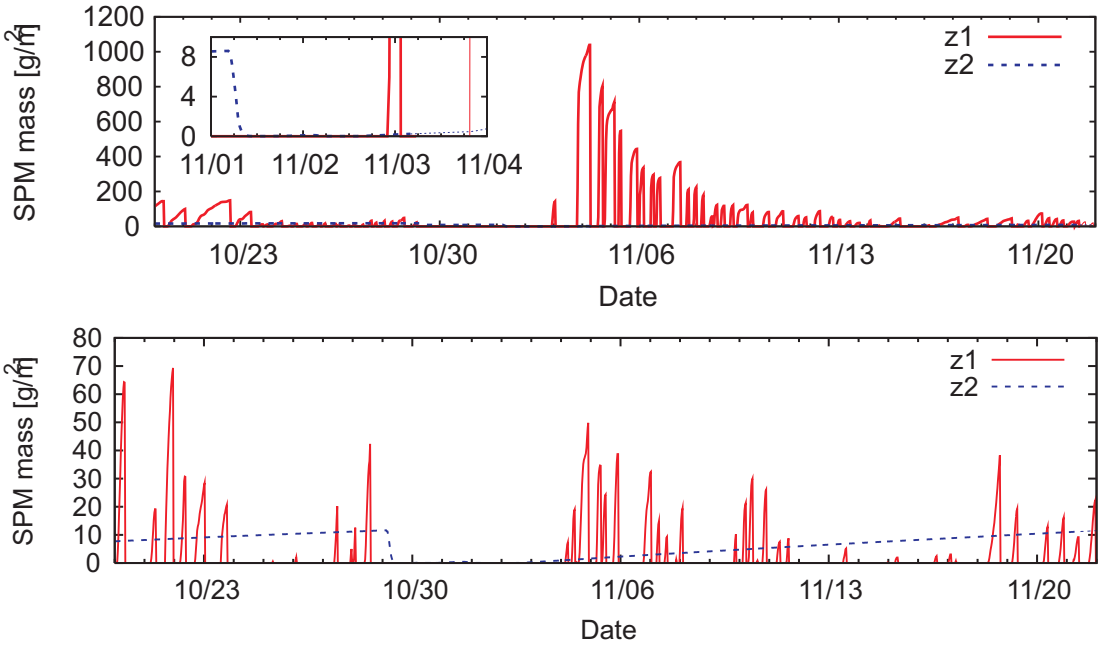

Figure 7.9: Time series of SPM mass in bottom layers $z1$ and $z2$ at site No.1 (upper panel) and No.2 (lower panel).

7.3.2 Model results compared with satellite measurements

The computed results in Figure 7.10 show the spatial distribution of surface SPM concentration and front extension. The currents are visualized by the arrows on the map. The blue spot in the center of the tidal river with low sediment concentration resulting from model experiments can be explained with the currents. There, the outflow of the river and the incoming tidal current meet and the veloc-

ity diminishes (see Figure 7.11). The SPM can settle down and the concentration decreases in the surface water layer. The shape of the front is well reproduced by the model. The shape of the front agrees well to the results of Framinan & Brown (1996) who investigated the spatial and temporal distribution of the turbidity front. The location of the front with the turbidity maximum is also clearly visible in Figure 7.12.

Figure 7.12 demonstrates the surface SPM concentrations along a transect through the RdP. The position of the transect can be viewed in Figure 7.6. The transect starts at Playa Honda near the delta and cuts the RdP passing Barra del Indio eastward to -56.3°W. Both, model and satellite show low SPM concentrations in the westerly quarter of the transect. Continuing to SE the SPM concentration starts to increase for both. The maximum is reached near Barra del Indio and is much lower for the model than for the satellite. The satellite shows clear peaks of SPM concentration up to 250 mg/l, while the model does not exceed 100 mg/l.

A direct comparison of the model and the satellite gives the scatter plot in Figure 7.13. Below 10 mg/l the model computes higher concentrations than the satellite. Between 20 and 80 mg/l the model and the satellite have the best agreement, while the model computes less concentration than the satellite in the higher concentration ranges above 100 mg/l. A similar pattern of the scatter plot is observed for all of the considered images in Figure 4.16.

7.3.3 Detection of zones of erosion and deposition

Regarding the sediment mass on the bottom layers, the zones of sedimentation and erosion were identified. A similar approach was made already in the beginning of the chapter using the shear velocity as indicator. The map in Figure 7.14 displays the mean sediment mass on the bottom taken during 6 months. It includes the sediment mass of the 3 upper bottom layers. The positive values represent gain and the negative values, loss of sediment. The sediment mass is given here in g/m^2. The area of sediment gain is the area where mostly current velocities diminish when the tidal current meets the river outflow. There the SPM can settle and be resuspended depending on the tidal conditions. The zones of erosion are basically located where the wave energy dissipates. Barra del Indio is such a region and also the turbidity maximum is located there.

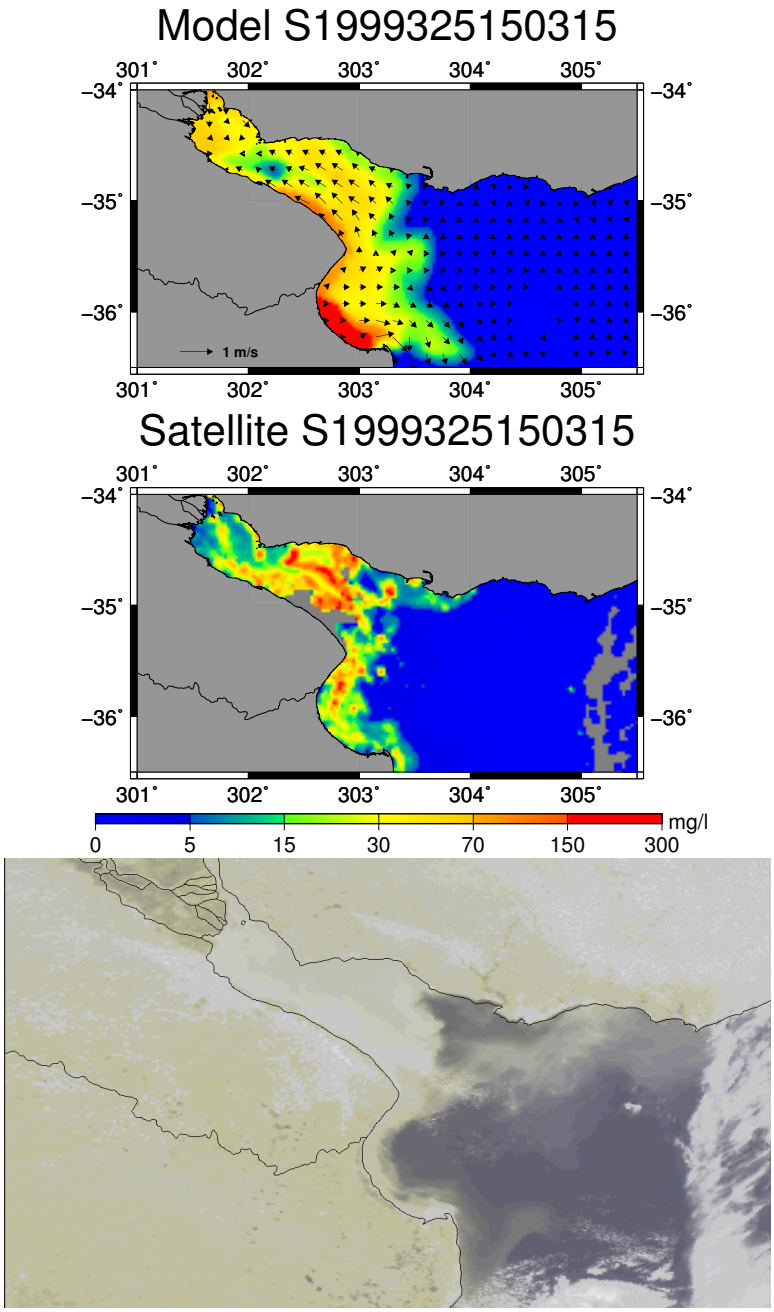

Figure 7.10: Spatial distribution of surface SPM on November 21st - Model, Satellite and Photography.

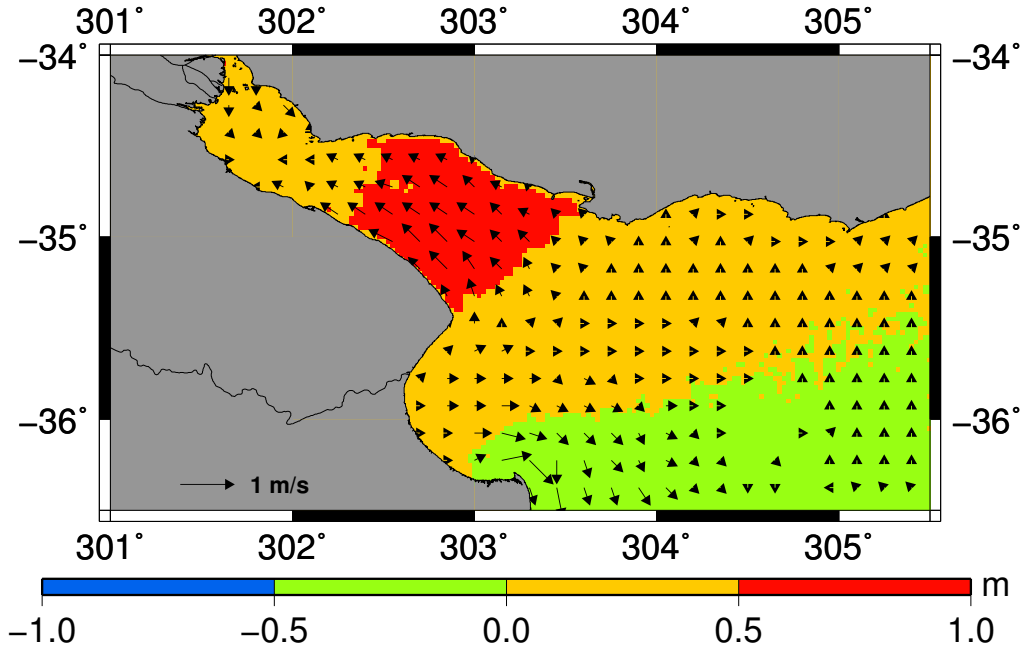

Figure 7.11: Current field and water levels on November 21st.

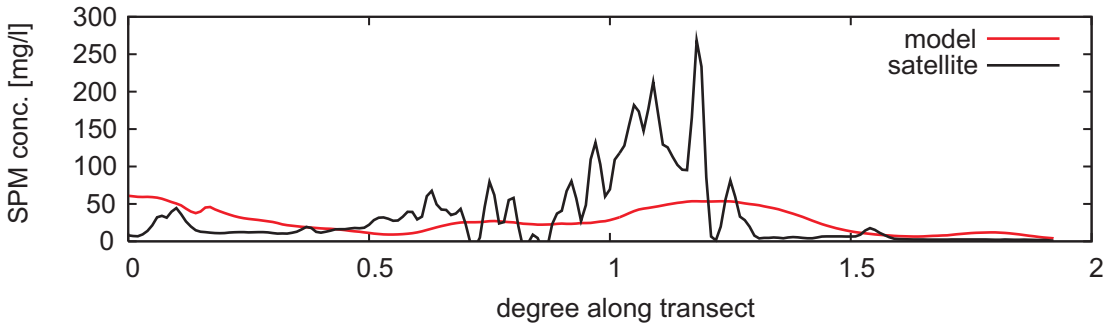

Figure 7.12: SPM concentrations along the transect of the estuary on November 21st.

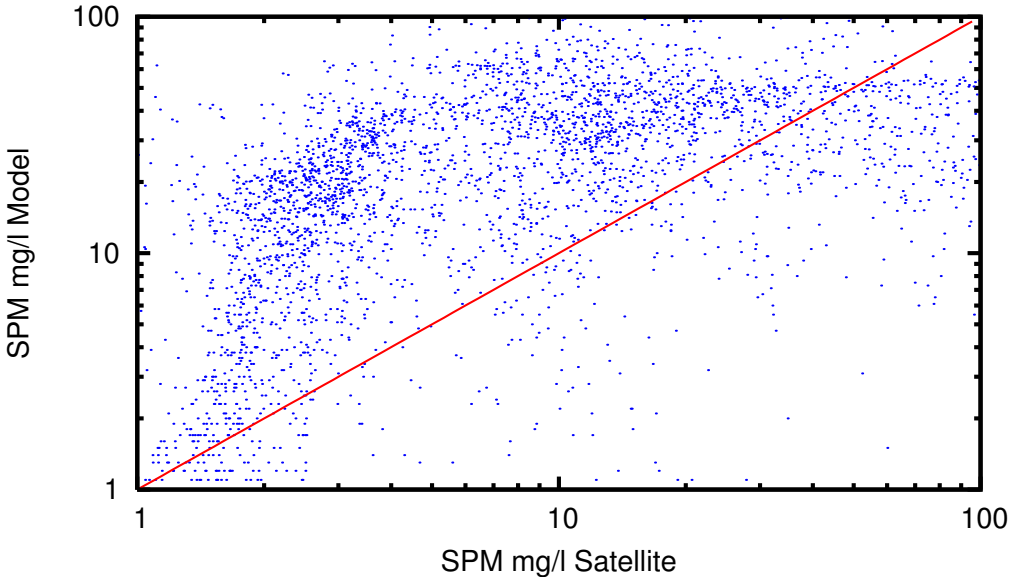

Figure 7.13: ScatterPlot of surface SPM on November 21st - model against satellite.

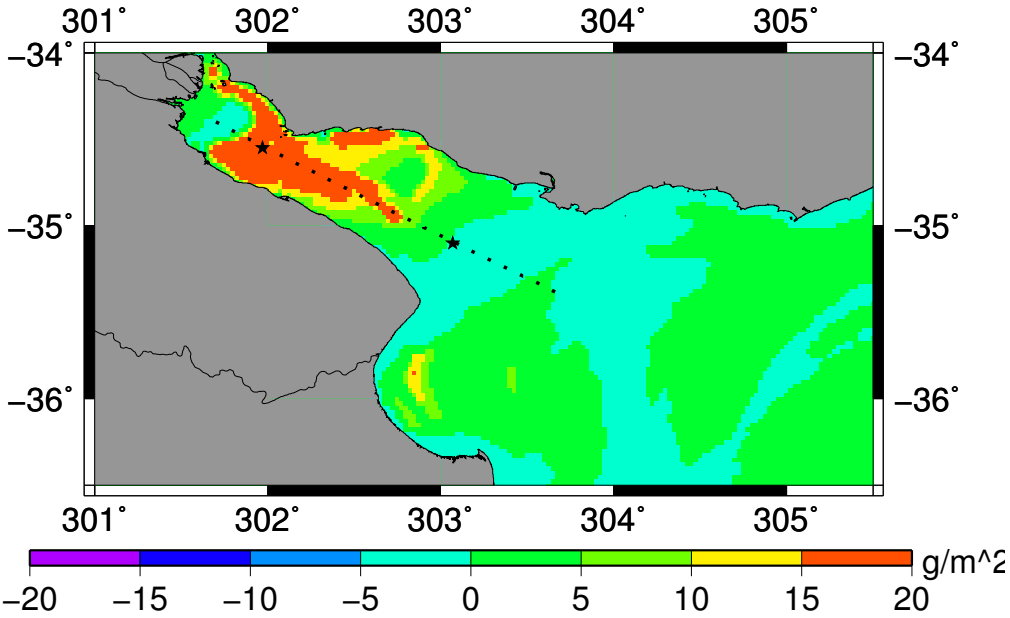

Figure 7.14: Zones of erosion (negative on scale) and deposition (positive on scale) due to sediment gain and loss in the bottom layers.

7.3.4 The case studies

The foregoing case serves as reference case for the subsequent analysis. This reference case was computed with a ratio of '170 mg/l SPM concentration per 15,000 m^3/s discharge', a single outlet of discharge and SPM input. It will be analysed to determine what effect a change in this ratio will have on the sediment conditions in the RdP. It will also be discussed what effect a second discharge outlet has. Flocculation effects will be discussed in addition.

Analysis with higher and lower sediment concentration input

Less sediment concentration at the outlet has no effect on the front shape. The front has a similar extension. Generally, there is less sediment concentration in the entire RdP, even in the central region of Canal Intermedio the sediment concentration decreases to sediment concentrations below 5 mg/l at the surface. On the contrary, an increase of sediment concentration at the river outlet leads to generally higher surface concentrations in the entire RdP. In any case, the Bay of Samborombon in the southern opening of the RdP (see Figures 7.15 and 7.16) seems to be a sediment trap. After 6 months of simulation there is a continuous increase of sediment concentration in the bay.

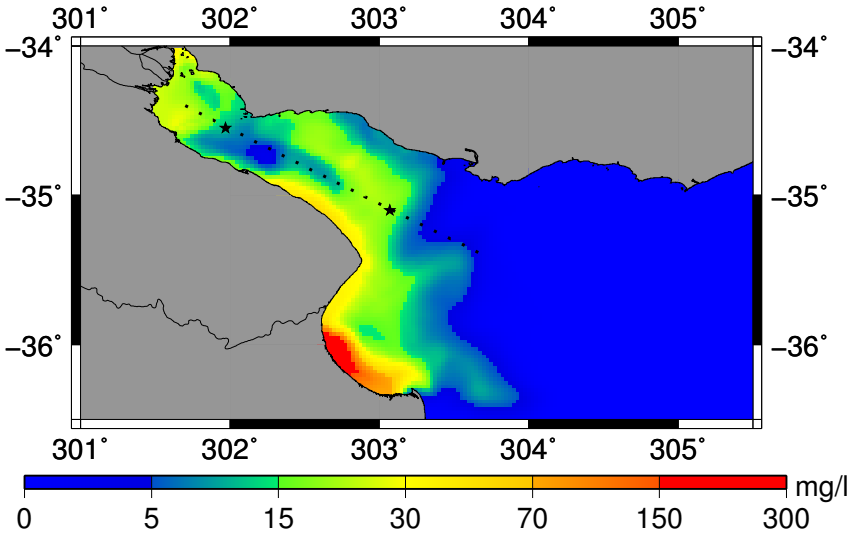

Figure 7.15: Spatial distribution of surface SPM on November 21st with lower sediment input.

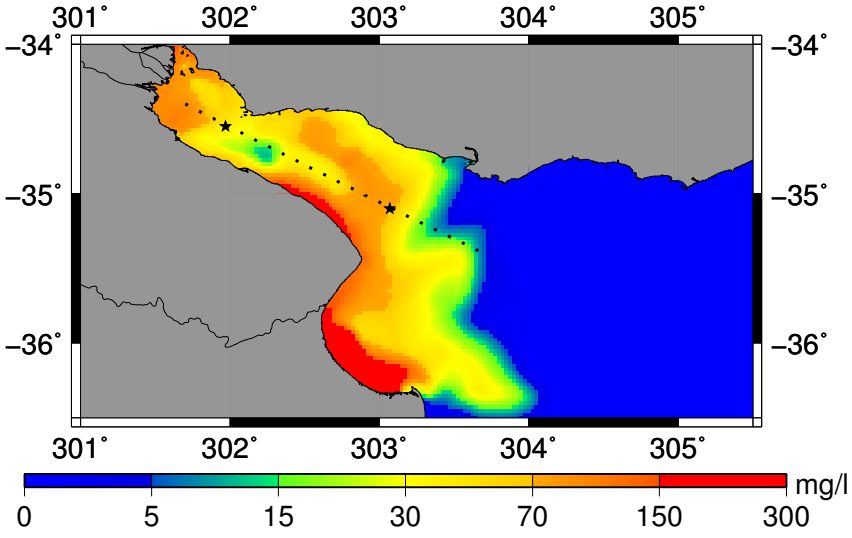

Figure 7.16: Spatial distribution of surface SPM on November 21st with higher sediment input.

Analysis of flocculation effects

The introduction of flocculation brought significant changes in the spatial distribution of SPM in the surface layer. Figure 7.17 shows the difference between the model result with and without flocs. The red areas mark the areas where the flocculation approach computes lower SPM concentrations and the blue areas mark the areas where the model with flocculation produces higher concentrations. The Bay of Samborombon shows in large parts a strong increase of SPM concentrations and only a single spot in this bay shows a decrease of SPM concentration. The most interesting change is the increase of SPM concentration along the front at Barra del Indio. The same feature can be recognized on the transect in Figure 7.18.

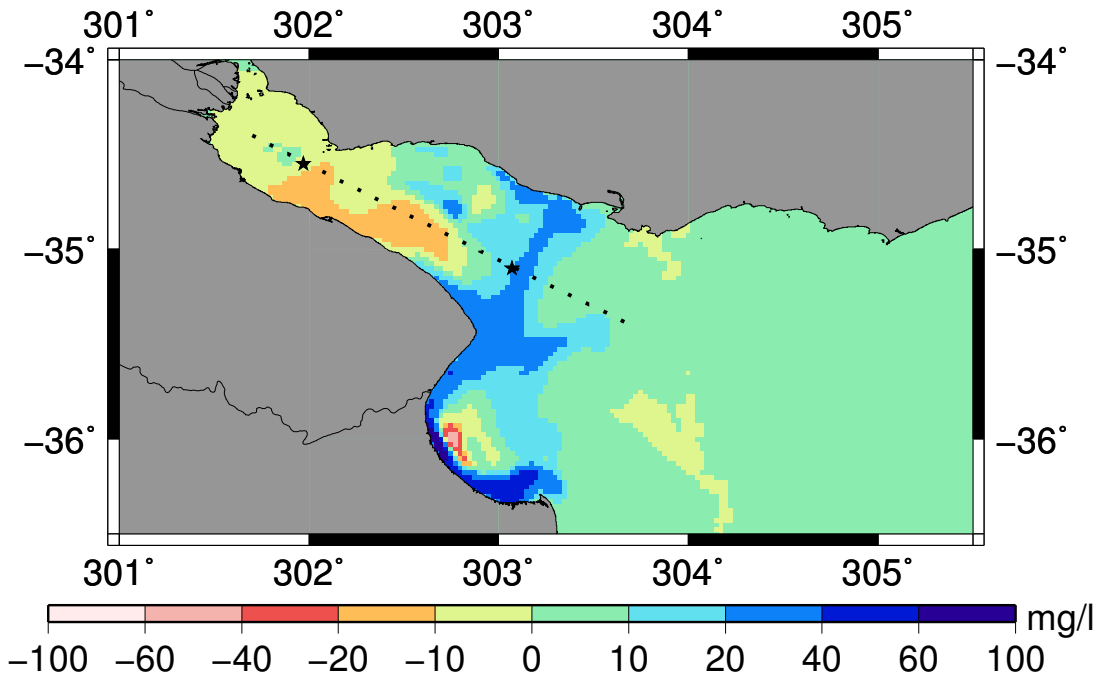

Figure 7.17: Comparison SPM concentrations in mg/l of model with and model without flocculation - positive values indicate higher concentrations with flocculation.

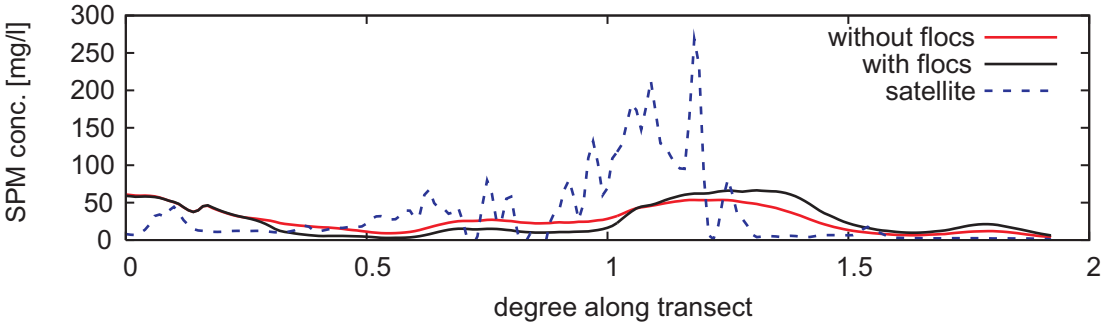

Figure 7.18: SPM concentrations along the transect of the estuary.

Figures 7.19 and 7.20 demonstrate the SPM concentrations in the water layers at site No. 1 and site No. 2. Each of the figures is split into three panels. The upper panel shows the sum of the concentrations of all 6 fractions in three water layers, the middle panel shows only the sum of fractions 1, 2 and 3 and the lower panel the sum of the concentrations of fractions 4, 5 and 6. This is a way to analyse the quantity of flocculation. In both figures it is visible that flocs make the largest portion of SPM. During the investigations it could be observed that the floc parameter P_F was mostly larger than 1. Only at a few events did the floc parameter decrease below 1 and then the flocs break and the concentrations of the fractions 1, 2 and 3 exceed the concentrations of the flocs in fractions 4, 5 and 6.

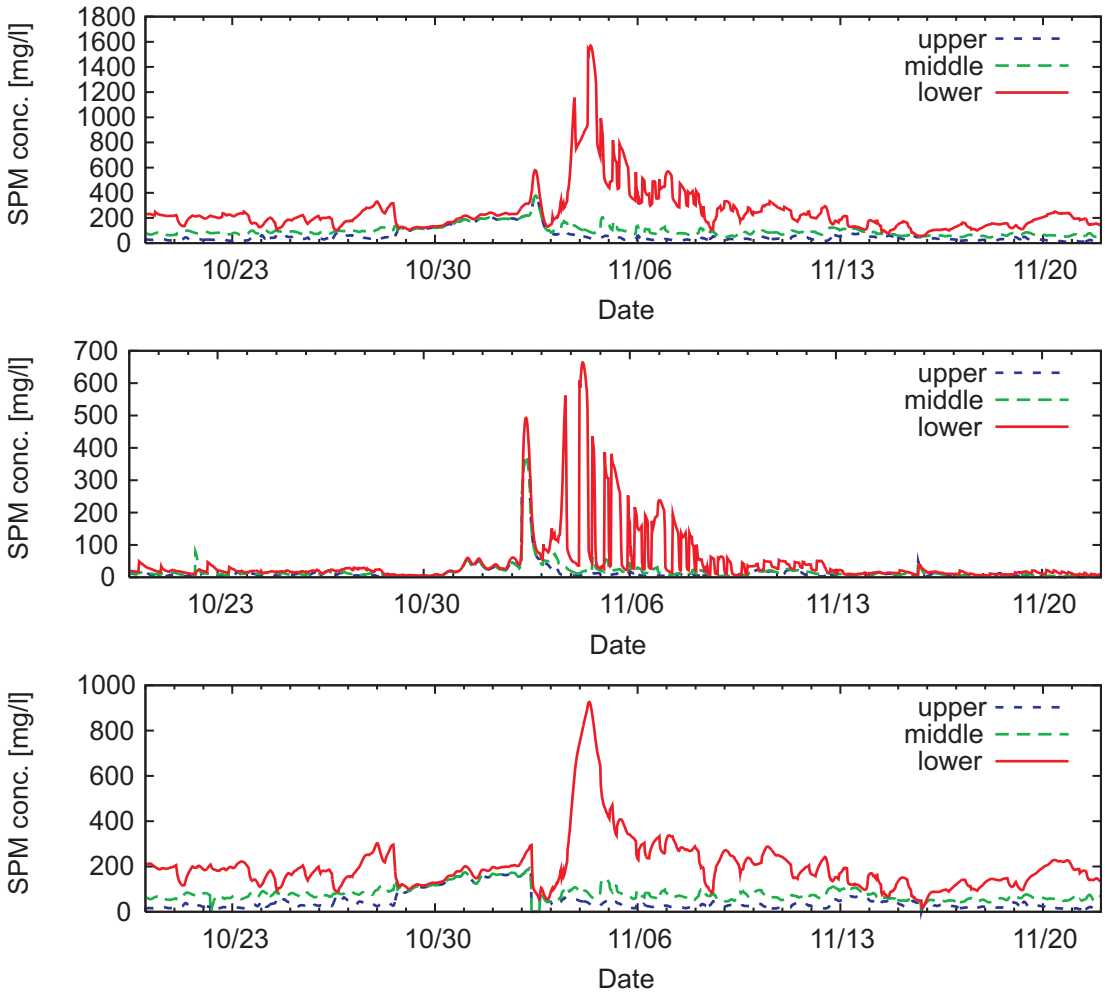

Figure 7.19: SPM concentrations in the waterlayers at site No. 1 (upper: sum of 6 fractions; middle: sum of fractions 1, 2, 3; lower: sum of fractions 4, 5, 6).

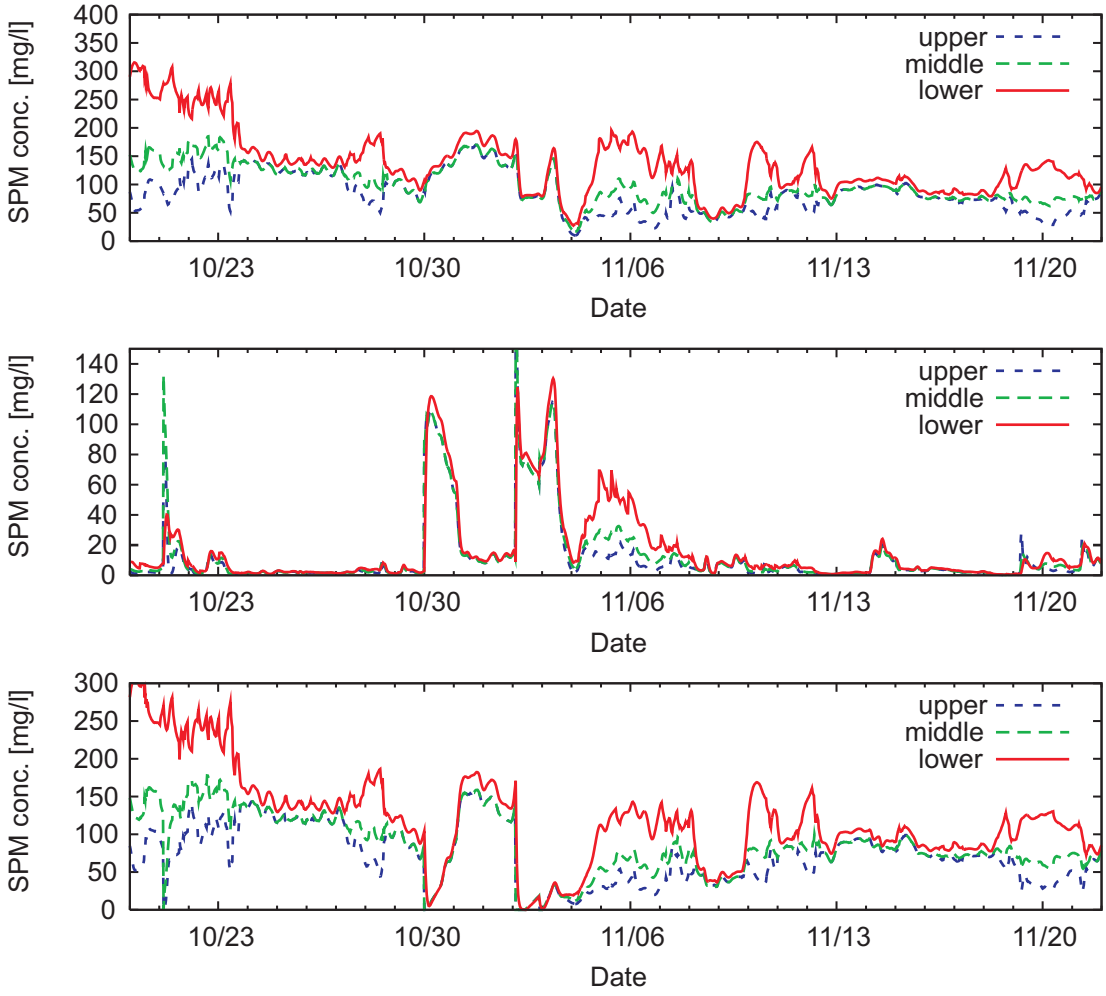

Figure 7.20: SPM concentrations in the waterlayers at site No. 2 (upper: sum of 6 fractions; middle: sum of fractions 1, 2, 3; lower: sum of fractions 4, 5, 6).

Analysis of change in river discharge

A temporal-constant SPM concentration at the discharge outlet has been tested although it is not realistic. Therefore the results are not presented and analyzed here. The discharge-dependent SPM concentration input was used because it is the most realistic approach. On the other hand, in order to obtain an even more probable discharge behavior simulations were performed with a second river outlet where the delta distributaries of the Rio Paraná meet the RdP. This change brought an improvement of the results mainly along the Argentine coastline while in the middle of the estuary hardly any changes are observed. Figure 7.21 shows a direct comparison of the model with a single outlet and the model with two outlets. The effect of a second outlet is that higher concentrations at central Playa Honda and lower concentrations along the Argentine coastline from Playa Honda towards Bay Samborombon are observed. In particular in the bay a strong decrease of SPM surface concentration occured. This might be a solution to avoid a permanent sediment filling in the bay.

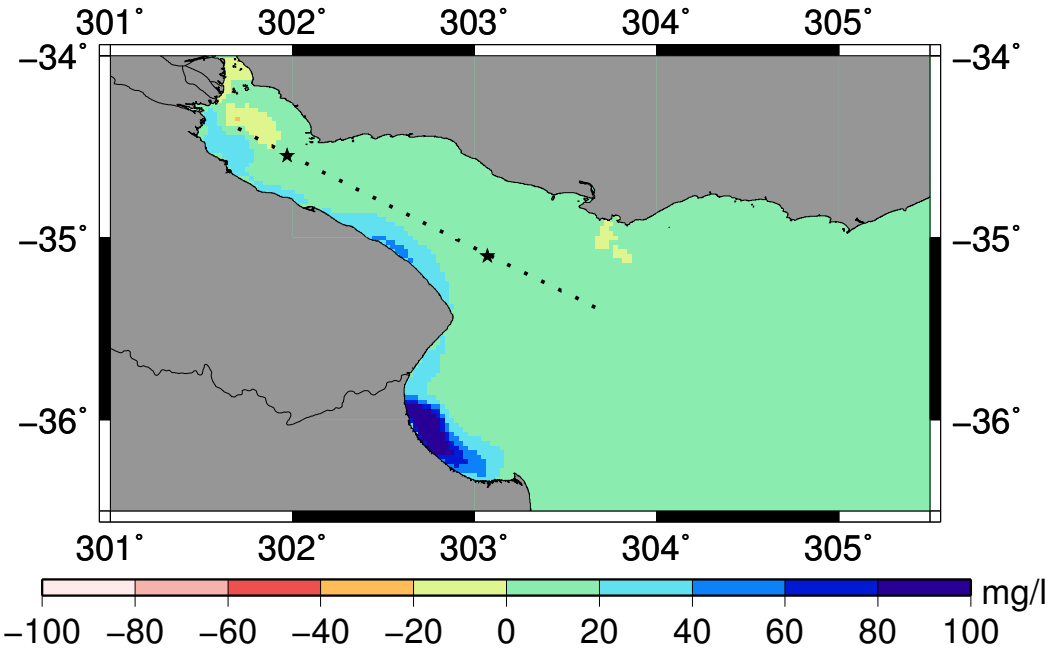

Figure 7.21: Comparison of model with one outlet and model with two outlets on November 21st - positive values indicate lower concentrations with two outlets.

Analysis with parameter setup adapted to the RdP, flocculation and a second outlet

The last analysis shows the effect of changing selected parameters in the configuration as well as the effect of adding flocculation and a second outlet. Rough estimations of Menendez (2001) suggest a critical shear velocity for deposition of 8 mm/s, a d_{50} between 6 and 20 μm and settling velocities up to 0.4 mm/s. Figure 7.22 shows the spatial distributions of SPM on the surface due to the adapted model setup for the RdP. The shape of the front is similar to the one of the default case in Figure 7.10. A direct comparison of both shows the clear difference in the spatial distribution in surface SPM concentration. Compared to the default case the sediment concentration has increased in the Bay of Samborombon and also partly along the front at Barra del Indio. Also at Playa Honda between the two outlets, a zone with higher SPM concentration on the surface has developed. Similar to Figure 7.21, the present case shows a decrease in concentrations along the southern coast of the RdP due to the second outlet. In order to compensate the quick settling of the flocs due to the increased settling velocities, the flocculation constant A_f had to be multiplied by 20 in order to receive a similar surface concentration as in the default case. The concentration would have been very low or zero without that adaption, especially near the front at Barra del Indio. There the material settles more easily due to the higher settling velocities for flocs. Also the critical shear velocity for deposition, which is lower than in the North Sea setup, benefits this behaviour. Figure 7.23 shows that there is more material deposited than in the default case. Even the second bottom layer $z2$ contains more SPM.

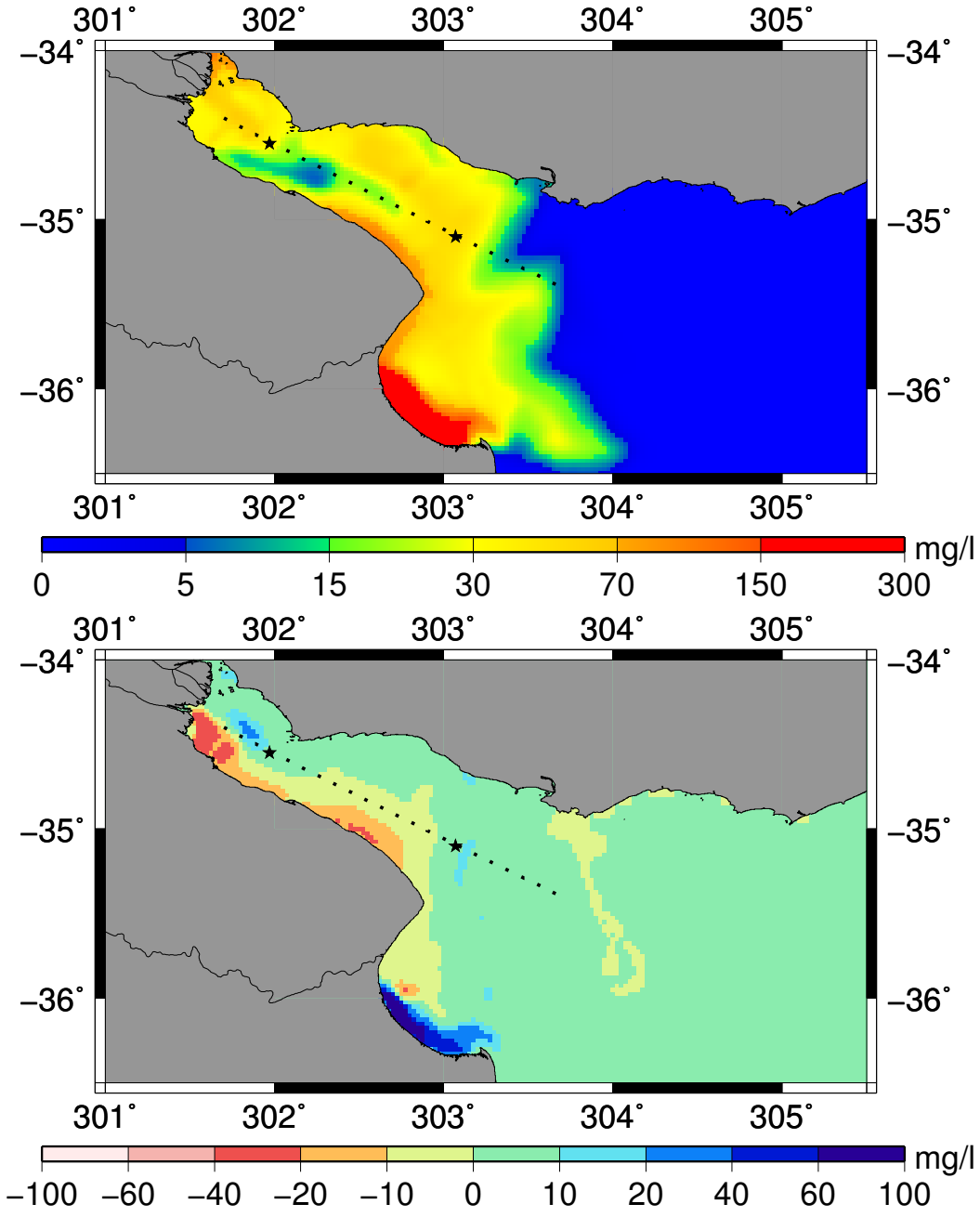

Figure 7.22: Spatial distribution of surface SPM concentration on November 21st with adapted parameters (upper panel) and comparison with the default case where positive values indicate higher concentrations with the adapted setup. (lower panel).

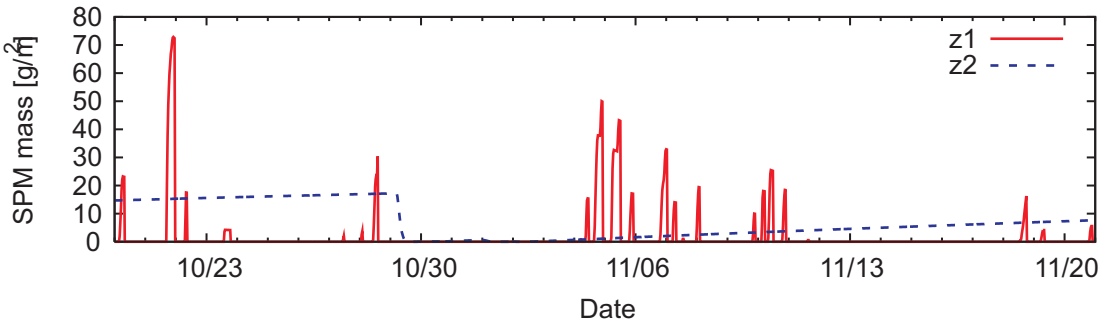

Figure 7.23: SPM mass on the upper two bottom layers at site No. 2.

Chapter 8

Conclusions

The SPM model was applied in order to generate a spatial and temporal distribution of SPM in the water column of the Río de la Plata. The results of the SPM model agree with the generated input data of currents and waves. It was shown that the simulations of waves and currents were performed successfully and provided input data of high quality to the SPM model. However, the input data of discharge and SPM are very poor in the present work, because the acquisition of data for the area of interest was very complicated. Data were limited available or not accessible.

In Chapter 4 it was mentioned that SeaWiFS satellite data were of limited use in the RdP region. The interpretation of SeaWiFS data in water with SPM concentration higher than 80 - 100 mg/l is very difficult, because the reflection of light from the sediments is so bright that they are interpreted as clouds. Therefore, the only source of SPM reference data used in the present work was not even convenient. Nonetheless, the shape and the extension of the SPM plume in the reference images could be recognized well and served for a comparison with the model results. Regarding the shape and the extension of the plume, the model generated good results. The magnitudes of SPM concentrations were not comparable due to the limited interpretation options that SeaWiFS offers at such SPM concentrations.

Besides the SPM reference data, also the SPM input data at the river outlets was insufficient. The approach of setting the SPM input concentration propor-

tional to the discharge appeared to be useful. Measurements of SPM at the outlet or a clear definition of the ratio between discharge and SPM concentration would be necessary to improve the model results.

As described in Chapter 4 the discharge data were acquired for a single outlet. It is known that in particular the Paraná river has a wide spread delta. To approximate a real situation and to improve the model results a second outlet has been introduced. It was shown that a second outlet changed the current patterns resulting in a changed SPM distribution. The Bay of Samborombóm in the southern opening of the RdP appeared to be sediment trap with a single outlet. The introduction of the second river outlet showed that this sediment trap can be avoided by modifying the river discharge. Therefore, the discharge data set must be more detailed and of high resolution in space and time in order to improve the simulation results.

Waves play a major role for the behavior of SPM in the water column. It was shown that the inclusion of waves is essential to reproduce the shape of the plume. Currents alone are not capable of bringing the material into suspension in the middle and outer RdP. Waves are a fundamental force to bring the material into suspension.

The introduction of flocs was an attempt to change the SPM concentration in the water column depending on turbulence. The applied approach brought significant changes in particular near the turbidity front. Flocs make the largest portion of SPM in the water column, because the computed floc parameter indicated mostly floc growth. However, the applied approach is insufficient since it lacks the concentration-dependent computation of settling velocities.

After all, it can be assumed that the model is able to depict real situations. In the present work the data input was partly insufficient. A richer input data set and better reference data would improve significantly and help to interprete the model results.

Appendix A

Statistics

This section, the statistical parameters which have been used for validation of model results against measurements are defined. Compared are times series at a given station with n elements of measured data set x and of the simulated data set y. The mean of the measurements is defined by:

$$\bar{x} = \frac{1}{n} \sum_{i=1}^{n} x_i \,, \tag{A.1}$$

the mean of the model results $\bar{y}$ is determined analogously.

The standard deviation of measured data is expressed as:

$$\sigma_x = \sqrt{\frac{1}{n-1} \sum_{i=1}^{n} (\bar{x} - x_i)^2} \,, \tag{A.2}$$

the standard deviation of the model results σ_y is defined analogously.

The bias is given by:

$$b = \bar{y} - \bar{x} \,. \tag{A.3}$$

The root-means-square error (rms error) is defined as:

$$rms = \sqrt{\frac{1}{n} \sum_{i=1}^{n} (x_i - y_i)^2} \,. \tag{A.4}$$

The standard deviation of model data to measured data is given by:

$$\sigma = \sqrt{\frac{1}{n-1}\sum_{i=1}^{n}((\bar{x} - x_i) - (\bar{y} - y_i))^2}\,. \tag{A.5}$$

The scatter index is defined by:

$$si = \frac{\sigma}{\bar{x}}\,. \tag{A.6}$$

Acknowledgement

First I would like to thank Prof. Dr. J. Sündermann and Dr. H. Günther for the appraisal of the work. They made it possible to complete the task at the GKSS. I would also like to thank Dr. M. Engel, who helped me run the first steps and who also provided the Buenos Aires connection. During my work in Buenos Aires I appreciated the support with knowledge and data of Dr. C. Simionato, W. Dragani and V. Meccia. My thanks also go to Mr. A. Tamusch who took time to listen to me and shared his sedimentological know-how of his past studies in the Rio de la Plata. Most parts of the work were performed at the GKSS Research Center with the support and patience of Dr. W. Rosenthal, G. Gayer, Dr. A. Pleskachevsky and other colleagues. Many thanks to them and also to Dr. J. Horstmann for being a serious and sometimes non-serious colleague and friend. Thanks to Adolfo for 'opening my eyes'. Thanks to Amanda for reading and english corrections. My special thanks go to Sónia and my family for the moral support and everything what makes life wonderful.

Bibliography

Backhaus, J.O. (1983). A semi-implicit scheme for shallow water equations for application to shelf sea modelling. *Continental Shelf Research*, **2(4)**, 243–254.

Backhaus, J.O. (1985). A three dimensional model for simulation of shelf sea dynamics. *Deutsche Hydrographische Zeitschrift*, **38(H.4)**, 164–187.

Backhaus, J.O. & Hainbucher, D. (1987). A finite difference general circulation model for shelf sea and its application to low frequency variability on the north european shelf. In J.C. Nihoul & B.M.J. (eds.), eds., *Three dimensional model of marine and estuarine dynamics.*, 221–244, Elsevier Oceanographic Series.

Carvallotto, J.L. (1987). Dispersion, transporte, erosion y acumulacion de sedimentos en el Río de la Plata. Tech. rep., Informe final de Beca de Iniciacion, Comision de Investigaciones Cientificas, La Plata - Rep. Argentina.

Demirbilek, Z. & Vincent, C.L. (2003). *Coastal Engineering Manual*, chap. Part 2 Water Wave Mechanics. US ARMY CORPS.

Depetris, P.J. (1968). Mineralogia de algunos sedimentos fluviales de la cuenca del Río de la Plata. *Asoc. Geol. Arg.*, **239(4)**, 317–325.

Depetris, P.J. & Griffin, J.J. (1968). Suspended load in the Río de la Plata drainage basin. *Sedimentology*, **11**, 53–60.

Depetris, P.J. & Paolini, J.E. (1991). Biogeochemical aspects of south american rivers: The Paraná and the Orinoco. http://www.icsu-scope.org/downloadpubs/scope42/chapter05.html.

Dittschke, D., Markofsky, M. & Zielke, W. (2005). Modelle für die Feinsedimentdynamik in Hafenbecken und Hafeneinfahrten unter Berücksichtigung der Feinstrukturen der Strömungs- und Transportprozesse. http://www.hydromech.uni-hannover.de/Mitarbeiter/DITSCHKE/index.html.

Eisma, D. & Cadee, G.C. (1991). Particulate matter processes in estuaries. http://www.icsu-scope.org/downloadpubs/scope42/chapter05.html.

Framinan, M.B. & Brown, O.B. (1996). Study of the Río de la Plata turbidity front, part 1: spatial and temporal distribution. *Continental Shelf Research*, **16(10)**, 1259–1282.

Gayer, G., Dick, S., Pleskachevsky, A. & Rosenthal, W. (2004). Modellierung von Schwebstofftransporten in Nordsee und Ostsee. Tech. rep., Bundesamt für Seeschifffahrt und Hydrographie, Hamburg.

Günther, H., Hasselmann, S. & Janssen, P.A.E.M. (1992). The WAM model cycle 4. Tech. rep., Deutsches Klimarechenzentrum, Hamburg.

Hasselmann, K. (1962). On the non-linear energy transfer in a gravity wave spectrum, part1: General theory. *Journal of Fluid Mechanics*, **12**, 481–500.

Hooker, S., Esaias, W., Feldman, G., Gregg, W. & McClain, C. (1992). An overview of SeaWiFS and ocean color. *SeaWiFS Technical Report Series*, **1**, 24 pp, nASA Technical Memorandum 104566.

Jacovkis, P.M. (2002). Some approaches to the Río de la Plata modeling. PROSUR. Third Meeting Co-Principal Investigators of the Project IAI CRN-055. Mar del Plata, Argentina, http://prosur.cima.fcen.uba.ar/documentos/jacovkis.pdf.

Kleine, E. (1993). Die Konzeption eines numerischen Verfahrens für die Advektionsgleichung - Literaturübersicht und Details der Methode im operationellen Modell des BSH für Nordsee und Ostsee. Tech. rep., Technischer Bericht des Bundesamtes für Seeschiffahrt und Hydrographie.

Laborde, J.L. (1987). Distribucion de sedimentos superficiales de fondo del Río de la Plata Exterior y Plataforma adyacente. *Invest. Oceanologicas*, **1(1)**, 19–30.

Laborde, J.L. (1997). *The Río de la Plata, An environmental review*, chap. Geomorphological and geological setting of the Río de la Plata, 1–16. Dalhousie University, Halifax, Nova Scotia.

Mansbridge, J. (2005). 5 minute gridded earth topography data. NOAA Product Information Catalog, http://edcsgs9bb.cr.usgs.gov/glis/hyper/guide/etopo5.

Menard, Y., Lefebvre, M., Escudier, P. & Fu, L. (1995). Ocean and climate: A quantitative answer, topex/poseidon. *Acta Astronautica*, **37**, 293–299.

Menendez, A.N. (2001). Description and modeling of the hydrosedimentologic mechanisms in the Río de la Plata river. VII International Seminar on Recent Advances in Fluid Mechanics, Physics of Fluids and Associated Complex Systems, Buenos Aires, Argentina, http://www.fi.uba.ar/laboratorios/lmm/com.htm.

Nagy, G.J., Martinez, C.M., Caffera, R.M., Pedraloza, G., Forbes, E.A., Perdomo, A.C. & Laborde, J.L. (1997). *The Río de la Plata, An environmental review*, chap. The hydrological and climatic setting of the Río de la Plata, 17–28. Dalhousie University, Halifax, Nova Scotia.

O'Connor, W.P. (1991). A numerical model of tides and storm surges in the Río de la Plata estuary. *Continental Shelf Research*, **11(12)**, 1491–1508.

Parker, G. & Laborde, J.L. (1990). Aspectos geologicos. In CARP-SIHN-SOHMA, ed., *Estudio para la Evaluacion de la Contaminacion en el Río de la Plata*, vol. 2 of *Informe de Avance 1989*, 1–72.

Parker, G., Marcolini, S., Cavallotto, J.L., Martinez, H., Lopez, M.C., Ghiorzo, D., de Leon, A., Maza, M.T., Ayup, R.N. & Laborde, J.L. (1985). Distribucion de sedimentos en la superficie del fondo. Tech. rep., SIHN-SOHMA, inf.Tec.No3, Tarea 2.

Parker, G., Marcolini, S., Cavallo, J. & Violante, R. (1987). Modelo esquematico de dispersion de sedimentos en el Río de la Plata. *Ciencia y Tecnologia del Agua*, **1(4)**, 68–80.

Pleskachevsky, A., Horstmann, J. & Rosenthal, W. (2001). Modelling of sediment transport in synergy with ocean colour data. In *4th Workshop on Ocean Remote Sensing "5 years of MOS-IRS"*, 177–182, Wissenschaft und Technik Verlag Berlin.

Pleskachevsky, A., Gayer, G. & Rosenthal, W. (2002). Numerical modelling of suspended matter transport. In *11th International Biennial Conference on Physics of Estuaries and Coastal Seas*, 476–479.

Pleskachevsky, A., Gayer, G., Horstmann, J. & Rosenthal, W. (2003). Synergy of satellite remote sensing and numerical modeling for monitoring of suspended particulate matter. *Ocean Dynamics*.

Puls, W., Kühl, H., Frohse, A. & König, P. (1995). Measurements of the suspended matter settling velocity in the German Bight (North Sea). *Deutsche Hydrographische Zeitschrift*, **47 (4)**, 259–276.

Ris, R.C., Holthuijsen, L.H. & Booij, N. (1999). A third-generation wave model for coastal regions, 2. Verification. *Geophysical Research*, **104**, 7667–7681.

Rodriguez, I., Alvarez, E., Krohn, E. & Backhaus, J.O. (1991). A mid-scale tidal analysis of waters around the north western corner of the Iberian penninsula. *Proceedings of Computer Modelling in Ocean Engineering*, **91**, 568pp.

Rosenthal, W. (1995). Derivation of Philips α-Parameter from turbulent diffusion as a damping mechanism. In G. Komen & W.e. Oast, eds., *Radar Scattering from Modulated Wind Waves*, 138–147, Kluwer Akademic Publishers.

Ruddick, K., Ovidio, F. & Rijkeboer, M. (2000). Atmospheric correction of SeaWiFS imagery for turbid coastal and inland waters. *Applied Optics*, **39/6**, 897–912.

SCHNEGGENBURGER, C. (1998). *Spectral Wave modelling with non-linear dissipation*. Ph.D. thesis, GKSS Report 98/E/42.

SCHNEGGENBURGER, C., GÜNTHER, H. & ROSENTHAL, W. (2000). Spectral wave modelling with non-linear dissipation: validation and applications in a coastal tidal environment. *Ocean Engineering*, **41**, 201–235.

SEAWIFS GSFC, N. (2005). SEADAS - SeaWiFS Data Analysis System. http://oceancolor.gsfc.nasa.gov/seadas/.

SIMIONATO, C.G., NUNEZ, M.N. & ENGEL, M. (2001). The salinity front of the Río de la Plata - a numerical case study for winter and summer conditions. *Geophysical Research Letters*, **28(13)**, 2641–2644.

SIMIONATO, C.G., MECCIA, V., DRAGANI, W. & NUNEZ, M.N. (2003). Circulacion estacional y plumas de los tributarios principales en el Río de la Plata. Tech. rep., CIMA.

SOULSBY, R. (1997). *Dynamics of marine sands*. Thomas Telford Ltd.

STRONACH, J.A., BACKHAUS, J.O. & MURTY, T.S. (1993). An update on numerical simulation of oceanographic processes in the waters between Vancouver island and the mainland: the gf8 model. *Oceanography and Marine Biology: An annual review*, **31**, 1–86.

TOLMAN, H.L. (1998). Validation of NCEP's ocean winds for the use in wind wave models. *Global Atmosphere and Ocean System*, **6**, 243–268.

URIEN, C.M. (1967). Los sedimentos modernos del Río de la Plata Exterior. *Bol. SIHN*, **4(2)**, 113–213.

VAN LEUSSEN, W. (1994). *Estuarine Macroflocs and their role in fine-grained sediment transport*. Ph.D. thesis, University of Utrecht, Netherlands.

WANG, M. (1999). A sensitivity study of the SeaWiFS atmospheric correction algorithm: Effects of spectral band variations. *Remote sensing Environment*, **67**, 348–359.

Wang, M. & Gordon, H.R. (1994). A simple, moderately accurate, atmospheric correction algorith for SeaWiFS. *Remote sensing Environment*, **50**, 231–239.

Wilber, C.G. (1983). *Turbidity in an aquatic environment: an environmental factor in fresh and oceanic waters*. Charles C. Thomas, Springfield, IL.

Winterwerp, J.C. (1999). *On the dynamics of high-concentrated mud suspension*. Ph.D. thesis, Delft University, Netherlands.

Nomenclature

u_{sinkX}	settling velocity of fraction X $[m/s]$
$\bar{U}$	mean current velocity $[m/s]$
ΔC	variation of concentration of SPM between two neighbouring layers $[kg/m^3]$
ΔM	variation of mass of SPM in a water layer $[kg/m^2]$
ΔM^B	delta of the sediment mass on the bottom $[kg/m^2]$
Δt	time step o the model $[s]$
ϕ	angle between current and wave direction
ρ	density of water $[1000kg/m^3]$
ρ_{sed}	density of the sediment $[1200kg/m^3]$
σ	intrinsic frequency $[1/s]$
τ	shear stress $[kg/s^2/m]$
τ_m	mean shear stress $[kg/s^2/m]$
τ_x	x-component of the wind stress vector $[m^2/s^2]$
τ_y	y-component of the wind stress vector $[m^2/s^2]$
τ_{cur}	shear stress induced by currents $[kg/s^2/m]$
τ_{wave}	shear stress induced by waves $[kg/s^2/m]$
θ	direction

ε	energy dissipation $[J/s/kg]$
a	constant
A_f	floc growth constant
A_h	horizontal turbulent viscosity $[m^2/s]$
A_v	vertical exchange coefficent $[m^2/s]$
A_{DIF}	diffusion coefficient
b	constant
C_C	Chezy coefficient $[m^{\frac{1}{2}}/s]$
C_D	friction coefficient
C_{kb}	SPM concentration in the lower most water layer $[kg/m^3]$
E	wave energy density
f	frequency $[1/s]$
f_w	roughness coefficient
G	root mean square velocity gradient $[1/s]$
g	acceleration of gravity $[m/s^2]$
h	water depth $[m]$
H_s	significant wave height $[m]$
h_{ero}	erosion depth $[m]$
k	wave number
k_s	Nikuradse grain roughness
M_k^B	mass of SPM in bottom layer k $[kg/m^2]$
M^{SED}	sediment mass in the lower most water layer $[kg/m^2/sec]$
N	wave action density

P_F	floc parameter
R_w	Reynolds number
S_{bo}	energy dissipation by bottom friction
S_{dis}	energy dissipation by turbulent diffusion and white capping
S_{in}	Snyder exponential growth
S_{ph}	Phillips linear growth of waves due to wind
t	time $[s]$
$TM1$	TM1 period of waves $[s]$
u	u-component of the velocity vector $[m/s]$
u^*	shear velocity $[m/s]$
U_w	orbital velocity on the bottom $[m/s]$
v	v-component of the velocity vector $[m/s]$
Z_A	bioturbation rate [days]